7-5-2012

# Incident shock Mach number effects on Richtmyer-Meshkov mixing with simultaneous density and velocity measurements

Gregory Orlicz

Gregory Christopher Orlicz

*Candidate*

Mechanical Engineering

*Department*

This dissertation is approved, and it is acceptable in quality and form for publication:

*Approved by the Dissertation Committee:*

Peter Vorobieff , Chairperson

Kathy Prestridge

Randall Truman

Svetlana Poroseva

Plamen Atanassov

# Incident shock Mach number effects on Richtmyer-Meshkov mixing with simultaneous density and velocity measurements

by

**Gregory Christopher Orlicz**

B.A., Bowdoin College, 2002
M.S., University of New Mexico, 2007

DISSERTATION

Submitted in Partial Fulfillment of the

Requirements for the Degree of

Doctor of Philosophy
Engineering

The University of New Mexico

Albuquerque, New Mexico

May, 2012

# Acknowledgments

I am thankful to many people for their respective roles in helping me to complete this journey. Most notably, I'd like to thank my parents for their undying support of me and my decisions. Their expectations and their confidence in me has inspired me to pursue challenges to the best of my ability, and to strive to become a better person. I'd also like to thank my collaborators at Los Alamos National Laboratory. Kathy Prestridge provided guidance throughout the entire process from experimental design to reporting experimental results, and was instrumental in keeping me on a path that could lead to success. Sridhar Balasubramanian dedicated his time over the course of several months to acquire this data set, and helped me in a countless number of ways during data processing and analysis. B.J. Balakumar and Ricardo Mejia-Alvarez provided me with very thoughtful suggestions, interpretation of results, and guidance throughout the data processing and analysis stage of this work. Others at Los Alamos to whom I owe my gratitude include Gavin Friedman, Megan Leftwich, and Chris Tomkins. I'd also like to thank my academic advisor, Peter Vorobieff, for his thoughts, wisdom, instruction, and help with overcoming challenges and hurdles along the way. Finally, I'd like to acknowledge the important role that my friends have played; whether it be providing encouragement, understanding, or simply a listening ear, I owe them much thanks and appreciation.

# Incident shock Mach number effects on Richtmyer-Meshkov mixing with simultaneous density and velocity measurements

by

**Gregory Christopher Orlicz**

B.A., Bowdoin College, 2002

M.S., University of New Mexico, 2007

Ph.D., Engineering, University of New Mexico, 2012

## Abstract

Experiments were performed at the horizontal shock tube facility at Los Alamos National Laboratory to study the effect of incident shock Mach number ($M$) on the development of the Richtmyer-Meshkov instability after a shock wave impulsively accelerates a varicose-perturbed, heavy-gas curtain (air-SF6-air). Three cases of incident shock strength were experimentally investigated: $M = 1.21$, 1.36, and 1.50. The resulting instability and subsequent fluid mixing is measured using simultaneous quantitative Planar Laser-Induced Fluorescence (PLIF) and Particle Image Velocimetry (PIV) for the first time in a Richtmyer-Meshkov Mach number study, while exceptional experimental repeatability allows for isolation of Mach number effects. Investigated are the mechanisms that drive the mixing, at both large and small scales, by examining the time evolution of simultaneous, 2-D density and velocity fields for each Mach number. Several differences in qualitative flow features are identified as

a result of Mach number variation, with differences in vortex interaction playing a critical role in the development of the flow field. Several quantities, including mixing layer width, mixing layer area, interface length, vorticity, circulation, velocity fluctuations, instantaneous mixing rate, the density self-correlation parameter, and other measures of turbulence and mixedness are examined as a function of time. These quantities are also examined versus time scaled with the convection velocity of the mixing layer, showing that the rate of change of several of these quantities with the distance the mixing layer travels is independent of Mach number. Results show that higher Mach number yields greater mixing uniformity at a given downstream location, while lower Mach number produces greater amount of mixing between the two gases, suggesting possible implications for optimization in applications with confined geometries.

# Contents

**List of Figures** **x**

**List of Tables** **xvi**

**1 Introduction** **1**

1.1 Overview . . . . . 1

1.2 Governing Equations . . . . . 3

1.3 Experimental History . . . . . 5

1.4 Previous Mach Number Effect Studies . . . . . 9

**2 Experimental Facility and Diagnostics** **14**

2.1 Initial Conditions . . . . . 15

2.2 Imaging Diagnostics . . . . . 20

2.3 Mach Number Variability . . . . . 24

**3 Image Processing** **34**

3.1 Quantitative PLIF Processing . . . . . 34

3.2 PIV Processing in the $x$-$y$ Plane . . . . . 41

3.3 PIV Processing in the $x$-$z$ Plane . . . . . 45

**4 Results** **46**

4.1 PLIF Time Series Comparison . . . . . 47

4.2 Mixing Layer Width . . . . . 61

4.3 Scaling the Mixing Layer Width . . . . . 65

4.4 Simultaneous PIV/PLIF Data . . . . . 72

4.5 Vorticity . . . . . 76

4.6 Circulation . . . . . 79

4.7 Velocity Fluctuations and Turbulent Kinetic Energy Estimates . . . . 81

4.8 Reynolds Number . . . . . 92

4.9 Instantaneous Mixing Rate . . . . . 95

4.10 Density Self Correlation . . . . . 104

4.11 Power Spectral Density . . . . . 111

4.12 Other Measures of Mixedness . . . . . 113

4.13 Vertical PIV Measurements . . . . . 124

**5 Conclusions** **130**

**A Preshock** **136**

**B Effect of PLIF Imaging on the Initial Conditions** **141**

**C Evolution of the Spike Feature** **143**

**References** **147**

# List of Figures


2.1 Shock tube schematic . . . . . 15

2.2 Test section schematic . . . . . 16

2.3 Photograph of initial conditions . . . . . 17

2.4 Initial condition vertical velocity map . . . . . 17

2.5 Initial condition vertical velocity streamwise profiles . . . . . 18

2.6 Schematic of passive coflow . . . . . 19

2.7 Photographs of the nozzle . . . . . 19

2.8 Photographs of the suction manifold . . . . . 20

2.9 Schematic showing vertical PIV field of view . . . . . 24

2.10 Mach number versus required driver pressure . . . . . 26

2.11 Mach 1.21: Sample signal traces . . . . . 30

2.12 Mach 1.21: $x$-$t$ diagram . . . . . 31

2.13 Mach 1.36: Sample signal traces . . . . . 32

2.14 Mach 1.36: $x$-$t$ diagram . . . . . 32

2.15 Mach 1.50: Sample signal traces . . . . . 33

2.16 Mach 1.50: $x$-$t$ diagram . . . . . 33

3.1 Test cell picture . . . . . 36

3.2 Laser sheet PLIF images . . . . . 37

3.3 Laser variation correction demonstration . . . . . 38

3.4 Spanwise intensity line profiles . . . . . 38

3.5 IC camera perspective correction . . . . . 40

3.6 DYN camera calibration grid . . . . . 41

3.7 PIV camera perspective correction . . . . . 42

3.8 Resolution study: PIV images . . . . . 44

4.1 Nomenclature for flow features . . . . . 47

4.2 Mach 1.21: $SF_6$ volume fraction maps, complete time evolution . . . 51

4.3 Mach 1.36: $SF_6$ volume fraction maps, complete time evolution . . . 52

4.4 Mach 1.50: $SF_6$ volume fraction maps, complete time evolution . . . 53

4.5 Mach 1.21: $SF_6$ volume fraction maps, complete time evolution (constant contrast) . . . . . 54

4.6 Mach 1.36: $SF_6$ volume fraction maps, complete time evolution (constant contrast) . . . . . 55

4.7 Mach 1.50: $SF_6$ volume fraction maps, complete time evolution (constant contrast) . . . . . 56

4.8 Illustration of repeatability, Mach 1.50 . . . . . 57

4.9 All Mach numbers: $SF_6$ volume fraction map time evolution comparison 60

4.10 Width measurement example . . . . . 62

4.11 Mixing layer width *vs.* time . . . . . 64

4.12 Mixing layer width *vs.* distance traveled . . . . . 68

4.13 Normalized mixing layer width *vs.* distance traveled . . . . . 68

4.14 Normalized mixing layer width *vs.* $t^{**}$ . . . . . 69

4.15 Scaled width *vs.* distance traveled . . . . . 70

4.16 Scaled width *vs.* $\tau$ . . . . . 71

4.17 Simultaneous PIV/PLIF: Mach 1.21 . . . . . 73

4.18 Simultaneous PIV/PLIF: Mach 1.36 . . . . . 74

4.19 Simultaneous PIV/PLIF: Mach 1.50 . . . . . 75

4.20 2-D vorticity maps . . . . . 77

4.21 Vorticity *vs.* time . . . . . 78

4.22 Vorticity *vs.* distance traveled . . . . . 78

4.23 Visual demonstration of circulation calculation . . . . . 80

4.24 Circulation *vs.* time . . . . . 80

4.25 Circulation *vs.* distance traveled . . . . . 81

4.26 RMS of velocity fluctuations at earlier times . . . . . 83

4.27 RMS of velocity fluctuations at later times . . . . . 84

4.28 PDFs of velocity fluctuations: Mach 1.21 . . . . . 86

4.29 PDFs of velocity fluctuations: Mach 1.36 . . . . . 87

4.30 PDFs of velocity fluctuations: Mach 1.50 . . . . . 88

4.31 Mean turbulent kinetic energy estimates ($\overline{K_{12}}$) *vs.* time . . . . . 90

4.32 Mean turbulent kinetic energy estimates ($\overline{K_{12}}$) *vs.* distance traveled 90

4.33 Mean turbulent kinetic energy estimates ($\overline{K_{12}}$) scaled *vs.* distance traveled . . . . . 91

4.34 Reynolds number: based on mixing layer width . . . . . 93

4.35 Reynolds number: based on circulation . . . . . 93

4.36 Reynolds number: based on TKE estimates . . . . . 94

4.37 All Mach numbers: Instantaneous mixing rate map comparison over time . . . . . 97

4.38 Instantaneous mixing rate *vs.* time . . . . . 98

4.39 Instantaneous mixing rate *vs.* distance traveled . . . . . 99

4.40 Consistency of current instantaneous mixing rate results with previous work . . . . . 100

4.41 Instantaneous mixing rate PDFs: Mach 1.21 . . . . . 101

4.42 Instantaneous mixing rate PDFs: Mach 1.36 . . . . . 102

4.43 Instantaneous mixing rate PDFs: Mach 1.50 . . . . . 103

4.44 Density self correlation (max value) *vs.* distance traveled . . . . . 107

4.45 Density self correlation (mean value) *vs.* distance traveled . . . . . 107

4.46 Density self correlation: Mach number comparison . . . . . 109

4.47 Density self correlation: whole field *vs.* just signal . . . . . 110

4.48 Power spectra of density fields . . . . . 112

4.49 Area of PLIF signal *vs.* distance traveled . . . . . 114

4.50 Mean $SF_6$ volume fraction ($\overline{c_v}$) *vs.* distance traveled . . . . . 114

4.51 Interface length *vs.* time . . . . . 116

4.52 Interface length *vs.* distance traveled . . . . . 117

4.53 Mean volume fraction streamwise profiles: Mach number comparison 119

4.54 Volume fraction PDFs: Mach 1.21 . . . . . 121

4.55 Volume fraction PDFs: Mach 1.36 . . . . . 122

4.56 Volume fraction PDFs: Mach 1.50 . . . . . 123

4.57 Vertical PIV: Raw particle fields . . . . . 127

4.58 Vertical PIV: vertical velocity maps . . . . . 128

4.59 Vertical PIV: streamwise velocity fluctuation maps . . . . . 129

A.1 PLIF images showing "preshock" deformation and the resulting post-shock structures . . . . . 138

A.2 Pressure traces from an experiment with late "preshock" . . . . . 139

A.3 Pressure traces from an experiment with intermediate "preshock" . . 139

A.4 Pressure traces from an experiment with early "preshock" . . . . . 140

B.1 Illustration of IC laser intrusiveness . . . . . 142

C.1 Shock wave focusing, reprinted from *Kumar et al. (2005)* . . . . . 144

C.2 Evolution of the spike feature . . . . . 146

# List of Tables

2.1 Table summarizing driver section pressures ($p_4$), and experimental and theoretical times after first shock arrival at PT4 for various events. Theoretical values were calculated using 1-D gas dynamics. . 29

4.1 List of parameters governing the flow, including input values used in Eq. 4.1, with $'$ denoting post-shock conditions when ambiguous. . . . 48

4.2 List of values pertaining to Equation 4.25. Measured values of the final interfacial area are approximately 1.4 times higher than estimated values for each Mach number. . . . . 116

# Chapter 1

# Introduction

## 1.1 Overview

The instability arising at the interface between two fluids of different densities due to the impulsive acceleration of the interface, and the misalignment of pressure and density gradients, is known as the Richtmyer-Meshkov (RM) instability [1, 2, 3]. It is a limiting case of the Rayleigh-Taylor [4, 5] instability that occurs when a constant acceleration, such as gravity, acts in the direction from a heavy fluid to a light fluid. Any perturbation that exists at the interface will grow with time, eventually causing the two fluids to mix. In the RM case, the interface becomes unstable regardless of the direction (i.e. heavy to light or light to heavy) of the impulsive acceleration (e.g. shock wave) [3]. Conversely, any perturbations of a fluid interface in a light to heavy orientation under constant acceleration (e.g. ripples on the interface between water and air in a pond) decay with time, leading to a stable solution.

While studying the Richtmyer-Meshkov instability is necessary for insight into the fundamental physics of shock driven variable density mixing, it is also of interest for its relevance in several applications, both practical and naturally occurring,

encompassing a range of scales [6]. In inertial confinement fusion (ICF), impulsive compression of the higher density ice deuterium-tritium (DT) layer into the lower density DT gas by high energy lasers gives rise to the RM instability and undesired mixing. This impairs the maximum pressure that can be attained, thus limiting the efficiency of the reaction and requiring greater laser input energy than reaction output energy [3, 6, 7, 8]. In supersonic combustion ramjet engines, maximizing the degree of mixing of fuel and oxidizer is of critical importance for combustion rate and improved engine efficiency [3, 6, 9]. Mixing can be enhanced by passing the 'light' hydrogen fuel and the 'heavy' air through an oblique shock wave, thereby producing RM instability. The RM instability is also important in deflagration-to-detonation transition [3, 6, 10]. In nature, it is believed that the RM instability plays a large role in the mixing processes after supernova explosions, as evidenced in Supernova 1987A where the helium and hydrogen layers were observed to be much less stratified than originally predicted, indicating some mechanism of mixing [3, 6, 11]. After the final stage of fusion, a star collapses to its core until it becomes so dense that the in-falling matter rebounds, producing a spherical shock wave that propagates outward. As the shock wave propagates through the stratified layers of the dying star, any misalignment of pressure and density gradients produces vorticity, which would serve to enhance the mixing of the remnant gases through the RM instability.

The underlying mechanism for amplification of initial perturbations in the RM instability is baroclinic vorticity deposition, generated by the misalignment of pressure (shock wave) and density gradients (fluid interface) [3]. Consider the case of a plane sinuous interface with small initial perturbation amplitude. Initially, after the pressure impulse, vorticity amplifies the perturbations causing the peaks and troughs of the interface to grow linearly in time. As time increases, the peaks and troughs grow asymmetrically, with spikes of heavy fluid penetrating into light, and bubbles of light fluid penetrating into heavy [3]. When the perturbation amplitude approaches that of the wavelength, the growth is nonlinear. At later times, vorticity

causes the spikes to evolve, rolling up into mushroom shaped structures, and the Kelvin-Helmholtz shear instability causes small scale features to appear along the distorting interface [3]. Eventually, this may lead to turbulent mixing.

## 1.2 Governing Equations

Taylor first developed a theory to describe the growth of sinusoidal perturbations on an interface between a heavy fluid of density $\rho_2$ over a light fluid of density $\rho_1$ in a constant gravitation field using linear stability theory [3, 5, 6]. Given a perturbation of $a(x,t) = a(t)cos(kx)$ the perturbation amplitude grows according to

$$a = a_0 cosh(\sqrt{kgA}t) \tag{1.1}$$

where $a$ is the amplitude ($a_0$ is the initial perturbation amplitude), $\kappa = \frac{2\pi}{\lambda}$ is the wavenumber, $g$ is constant acceleration due to gravity, and $A$ is the Atwood number defined as the difference between fluid densities divided by their sum,

$$A = \frac{\rho_2 - \rho_1}{\rho_2 + \rho_1} \tag{1.2}$$

where $\rho$ is the fluid density, and by convention the acceleration is directed from fluid 2 to fluid 1. Therefore, the Atwood number is positive if acceleration is directed from a heavy to a light fluid.

Thus, in such a configuration of a heavy fluid over a light fluid, perturbations grow exponentially with time as long as the interfacial amplitude is small compared to the wavelength, $\lambda$ [1, 6, 12, 13]. In general, this is taken to be the case as long as $ka$ <1 [1, 3, 6]. As the amplitude approaches the wavelength, nonlinearities come into play and this linear model is no longer valid. Note that if gravity is directed in the opposite direction, the system stabilizes.

Richtmyer expanded upon Taylor's formulation by postulating the growth of initial perturbations of a fluid interface due to an impulsive force [1, 3, 6]. He considered

the case of a planar shock wave traveling in a direction normal to the interface from a light to a heavy fluid. If the shock wave is sufficiently weak, fluid incompressibility can be assumed. It should be noted that in many practical applications and experimental research, incompressibility cannot be assumed, as compressible effects result in departures from Richtmyer's model. Richtmyer modeled the problem using Taylor's equations, but substituted gravitational acceleration with a Dirac delta function to capture the impulsive force [1, 3, 6]. Richtmyer's linear stability theory based formulation then yields a growth rate of the incompressible instability

$$\frac{da}{dt} = \kappa A \Delta v a_0 \tag{1.3}$$

where $\Delta v$ is the velocity imparted upon the interface by the impulsive acceleration. In contrast to constant acceleration, in the impulsive acceleration case the growth rate does not depend on time, and perturbations grow linearly as long as the amplitude is sufficiently small ($ka < 1$) [6], and nonlinearity does not dominate the solution. Although not considered by Richtmyer, growth occurs regardless of the orientation of the fluids (i.e. light to heavy or heavy to light). In the heavy to light case, the initial perturbations first decrease in amplitude, reverse phase, and then continue to grow linearly in the small amplitude regime [3, 6]. Meshkov was the first to confirm Richtmyer's results experimentally, albeit qualitatively, giving rise to the instability's name [3].

The mechanism by which vorticity is generated is derived from the equation for a Navier-Stokes fluid. By taking the curl of the momentum, one obtains the vorticity equation

$$\frac{\partial \vec{\omega}}{\partial t} = -\vec{u} \cdot \vec{\nabla}\vec{\omega} + \vec{\omega} \cdot \vec{\nabla}\vec{u} - \vec{\omega}(\vec{\nabla} \cdot \vec{u}) + \frac{1}{\rho^2}(\vec{\nabla}\rho \times \vec{\nabla}p) + \text{viscous terms} \tag{1.4}$$

where $\vec{\omega}$ is the vorticity vector aligned normal to the plane of motion, $\vec{u}$ is the velocity vector of a fluid element, $\nabla p$ is the pressure gradient (e.g. across a shock

wave), and $\rho$ is the density of the fluid at a given location [14, 15]. In the current study, the flow is considered to be two-dimensional, viscous effects are assumed small, and because it is driven by a shock, baroclinic vorticity deposition is considered to dominate. Assuming all terms on the right hand side to be negligible compared to the baroclinic term, the vorticity equation becomes

$$\frac{\partial \vec{\omega}}{\partial t} = \frac{1}{\rho^2} \vec{\nabla} \rho \times \vec{\nabla} p \tag{1.5}$$

It can be seen that vorticity deposition is maximized when the pressure and density gradients are orthogonal. Comprehensive reviews of the RM instability are presented by Brouillette [3], Zabusky [15], and Vorobieff and Kumar [16].

## 1.3 Experimental History

Experimentally, the most common way to achieve an impulsive acceleration for study of the RM instability is to produce a traveling shock wave in a shock tube [3, 6, 16]. In a typical shock tube, one end of the tube (driver section) is separated with a diaphragm and is pressurized. At a designated pressure, the diaphragm is ruptured and a shock wave begins propagating down the length of the tube (driven section), while an expansion fan begins traveling upstream toward the driver section end wall. As the shock wave travels through the driven section, it becomes planar. At some position downstream (test section), a fluid interface is created and viewports allow for interrogation of the resulting fluid dynamics before and after shock passage. The two most significant obstacles for experimental study of the RM instability are (1) the creation of a well–characterized and repeatable fluid interface, and (2) the implementation of adequate diagnostics.

To address the first problem, the early experiments used fragile membranes [6, 16] to separate two gases and create a well defined, unmixed, single interface. The mem-

branes were spread over a very thin wire mesh in a sinusoidal pattern to give the initial perturbation. Upon arrival of the shock wave, the membrane is shattered and the shock wave passes through the interface giving rise to the RM instability. Although the interface is well characterized and repeatable, the use of the membrane introduces new problems [3, 6, 16]. First, fragments from the shattered membrane become entrained in the resulting flow, and it is unclear what effect this has on the fluid dynamics. Often, experiments that have used membranes have reported growth rates that are smaller than those predicted by theory, indicating that the membrane adds an unknown level of complexity to the dynamics of the system [6]. The membrane fragments also complicate visualization of the flow, making it difficult to use planar imaging techniques, and more difficult to attain quantitative information from planar visualization. Membranes were also used in later experiments to create sawtooth perturbations on a single interface [17, 18, 19], and other geometries [20, 21, 22, 23].

Experiments have also used a sliding plate with a sinusoidal perturbation to initially separate the two fluids [24, 25]. Just before the shock is released, the plate is retracted and the shock wave interacts with the interface. However, the motion of the plate drags fluid along with it, causing perturbations on the interface that cannot be controlled. Additionally, some mixing of the two gases occurs before shock impact resulting in a relatively thick, diffuse interface. Therefore, the initial conditions in these experiments are difficult to characterize, and lack repeatability. This not only makes comparison of the experimental results to numerical models and theory a significant challenge, but also inhibits comparison between experiments.

In another experiment, first reported by Jones and Jacobs [26], a new technique for creating a membraneless single interface in a vertical shock tube was developed. In this experiment, light and heavy gases flow through opposite ends of the tube meeting at some location where slots in the tube walls on opposite sides allow the gases to

exit. This leaves behind a nominally flat and relatively thin interface between the gases at the stagnation point of the opposing flows. The shock tube is then oscillated in the horizontal direction at a prescribed frequency using a stepper motor and crank to produce a sinusoidal standing wave for the initial perturbation. This same setup has since been used by others [12, 27] and has achieved growth rate results that are in good agreement with models in the linear regime.

The RM instability has also been studied at a liquid–liquid interfaces [6, 28, 29] and solid–solid interfaces [30, 31]. In both cases, the interface is much more clearly defined than in membraneless gas–gas interface experiments. The Nova laser experiment at Lawrence Livermore National Laboratory employs high powered lasers to ablate a target to produce a strong shock wave ($M > 10$) that travels through a machined solid-solid 2-D sinusoidal interface [30]. Two major difficulties with studying RM instability in solids are that very strong shock waves are needed to make the solids behave as fluids, and visualization of the resulting flow using radiography lacks resolution. In a notable incompressible liquid-liquid interface experiment, a sinusoidal interface of light fluid over heavy fluid is formed in a clear tank that is mounted on a pair of vertical rails [28]. The sled is then made to drop onto a coil spring where it rebounds to provide an impulsive acceleration. The resulting RMI can then be visualized during the subsequent free fall until the tank impacts the spring for the second time. Because the impulsive force is relatively weak and the Atwood number is relatively low compared to other RM studies ($A = 0.30$ and 0.15), the development of the RM instability is relatively slow. Slower growth has the advantage of greater ease of visualization, and with the aid of a well defined interface, this experiment yields good comparison with incompressible linear growth models after taking into account the finite interaction time with the spring [6]. However, study of the late time nonlinear regime is not possible as the RM instability is still at a relatively early stage upon completion of the free fall of the tank. This experiment was improved upon later to allow more time for free fall with improved diagnostics

and improved interfacial perturbation mode generation [6]. However, well–mixed turbulent states are still beyond the reach of the experiment.

While single interface experiments are desirable test cases for validation of models, other more complex interfacial configurations have been extensively studied. These include spherical soap film bubbles of light or heavy gas in vertical shock tubes [16, 32, 33], laminar jet cylinders of light or heavy gas [34, 35, 36, 37], and heavy gas curtains with membranes [23] and without [38, 39, 40, 41, 42, 43, 44, 45, 46, 47] in horizontal shock tubes. In the recent spherical bubble experiments [32, 33], a soap film bubble is created by a retractable injector in air. Once the bubble is formed, the injector releases the bubble and is retracted into the inner wall of the shock tube so as not to disrupt the flow. The bubble then falls or rises (depending on the density of the injected gas) a certain distance to allow for oscillations of the bubble to die out before a shock wave is timed to impact the bubble within the field of view. In gas cylinder experiments, a laminar jet is flowed out of a nozzle upwards (He) or downwards ($SF_6$) through the test section of a horizontal shock tube, and then impacted by a shock wave. In one horizonal shock tube experiment, the RM instability resulting from five different configurations of heavy $SF_6$ cylinders was studied [37]. Reported were the comparison of integral mixing widths, as well as, for the first time in shock accelerated gaseous flows, the stretching rate of material lines made possible by advanced diagnostics.

In the present study, the interface of interest is a membraneless, varicose, heavy–gas ($SF_6$) curtain flowing in air. This configuration is sometimes referred to as A-B-A, in the sense that one fluid, B, is sandwiched by fluid A, creating two nearby interfaces (first light to heavy and then heavy to light). Its formation is similar to the laminar heavy gas jet cylinder experiments, and relies upon the shape of the nozzle. In both the flowing cylinder and curtain experiments, a small amount of diffusion occurs, resulting in an interface of finite thickness, but in most experiments this effect is

minimized by imaging cross-sections close to the nozzle exit.

In the varicose curtain, the existence of two nearby interfaces adds a level of complexity to the dynamics of the RM instability, as the initial perturbations on either side of the curtain do not grow independently, but interact and influence the instability development. In the first curtain experiments, 3 distinct flow morphologies were reported from the same nominal initial conditions [38]. Later these morphologies were observed experimentally and shown numerically to be the result of small differences in the initial conditions[39, 48], specifically, that the perturbation amplitudes were either slightly greater on the upstream side (upstream mushrooms), downstream side (downstream mushrooms), or nominally equal on both sides (sinuous). The qualitative flow bifurcation in these experiments showed just how sensitive the resulting RM instability is to even very small changes in initial conditions, and moreover emphasized the importance of being able to generate initial condition repeatability with good characterization. Obtaining the required degree of initial condition repeatability for the free flowing jet curtain has proven to be one of the greatest experimental challenges in the current facility. However, through the modification of the inlet and suction nozzles, the initial conditions in the present study are very repeatable, as discussed in Chapters 2 and 4. With advanced diagnostics, they are also well characterized.

## 1.4 Previous Mach Number Effect Studies

In the present study, multiple experiments were performed on a varicose, heavy gas curtain to observe the effects of the resulting RM instability when the incident shock wave Mach number was varied within the weak shock regime ($M \leq 2$). Some previous studies with a variety of initial conditions have reported results of Mach number variation, but overall, reports regarding Mach number effects in the RM

instability are sparse.

One experiment that discusses Mach number effect is reported by Jacobs and Krivets [27] in which a membraneless single interface between air and $SF_6$ is created using opposing flows that exit from slots in the side of the shock tube. Reported in this study are experiments at three different Mach numbers: $M = 1.1$, 1.2 and 1.3, with nominally the same sinusoidally perturbed initial conditions (results from $M = 1.1$ and 1.2 were first reported in Collins and Jacobs [12]). In this study, it was found that slightly increasing the Mach number of the incident shock effectively increases the duration of the experiment when time is nondimensionalized. In an absolute sense, increasing the Mach number allowed the researchers to observe the RM instability in a more developed state before the reflected shock wave from the end of the shock tube returned to interact with the evolving interface. Perturbation amplitude growth of the single interface was also reported. Growth data agreed fairly well with amplitude growth models, and could be effectively collapsed if amplitude and time were appropriately nondimensionalized. It was also stated that increasing the Mach number from 1.1 to 1.2 effectively caused the interface to develop twice as fast since the interface velocity is a factor of 2 larger in $M = 1.2$, and the amplitude growth is proportional to interface velocity, as given by Richtmyer's linear formula.

In a more recent membraneless single interface experiment by Motl *et al.* [49], a larger parameter space was investigated. By conducting experiments with a variety of different gases, a wide range of Atwood numbers were explored ($0.29 < A < 0.95$) in addition to a wide range of Mach numbers ($1.1 < M < 3$). The interface was created in a similar fashion as discussed above in references [12, 27]. Qualitative flow visualization was used to measure mixing layer width, however initial growth rates could not be experimentally measured. Yet, it was found that the mix width from experiments across the entire parameter space could be collapsed by using Richtmyer's impulsive formula and a growth rate reduction factor derived from numerical

simulations to account for the diffusion thickness of the interface in the experiments. Certain features in the flow field were also identified as an effect of increasing Mach number, including bubble flattening and chevron shaped features underneath the spike.

Two separate experiments carried out by Ranjan *et al.* show the effect of varying incident shock Mach number on a spherical heavy argon bubble [32], and a spherical light helium bubble [33], both in atmospheric nitrogen. The intent of both studies was to attempt to bridge the gap between high Mach number laser driven experiments ($M > 10$) and previous low Mach number, bubble interface, shock tube experiments. In the Mach 2.88 heavy bubble case, researchers observed a secondary vortex ring that was not previously seen in similar experiments at Mach 1.3 or lower, but was previously predicted. The researchers suggest that this feature may result due to differences in compressibility effects when the particle velocity behind the incident shock wave becomes supersonic, which occurs at Mach 2.07 in nitrogen at atmospheric temperature. Similarly, in the Mach 2.95 light bubble experiment, secondary and tertiary counter-rotating vortex rings in the flow field were observed for the first time that were absent in the previous experiments carried out at $M < 1.3$. These features caused the rate of bubble elongation (integral width) to be twice that of the previous low Mach number studies. The researchers attribute these additional flow features in the higher Mach number light bubble experiment to more complex shock refraction and reflection phenomena occurring with stronger incident shocks.

In the solid–solid sinusoidal machined interface Nova laser experiments, Holmes *et al.* [30] report results from negative Atwood number experiments with incident shock Mach numbers of 10.8 and 15.3. It was found that absolute perturbation growth rate increases with Mach number; however, if the growth rates are nondimensionalized by experimental parameters, they reduce with increasing Mach number. This result is confirmed by simulations and models in the report. The nondimensional growth rate

reduction is attributed to higher compression of the geometric perturbations at the interface, and resulting changes in the post-shock Atwood numbers as Mach number is increased.

Another experiment reported by Sadot *et al.* [18] investigates the RM instability resulting from a sawtooth perturbed air/$SF_6$ interface that is initially separated by a membrane. Two experiments were carried out, one with large initial perturbation amplitudes and low Mach number ($M = 1.2$), and the other with small initial amplitudes and moderate Mach number ($M = 2$). Because both parameters were changed between experiments, it is unclear what conclusions can be drawn. Measured in both experiments was the amplitude of the bubble flow feature. In the low Mach number, high amplitude experiment the growth rate of this feature remained positive, but in the moderate Mach number experiments, the growth rate became negative. The researchers attribute this negative growth rate to pressure fluctuations in front of the bubble due to shock reverberation. Yet, it is concluded that altering the perturbation amplitude is the dominant explanation for flow feature differences between the two experiments. Another Mach number study was reported by Bliznetsov *et al.* [21], in which single interface initial conditions of unreported geometric characterization with both helium/$SF_6$ and air/$SF_6$ configurations were accelerated by shocks ranging from Mach 2 to 9. It was simply reported that higher Mach number shocks cause higher fluid interface velocities and higher mixing width growth rates.

Some of these experiments discuss interesting results related to Mach number effect, but they are lacking in diagnostic capability. The present work represents an extension of previously reported experiments [47, 50] carried out at the Los Alamos horizontal gas shock tube facility in which a varicose-perturbed, thin, heavy-gas curtain was impulsively accelerated by planar shock waves of varying strength within the weak shock regime, and studied using qualitative planar laser induced fluorescence (PLIF) to acquire 2-D intensity fields. In the previous work, it was found that mixing

width growth rates scaled with the mean velocity of the curtain between Mach 1.21 and Mach 1.54 experiments, while measurements of the instantaneous mixing rate did not collapse with the same scaling. This demonstrated that there is a disparity in the time scale for small *vs.* large scale mixing when Mach number is varied. The current work aims to extend our understanding of the physics governing the instability growth and mixing through the addition of particle image velocimetry (PIV) measurements that provide instantaneous velocity fields, obtained simultaneously with quantitative PLIF measurements that provide 2-D density fields. Moreover, the new sets of experiments conducted compare 3 different Mach numbers (Mach 1.21, 1.36, and 1.50), with instability growth observed for a longer duration made possible by a new test section with extended optical access. Chapter 2 contains a description of the experimental facility, Chapter 3 discusses the processing of image data, and Chapter 4 presents the results of the investigation.

# Chapter 2

# Experimental Facility and Diagnostics

The experiments were performed at the gas shock tube facility at Los Alamos National Laboratory using a horizontal shock tube with a 3 in. square cross section and a total length of approximately 5.3 m. A schematic can be found in Figure 2.1. The driven, test, and end sections are open to atmosphere (11.5 psi). The driver section is initially separated from the rest of the tube by a polypropylene film and is pressurized with nitrogen or helium gas to the appropriate level to generate the desired Mach number shock wave. Experimentally, this was determined to be approximately 22 psi ($N_2$), 30 psi (He), and 50 psi (He) for Mach 1.21, Mach 1.36, and Mach 1.50, respectively. Once the desired pressure is reached, a trigger is sent to a solenoid driven set of razor blades, which puncture the diaphragm. The rapid depressurization of the driver section generates a shock wave that becomes planar as it travels down the length of the tube, eventually interacting with the initial conditions. Four pressure transducers, embedded in the shock tube walls, are located along the path of the shock wave, and are used to measure shock speed, time of shock interaction with initial conditions, and to coordinate the timing of imaging diagnostics.

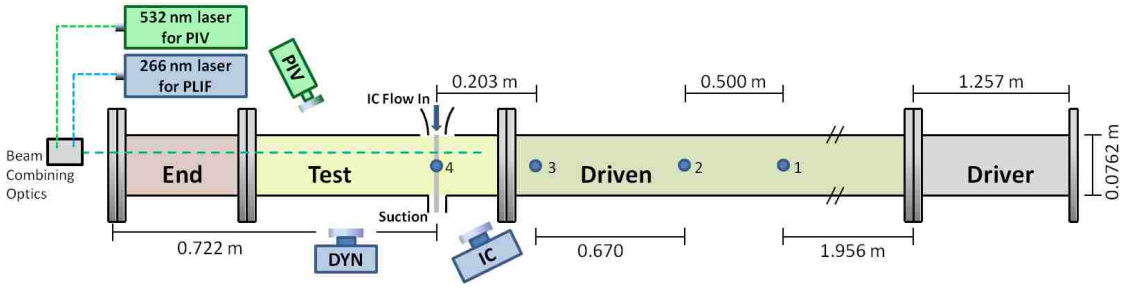


Figure 2.1: Shock tube schematic. Diaphragm is placed between Driver and Driven sections. Shock wave travels from right to left, with pressure transducers (PT) labeled 1 through 4. Shock speed is calculated between PT2 and PT3, and diagnostics are triggered off of PT3, while PT4 is coincident with IC location to measure time of shock interaction.

## 2.1 Initial Conditions

The initial conditions consist of a thin fluid layer of $SF_6$ with varicose perturbations surrounded by air. To seed the initial conditions for the imaging techniques discussed below, pure $SF_6$ gas is first bubbled through liquid acetone in a temperature controlled bath set to 20°C prior to reaching the settling chamber. The bath is set below room temperature to prevent subsequent condensation of the acetone vapor. The mixture is then sent to the settling chamber located above the shock tube. There, glycol fog particles are added to the mixture using a commercially available theatrical fog machine. The initial conditions are then formed by a gravity induced flow of the heavy gas mixture from the settling chamber to a specially designed nozzle whose exit is aligned with the top wall of the test section. The nozzle consists of a row of closely spaced holes of 3 mm diameter and 3.6 mm spacing. Porous flow straightening foam is also placed just upstream of the nozzle to help ensure laminar flow. The initial conditions flow through the test section (shown schematically in Figure 2.2, and photographed in Figure 2.3), where diffusion between the individual jets creates a heavy gas curtain, and exit at the bottom where there is a mild suction set just strong enough to prevent overflow of $SF_6$ into the test section. At the

measurement plane, the maximum vertical flow velocity of the initial conditions was measured to be 1.38 m/s, as seen in Figures 2.5 and 2.4, which is small compared to the horizontal velocity of the shock-induced flow (>100 m/s for all experiments). Figures 2.5 and 2.4 were obtained from "vertical PIV" measurements discussed in Section 2.2. The $SF_6$ concentration along the centerline at the measurement plane is estimated to be $\approx 50\%$ of pure $SF_6$, with 13% acetone vapor and 37% air by volume. For this composition, the Atwood number is $A = 0.52$, where $\rho_1$ is the density of air and $\rho_2$ is the density of the heavy gas mixture at the streamwise center of the curtain.

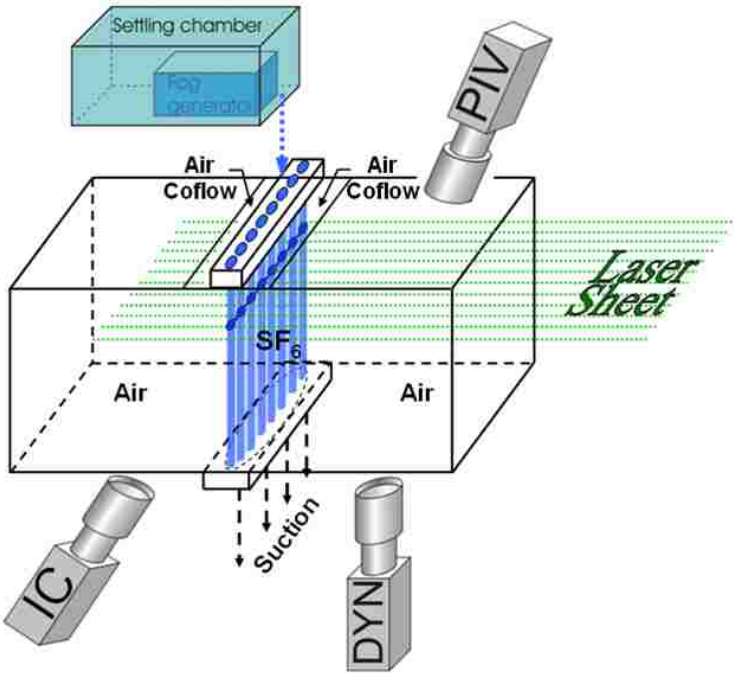


Figure 2.2: Test section schematic showing initial conditions and coflow. When fired, the shock wave will move from left to right.

Experimentally, it was found that if air could be entrained to flow passively on either side of the $SF_6$, the curtain could be made much more stable. If air was not entrained, then drag from the $SF_6$ flow caused the air within the test section to form circulation patterns, thus causing the curtain to oscillate in the streamwise direction

Figure 2.3: Photograph of the axis view of the shock tube (looking through the window at the end of the end section) showing the varicose curtain initial conditions flowing from top to bottom. Visualization was accomplished with fog droplets for flow seeding in the $SF_6$ and a flashlight for illumination.

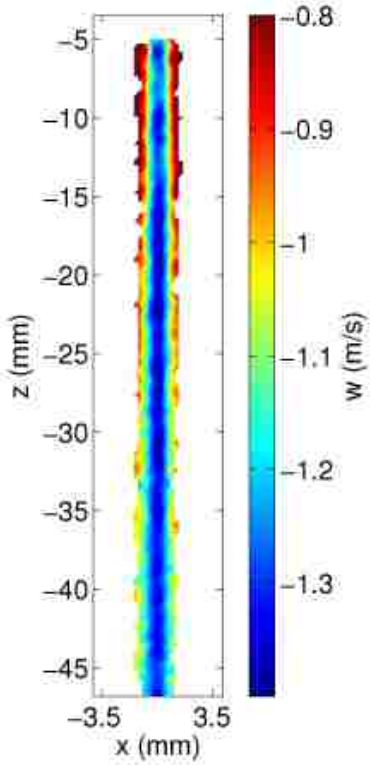


Figure 2.4: Spatial map of vertical velocity, $w$, for initial conditions. $z = 0$ represents the top wall of the shock tube, which coincides with the nozzle exit.

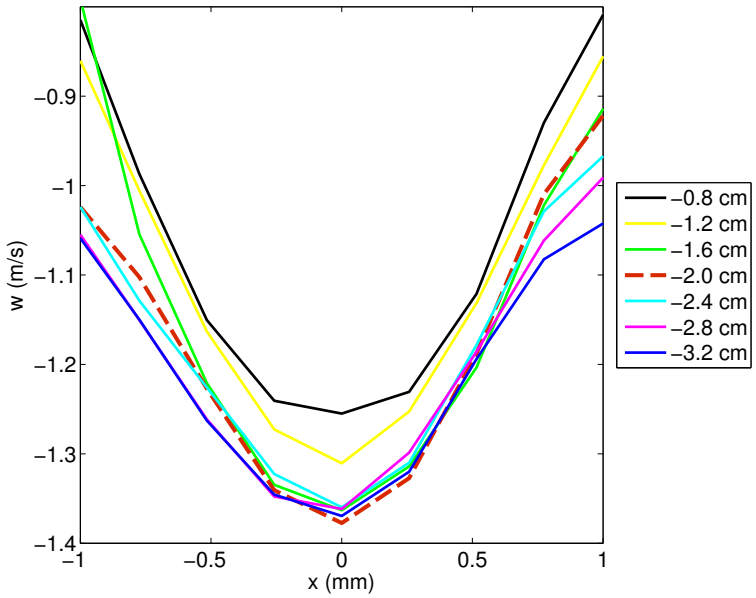


Figure 2.5: Comparison of streamwise profiles for initial condition vertical velocity, $w$, at different vertical positions. The red dashed line represents the primary imaging plane, 2 cm below the nozzle exit, with a maximum velocity of 1.38 m/s occurring at the center.

(see Figure 2.6). These unsteady oscillations led not only to unrepeatable initial conditions, but also to asymmetry within individual experimental runs in earlier experiments at the same facility. Therefore, the nozzle was designed to provide open slots on either side of the heavy gas through which external air would enter, forming a passive co-flow nozzle. To ensure laminar entrainment of the air, and thus a symmetric and repeatable $SF_6$ curtain, the bottom of the nozzle was designed with a smooth concave curve on two sides so that the nozzle itself was thinner than the opening to the test section at the insertion point. Given the level of complexity of such a part, stereolithography was found to be the ideal manufacturing method, and has become a standard for all IC generating nozzles used at the facility. The nozzle was custom fabricated by an outside company (Harvest Technologies Inc.) using the stereolithography process in which a liquid resin is hardened layer by layer upon laser contact. This allows for the manufacture of virtually any shaped plastic part given a properly formatted CAD drawing (see Figure 2.7 for photographs of the nozzle).

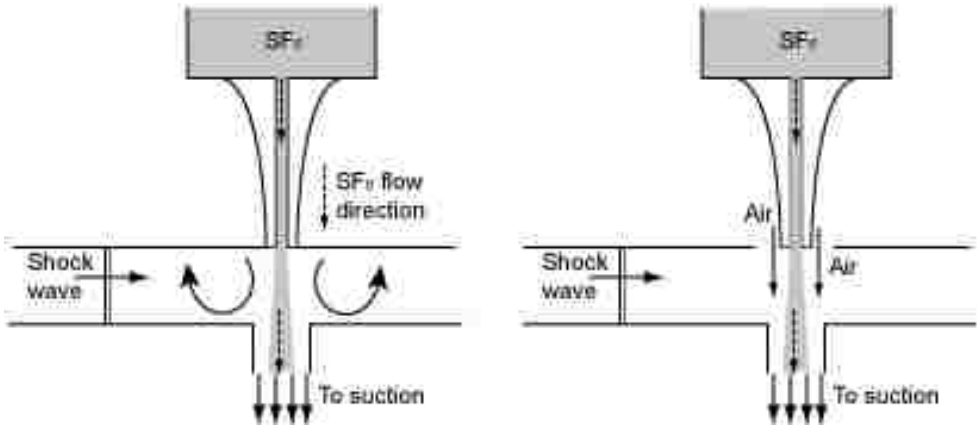


Figure 2.6: *Left*, flowing $SF_6$ induces circulation patterns in air on either side of the curtain leading to streamwise instability; *right*, the suction induces the air to flow alongside the curtain continually passing through the test section. [46, 50]

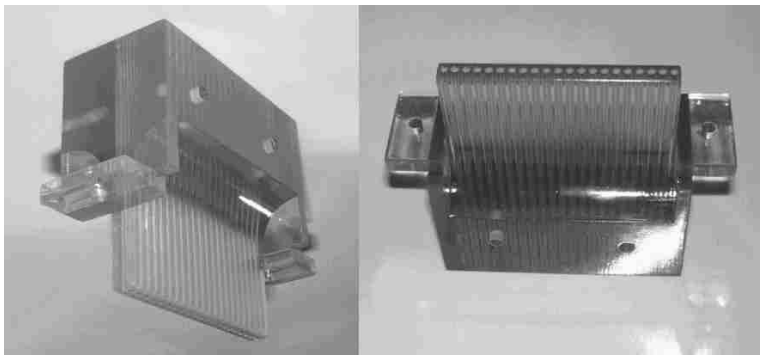

Figure 2.7: Two photographs of the nozzle created by stereolithography and used in the experiment. The narrow section with the row of holes is inserted downward into the test section. The curved surfaces allow for smooth entrainment of surrounding air for co-flow stabilization.

Initial conditions were also found to be sensitive to unsteady and uneven fluctuations in the suction at the bottom of the test section. To further improve curtain stability and experimental repeatability for this study, a specially designed suction manifold was also fabricated using stereolithography (Harvest Technologies Inc.) to interface the shock tube with the suction source in the laboratory. The suction manifold was designed with a bend to allow for optical access and camera placement. On

the inside, the opening slowly transitions from the rectangular shape at the exit of the shock tube to a circular shape where flexible tubing was attached to the hose barb fitting (see Figure 2.8 for photographs of the suction manifold). This part helped to generate a more steady, uniform suction at the bottom of the test section, and consequently, a more repeatable IC at the measurement plane.

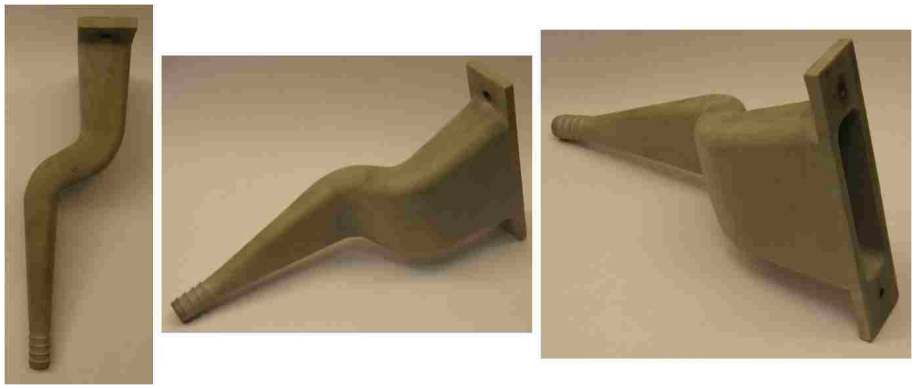

Figure 2.8: Three photographs of the suction manifold fabricated using stereolithography and used in the experiment. The end with the rectangular opening and flanges was attached to the bottom of the shock tube directly below the nozzle location. The suction was supplied through a flexible hose that was attached to the circular section with the hose barb connection.

## 2.2 Imaging Diagnostics

All images of the initial conditions and the resulting instability were acquired in a plane located 2 cm below the nozzle exit. Two imaging techniques were used simultaneously: planar laser-induced fluorescence (PLIF) and particle image velocimetry (PIV). These measurements were made using two dual headed neodymium-doped yttrium aluminum garnet (Nd-YAG) pulsed lasers with output frequencies of 266 nm (frequency quadrupled) for PLIF, and 532 nm (frequency doubled) for PIV. The lasers are co-aligned through a combination of optics and formed into a horizontal

laser sheet that enters the shock tube through a UV-transparent (fused silica) window in the end wall of the end section at a vertical location of 2 cm below the top wall. The light sheet thickness for all measurements was estimated to be ∼1.5 mm.

The light sheet from the 266 nm PLIF laser causes the acetone vapor to fluoresce within the visible range (350 to 550 nm), with a peak at 420 nm. The acetone vapor tracks the $SF_6$ at a molecular level, giving rise to very high quality, high resolution images representative of $SF_6$ concentration [51]. Acetone also has a phosphorescent signal in response to the laser pulse that occurs on a longer time scale than the fluorescent signal. However, oxygen from the surrounding air that has diffused into the curtain quenches the phosphorescence signal, and blurring of the post-shock flow visualization images is avoided despite the high convective velocity. The 10 ns pulse width is also short enough so that no image blurring occurs from the fluorescent signal itself. For the highest Mach number studied, a parcel of gas traverses, at most, 4% of the pixel size in that time.

A small percentage of the 266 nm PLIF laser beam is directed into a laser power meter prior to laser sheet formation to confirm laser pulse timing as well as to calibrate PLIF data for quantitative processing (discussed below). PLIF images are acquired using two separate Apogee charge-coupled device (CCD) cameras to gain optical access to both early time and later time flow structures. A 2184 × 1470 CCD array Apogee 32ME with 3 × 3 on-chip binning was used to acquire early times, including the ICs. The binning was performed to increase signal intensity and results in a 728 × 490 image. This camera is labeled "IC" in Figures 2.1 and 2.2, and is tilted with respect to the measurement plane to gain optical access to the initial conditions. Later times were acquired with an Apogee Alta U-42 camera with a 1024 × 1024 CCD array, labeled "DYN" in Figures 2.1 and 2.2, aligned orthogonally to the measurement plane. Each camera is equipped with a Tamron SP Macro lens with a focal length of 90 mm, and a visible-light interference filter

to prevent contamination of the fluorescence signal by the 532 nm light scattered off the glycol particles. Both PLIF cameras provide high resolution images with about 50.5 μm/pixel. The shutters for both cameras are relatively slow, and therefore are triggered to open just before the signal that triggers the solenoid-driven blades to rupture the diaphragm and generate the shock wave. The shutters were timed to remain open for 0.5 s and 1 s for the IC and DYN cameras, respectively, before closing.

With only two PLIF laser pulses available for each experiment, the pulses could be timed to acquire two dynamic images, or one dynamic image and one IC image. Although it is widely accepted that PLIF is a non-intrusive imaging technique, it was discovered in a previous experiment that illuminating the initial conditions with a UV laser pulse prior to shock arrival appeared to alter the post-shock flow, causing structures to appear more blurred. In-depth discussion of this topic is beyond the scope of this document, and should be an object of future study, but some notes and a visual illustration can be found in Appendix A. To avoid influence of this effect on the data set, only those post-shock images acquired in the absence of IC visualization were included in the analysis.

For PIV, the 532 nm light sheet scatters (Mie scattering) off the fog tracer particles, which were measured to be $\sim 0.5$ μm in diameter on average. The PIV laser provided two pulses per run of the experiment, which were spaced 2 μs apart for $M = 1.21$, and 1 μs for $M = 1.36$, 1.50 experiments. The two images are captured on separate frames of a single Kodak Megaplus ES 4.0/E cross-correlation camera with a 2048 $\times$ 2048 CCD array, labeled "PIV" in Figures 2.1 and 2.2, yielding two images per experimental run with a resolution of 16.1 μm/pixel. The fluorescence from the PLIF diagnostic is removed by placing a Raman notch filter centered at 532 nm in front of the lens. The two images are then processed to provide a single velocity field for each run of the experiment. For optical access to earlier times, the

PIV camera was also aligned non-orthogonally to the imaging plane. To preserve focus across the entire image, this camera was equipped with a Scheimpflug mount that allows for misalignment of the lens to the body of the camera. To obtain simultaneous PIV/PLIF measurements, the PIV laser pulses occurred before and after one of the PLIF laser pulses. Simultaneous PIV/PLIF is a key advantage in this study because fog visualization for measurements of species concentration is inferior to acetone PLIF in that the fog droplets fail to follow the diffusion of the $SF_6$ in the initial conditions, and lag behind the initial impulsive acceleration of the $SF_6$ curtain. However, once the droplets are accelerated, they accurately trace the flow for velocity field measurements [42, 44]. Therefore, the implementation of simultaneous PIV/PLIF can provide velocity measurements without compromising the resolution and fidelity of concentration measurements.

A small number of experiments were also performed to obtain PIV in the $x$-$z$ plane located at the center of the center cylinder. This was accomplished by rotating the PIV laser sheet 90 degrees and positioning the PIV camera orthogonally to the imaging plane to view through a side window in the test section. A schematic for the PIV camera viewpoint can be found in Figure 2.9. For these "vertical PIV" measurements, the PIV camera yielded images with 21.5 μm/pixel resolution. Vertical PIV data was acquired for un-shocked ICs and for early time experiments for each Mach number. For ICs the laser pulses were spaced 10 μs apart, while for $M$= 1.21, 1.36, and 1.50, the laser pulses were spaced 2, 1, and 1 μs apart, respectively.

All four laser heads and the PIV camera are triggered off the rise in the signal by the passage of the shock wave across the pressure transducer located immediately upstream of the test section, labeled "3" in Figure 2.1.

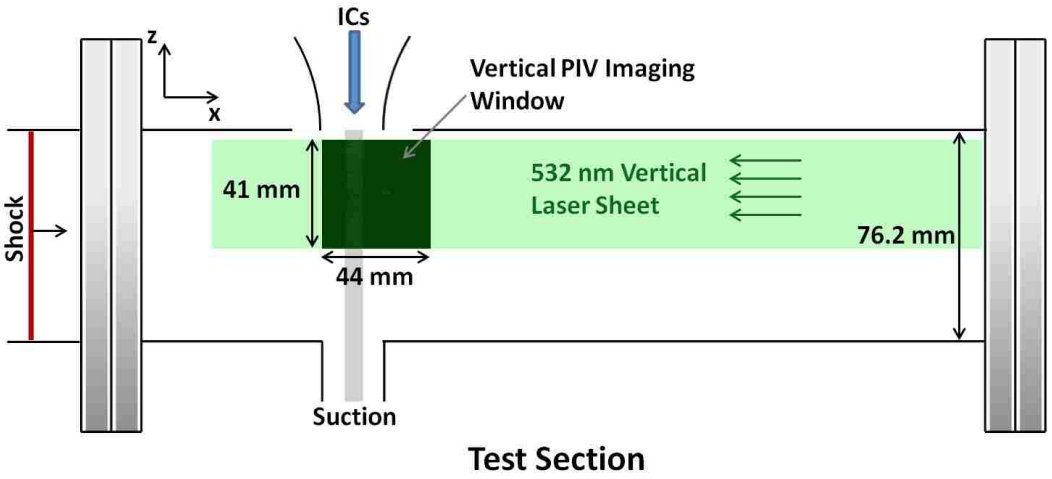


Figure 2.9: PIV camera field of view for vertical PIV measurements. The vertical laser sheet was positioned at the spanwise center of the test section to visualize the center of the center cylinder constituting the gas curtain. The field of view extends from $z$ = -5 to -46 mm with $z = 0$ at the top wall of the shock tube. Field of view extends 3.5 cm in the streamwise $x$ direction from the initial condition location.

## 2.3 Mach Number Variability

In this study, the evolution of the RM instability is compared between experiments at different Mach numbers with nominally identical initial conditions. Varying the Mach number is accomplished in two ways that are practical in the current experimental facility: varying the driver pressure and changing the driver gas. For increasing Mach numbers, the required driver pressure increases exponentially for a given driver gas, but the shock speed is also determined by the specific heat ratio, $\gamma$, of the driver gas. The pressure that is required to reach a given Mach number changes according to the following equations [14]:

$$M_s = \sqrt{\frac{(\gamma_1 - 1) + (\gamma_1 + 1)(p_2/p_1)}{2\gamma_1}} \tag{2.1}$$

where $M_s$ is the desired Mach number, $p_1$ and $p_2$ are the pressures ahead of the shock wave (atmospheric pressure) and behind the shock wave, respectively, and $\gamma_1$ is the

specific heat ratio of the atmospheric air. Then,

$$\frac{p_2}{p_1} = x = \frac{2\gamma_1 M_s^2 - (\gamma_1 - 1)}{\gamma_1 + 1} \tag{2.2}$$

Finally, the driver pressure, $p_4$, required to achieve $M_s$ is,

$$p_4 = p_1 x \left[ 1 - \frac{(\gamma_4 - 1)(\frac{a_1^*}{a_4^*})(\frac{p_2}{p_1} - 1)}{\sqrt{2\gamma_1[(\gamma_1 - 1) + (\gamma_1 + 1)(\frac{p_2}{p_1})]}} \right]^{\frac{2\gamma_4}{\gamma_4 - 1}} \tag{2.3}$$

where $\gamma_4$ is the specific heat ratio of the driver gas, and $a_1^*$ and $a_4^*$ are the speed of sounds in the atmospheric air and the driver gas, respectively, defined as

$$a^* = \sqrt{\gamma RT/m} \tag{2.4}$$

where $R = 8.314$ J/(mol*K) is the gas constant, $T$ is the temperature, and $m$ is the molecular mass in kilograms per mol. This yields 346 m/s for the speed of sound in air at room temperature. From the equations above, it can be shown that the higher the $\gamma$ of the driver gas, the less pressure is required to achieve the same Mach number. Traditionally, the shock tube at Los Alamos has operated at $M = 1.2$ using nitrogen as the driver gas with $\gamma_{N_2} = 1.4$, but helium has $\gamma_{He} = 1.67$, making it more desirable to be used as a driver gas to achieve higher Mach numbers. In Figure 2.10 the curves for Mach number *versus* required driver gauge pressure are given for both nitrogen and helium at 7100 ft, which was determined to be the elevation of the experimental facility in Los Alamos using a hand held GPS unit. At 7100 ft and room temperature, the atmospheric pressure, $p_1$, is approximately 11.46 psi. It can be seen that the effect of varying $\gamma$ is significant. For example, to achieve Mach 2.0, the required driver gauge pressure for nitrogen is approximately 360 psig, while it is only approximately 100 psig for helium. Therefore, for $M = 1.36$ and 1.50, helium was chosen for the driver gas, as it would lower the material stresses in the shock tube and promote personal safety (the shock tube has a maximum allowable driver gauge pressure of 350 psig based on pressure safety reviews).

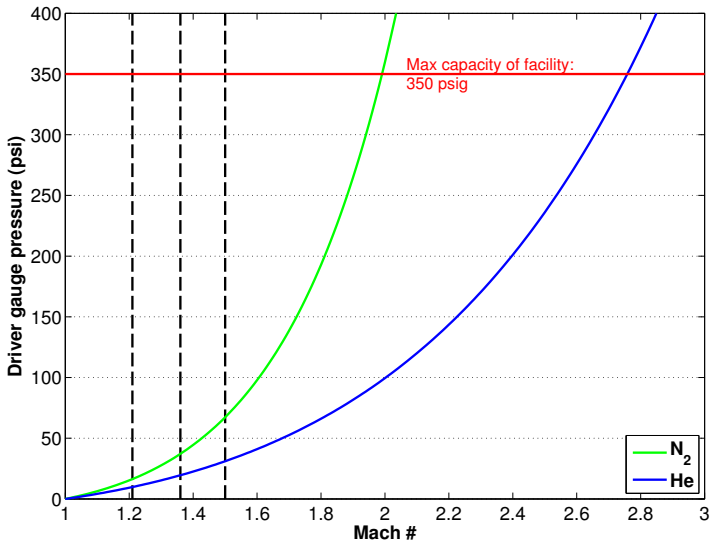


Figure 2.10: Mach number *vs.* required driver pressure for nitrogen and helium. Maximum allowable pressure for the facility is 350 psig. Vertical lines represent Mach numbers of shock waves from the current experiment: $M = 1.21$, 1.36, and 1.50.

Experimentally, it was found that to generate Mach 1.21, Mach 1.36, and Mach 1.50 incident shock waves, driver pressures of approximately 22 psig, 30 psig, and 50 psig, respectively, were required. These values contrast with the calculated theoretical values of 16.4 psig, 19.5 psig, and 31.0 psig. Therefore, the theoretical required driver pressure was between 75%, 65%, and 62% that of the experimentally determined driver pressure for $M = 1.21$, 1.36, and 1.50 experiments, respectively. It is believed that this was mainly due to several losses incurred during the shock generation process, including the imperfect rupture of the diaphragms, and boundary layer effects. Also, the solenoid-driven razor blades take up a significant cross section of the driver section near the diaphragm location. This blockage between the driver section and driven section could be the cause of additional mechanical/aerodynamic losses as the pressure waves initially form into a shock wave.

Some of the discrepancy in the two higher Mach number cases occurs because

air is not evacuated from the driver section prior to pressurizing above atmospheric pressure with helium, so the driver gas consists not only of helium, but also a small fraction of air. Because the specific heat ratio of air ($\gamma$=1.4) is smaller than that of helium ($\gamma$=1.67), the operating specific heat ratio is really a weighted average of the two gasses, having the effect of increasing the required driver pressure in the experiment above what is calculated for pure helium. In previous experiments using helium ($\gamma$=1.67) as the driver gas with the same experimental setup (not reported here), a driver pressure of 15 psig was required for the generation of a Mach 1.21 shock wave, while only 10 psig (66%) is required according to theory. Because nitrogen and air have the same specific heat ratio, and because there is only a small difference in the speed of sound between $N_2$ and air, the losses in the case of nitrogen as the driver gas can only be explained by the mechanics described earlier. Since the theoretical driver pressure for nitrogen is about 75% that of the experimental value, and for helium it is about 65%, it is speculated that the extra 10% error in the helium cases is a result of not using the weighted average of the specific heat ratio in calculations. In this interpretation, the remaining discrepancy of approximately 25% is due to the mechanisms listed above.

While using helium for the driver gas allows for higher Mach numbers, it comes at the expense of a faster traveling expansion fan, which arrives at the test section in much less time than when nitrogen is the driver gas. In this facility, according to theoretical calculations using pure driver gas constitutions, the expansion fan would interact with the moving mixing layer at $\sim t = 7000$ µs, $t$=1400 µs, and $t$=900 µs for $M = 1.21$, 1.36, and 1.50, respectively. The much longer time for Mach 1.21 reflects that nitrogen was used as the driver gas in those experiments. The interface also eventually encounters a second shock wave which travels upstream after reflecting off the end wall of the end section. Theoretically, this reshock event occurs at $\sim t = 2900$ µs, $t$=2500 µs, and $t$=2150 µs for $M = 1.21$, 1.36, and 1.50, respectively. For Mach 1.21, these interactions are not concerning, as the earlier reshock event occurs 200

μs after the latest image acquisition at 2700 μs. For the two higher Mach number cases, the reshock occurs much later than the latest image acquisitions of $t = 1700$ μs ($M = 1.36$), 1250 μs ($M = 1.50$), however, according to 1-D gas dynamics, the expansion fan arrives earlier than these image times. Of course, it is expected that experimental factors will cause the dynamics of the pressure waves to deviate from the 1-D calculations. In addition to the factors described above, there are also openings in the test section for the in and out flow of the initial conditions, which will cause shock reflections and expansions.

To know the effects of all of these factors, one would need to perform a numerical simulation of the full geometry of the shock tube. In the absence of that information one must rely on the traces from the pressure transducers. Figures 2.11, 2.13, and 2.15 show representative traces from each of the 4 pressure transducers for each Mach number experiment in addition to the trace from the UV laser power meter. From the traces it appears that the primary expansion fan from the driver section arrives at the IC location, which is coincident with pressure transducer number 4 (PT4), at 5500 μs, 1800 μs, and 1500 μs in order of increasing Mach number. These times are all after the latest image acquisitions, even before accounting for the extra time required to catch the moving mixing layer. This information is summarized in Table 2.1. Additionally, there was no other experimental evidence that the expansion fan ever interacted with the evolving curtain, based upon its steady convection velocity and a lack of an unexpected change in flow evolution. With this information it is concluded that all data was acquired in all experiments before the arrival of either the reshock or the expansion fan.

Figures 2.12, 2.14, and 2.16 show $x$-$t$ (position versus time) diagrams with shock waves, reflected shock waves, and expansion fans, for $M = 1.21$, 1.35, and 1.50 generated using code developed at the University of Wisconsin and altered to the specifications of the experimental conditions in the current study. Indicated in each

Table 2.1: Table summarizing driver section pressures ($p_4$), and experimental and theoretical times after first shock arrival at PT4 for various events. Theoretical values were calculated using 1-D gas dynamics.

| | | **Mach 1.21** | **Mach 1.36** | **Mach 1.50** |
|---|---|---|---|---|
| **Fill Gas** | | $N_2$ | He | He |
| $\mathbf{p_{4,expt}}$ | (psig) | 22 | 30 | 50 |
| $\mathbf{p_{4,theory}}$ | (psig) | 16.4 | 19.5 | 31 |
| $\mathbf{\Delta t}$ **latest image** | (μs) | 2700 | 1700 | 1250 |
| $\mathbf{\Delta t_{expt}}$ **expansion fan** | (μs) | 5500 | 1800 | 1500 |
| $\mathbf{\Delta t_{theory}}$ **expansion fan** | (μs) | 7000 | 1400 | 900 |
| $\mathbf{\Delta t_{expt}}$ **reshock** | (μs) | 4000 | 3800 | 3600 |
| $\mathbf{\Delta t_{theory}}$ **reshock** | (μs) | 2900 | 2500 | 2150 |

$x$-$t$ diagram is the location of the interface within the test section and an overlay of the rise in each pressure transducer signal (squares) giving the general space-time of an experimental run. It can be seen that the rises in the signals of the pressure transducers agree very well with the computational code for the incident shock, but that the correlation falls off for the reflected shock wave. This discrepancy can probably be explained by losses that occur in the experiment that are not accounted for in the idealized code as the experimentally measured reflected shock wave is slower than that according to 1-D gas dynamics. It is hypothesized that most of the losses occur due to openings in the test section. It is also likely that other losses occur at the end wall where the shock wave is not perfectly reflected in the experiment.

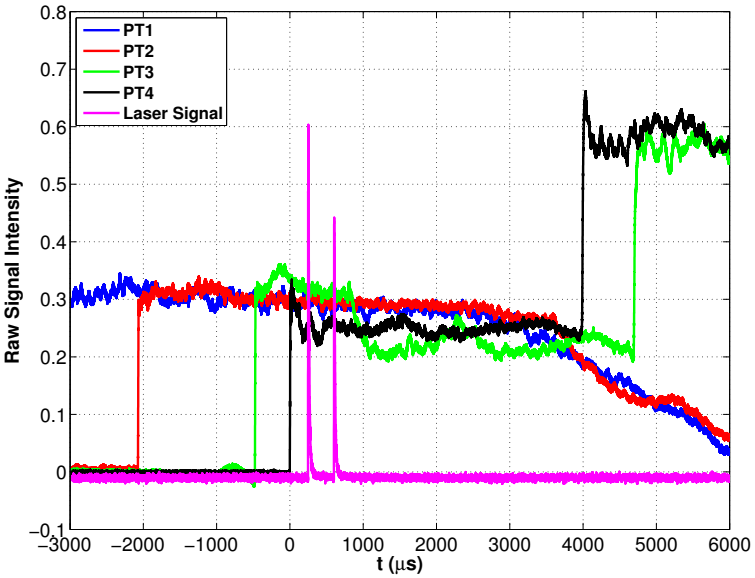


Figure 2.11: Pressure transducer and UV laser power traces for a sample Mach 1.21 experiment. Timing here is set to take PLIF images at 250 and 600 μs after shock interaction at PT4 (IC location).

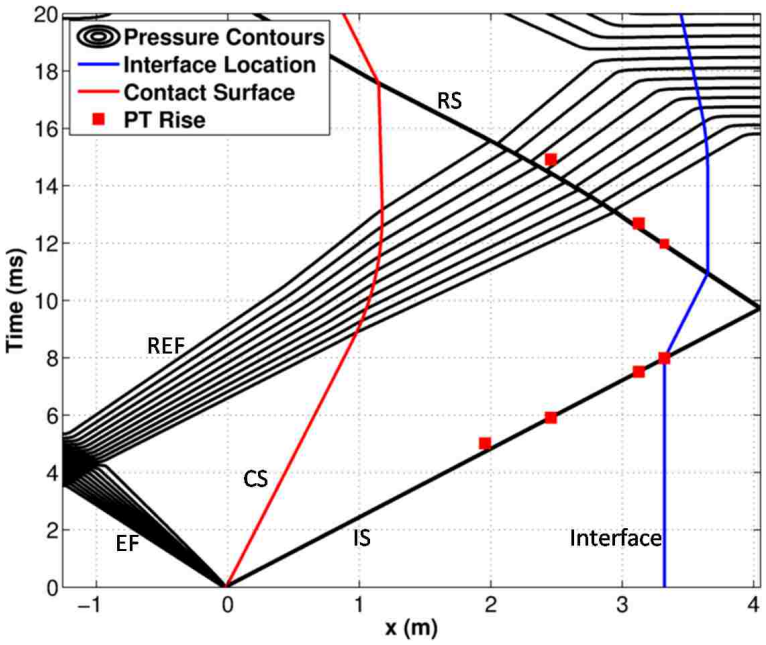


Figure 2.12: Theoretical $x$(m)-$t$(ms) wave diagram for Mach 1.21 [52] with experimental pressure trace rises overlaid (red squares). $x = 0$ is the location of the diaphragm. IS, incident shock; RS, reflected shock; EF, expansion fan; REF, reflected expansion fan; CS, contact surface; Interface, location of the gas curtain.

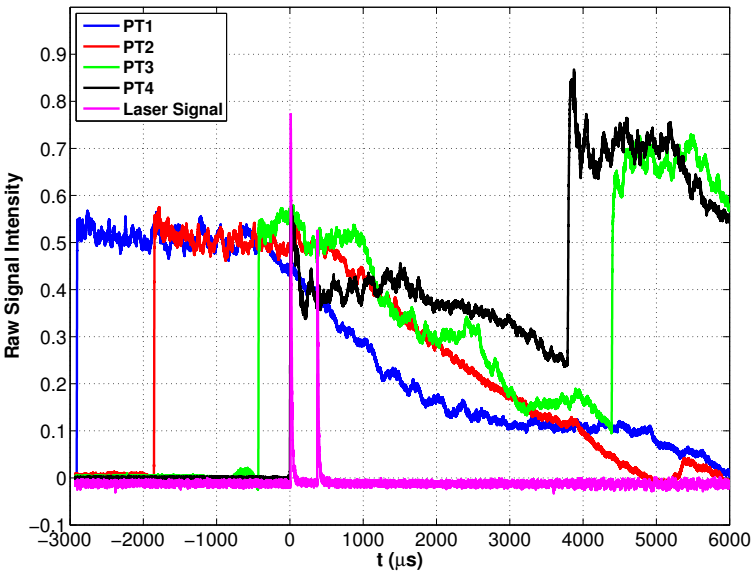


Figure 2.13: Pressure transducer and UV laser power traces for a sample Mach 1.36 experiment. Timing here is set to take PLIF images at 10 and 375 μs after shock interaction at PT4 (IC location).

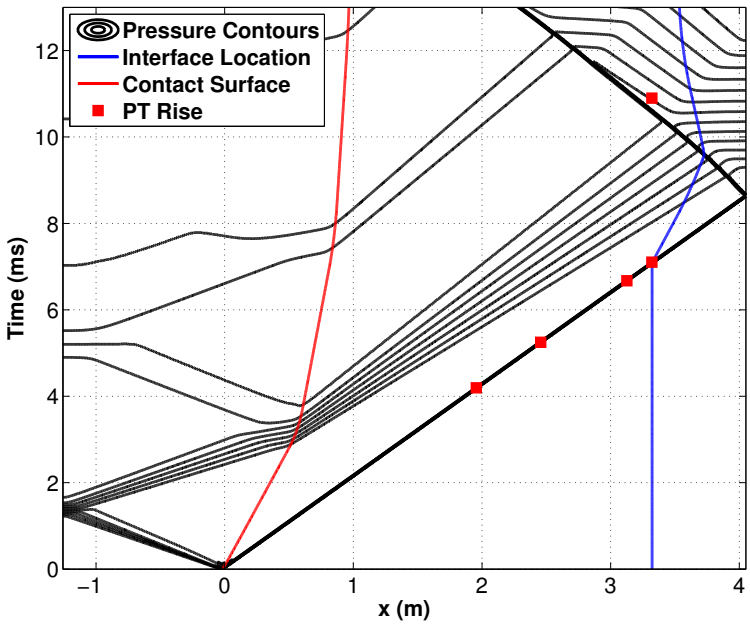


Figure 2.14: Theoretical $x$(m)-$t$(ms) wave diagram for Mach 1.36 [52] with experimental pressure trace rises overlaid (red squares). $x = 0$ is the location of the diaphragm.

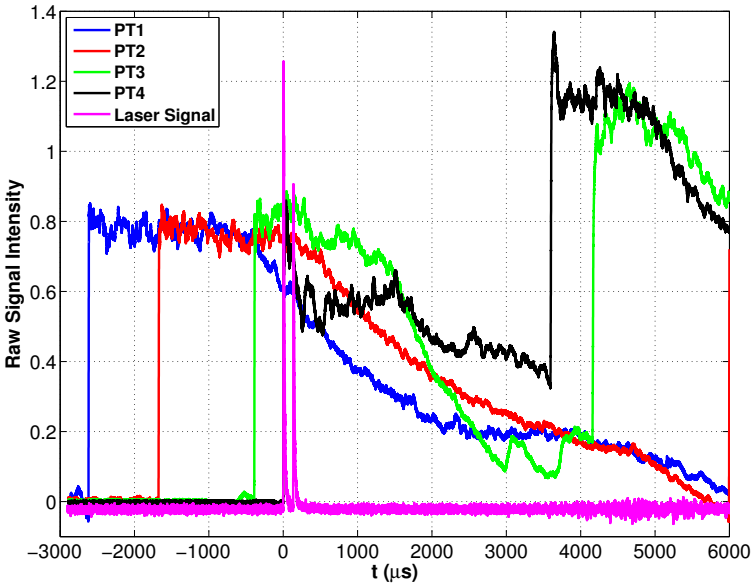


Figure 2.15: Pressure transducer and UV laser power traces for a sample Mach 1.5 experiment. Timing here is set to take PLIF images at 20 and 150 μs after shock interaction at PT4 (IC location).

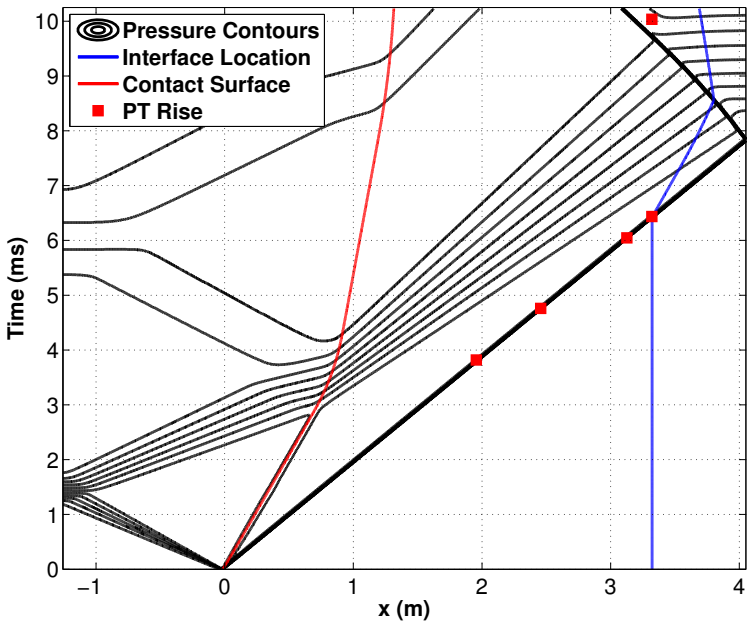


Figure 2.16: Theoretical $x$(m)-$t$(ms) wave diagram for Mach 1.50 [52] with experimental pressure trace rises overlaid (red squares). $x = 0$ is the location of the diaphragm.

# Chapter 3

# Image Processing

## 3.1 Quantitative PLIF Processing

The raw PLIF images are 2-D maps of fluorescence intensity which scales linearly with acetone concentration (volume fraction), $c_v$, in the power output range of the PLIF laser. To convert the images to quantitative density maps requires acquisition of very careful calibration data while conducting experiments and several processing steps thereafter. Quantitative PLIF (QPLIF) is very difficult to obtain experimentally because, as a general rule, if any component of the imaging diagnostics changes before the relevant calibration data has been collected, then it is very likely that QPLIF will no longer be possible. Such changes encountered in the current experimental setup include camera positioning, camera focus, background light contamination, test section optical window cleanliness, laser intensity, and laser spatial variations (due to both laser output and the degradation of external optics).

The first step in calibrating the PLIF images is to subtract backgrounds to remove noise due to ambient light sources in the laboratory. In general, background images were taken approximately every 10 runs of the experiment or whenever camera po-

sition was changed to visualize a different downstream location. To reproduce the reflections and scattering of the laser sheet within the test section, the background images were acquired while pulsing each laser head once. The exposure duration of each camera was set equal to those of the experiments (0.5 s and 1 s for IC and DYN cameras, respectively).

The next step is to correct for variations in the uniformity of the laser sheet. In this study, it was found that the spanwise laser sheet variations were significant, introducing both long and short wavelength intensity variations in resulting images on the order of +/- 50% from the median intensity value. It was decided that this had to be corrected for as well as could be achieved using images of the laser sheet acquired through use of a custom made calibration test cell. The test cell, shown in Figure 3.1, is a lexan and glass box that can be filled with the heavy gas mixture directly from the settling chamber. It was designed so it could be positioned at any streamwise location in the path of the laser sheet. For imaging, the cell is oriented so that laser light enters the test cell through UV transparent window 1 and exits through UV transparent window 2, each composed of fused silica. The second UV window helps to minimize the amount of UV light that is backscattered into the test cell, which could contribute noise to the calibration signal. The bottom side of the test cell is a glass window to provide optical access for both PLIF cameras. The window is the same as those that make up the test section to reproduce the fluorescence signal attenuation that occurs in the actual experiment.

The test cell was filled by flowing heavy gas in from the bottom and allowing outflow from the top so that the air could be evacuated. The subsequent steady flow of heavy gas through the test cell also helps to reproduce the temperature of the ICs in the actual experiment, which has an effect on the intensity of acetone fluorescence [53]. Once the test cell was uniformly filled, a spatial map of the light sheet could be obtained, as demonstrated in Figure 3.2, for both laser heads at

each camera position. As the light travels through the gas filled test cell, the signal attenuates according to Beer's Law. Also as the light sheet propagates from the end section to the initial conditions, it fans out in the spanwise direction making it necessary to calibrate for the spanwise laser sheet variations at each streamwise location within a given image for each camera location. After passing the calibration images through a median filter and an adaptive linear filter to reduce noise, a row by row function is constructed that will remove the spanwise variations along each row. This function is then applied to all images of the flow field acquired at the corresponding camera position.

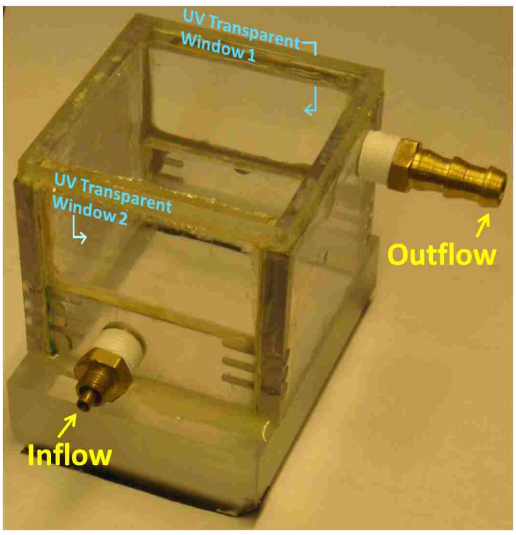


Figure 3.1: Photograph of test cell used for spanwise laser variation and volume fraction calibrations.

Data were taken on about 50 different days with slight movements of both cameras with respect to the laser sheet occurring uncontrollably over time. Since calibration test cell data was not acquired for each position on each day, adjustments had to be made in the calibration data. This included shifting the calibration images in the spanwise direction to achieve an optimized best fit to the experimental images acquired on certain days. Moreover, small scale spanwise variations in the laser

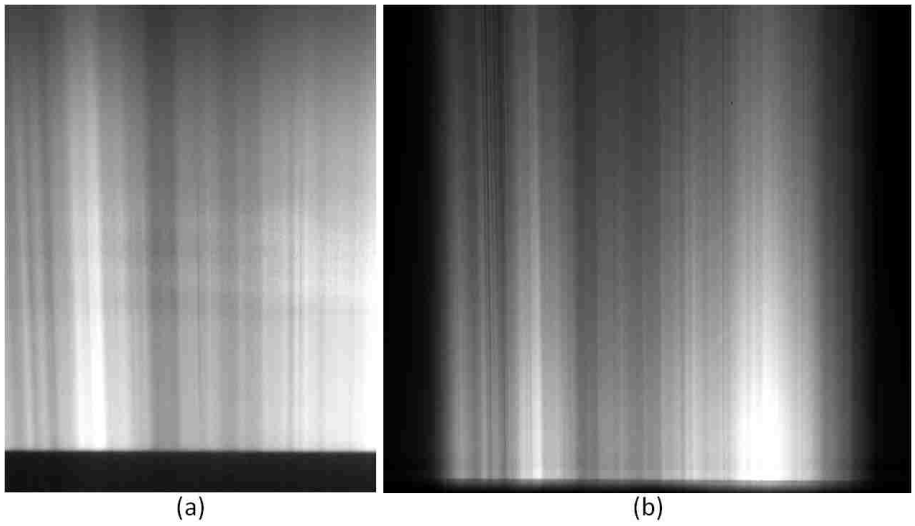


Figure 3.2: PLIF imaging of the laser sheet using the calibration test cell, with background subtracted. *Left*: IC camera; *Right*: DYN camera

sheet from head 2 were inconsistent from pulse to pulse, making it impossible to fully correct those PLIF images. Consequently, in many images (especially later-time images), one can still make out small-scale laser sheet striations, but they are relatively small in magnitude compared to pre-processed images. Figure 3.3 demonstrates the fidelity of the spanwise laser sheet correction in an IC image and a late time dynamic image. Figure 3.4 shows streamwise centerline profiles of the IC images (a) and (c) from Figure 3.3, as well as a line profile of the laser sheet image (a) in Figure 3.2 at the same CCD location. Each of the profiles is normalized by the maximum value. The peaks in the intensity signal from the raw image follow the trend of the laser sheet variations in the spanwise direction ($y$). After correction, the calibrated image produces consistent peak values for each wavelength, all around a normalized value of one.

After background subtraction and spanwise laser sheet variation correction, the images must still be converted from intensity to concentration. From infrared spectroscopy, the volume fractions of the gases in the settling chamber are known to

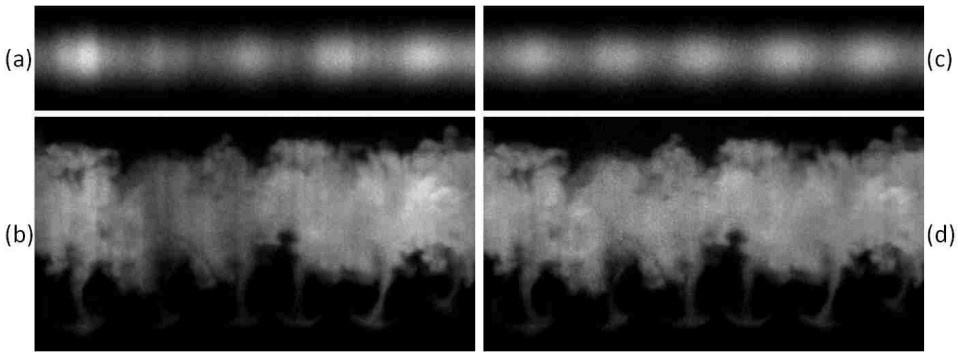


Figure 3.3: PLIF images of *Left*: (a) ICs before laser sheet correction, and (b) an image from a Mach 1.50 experiment at 1200 $\mu$s before laser sheet correction. *Right*: The same images after correction.

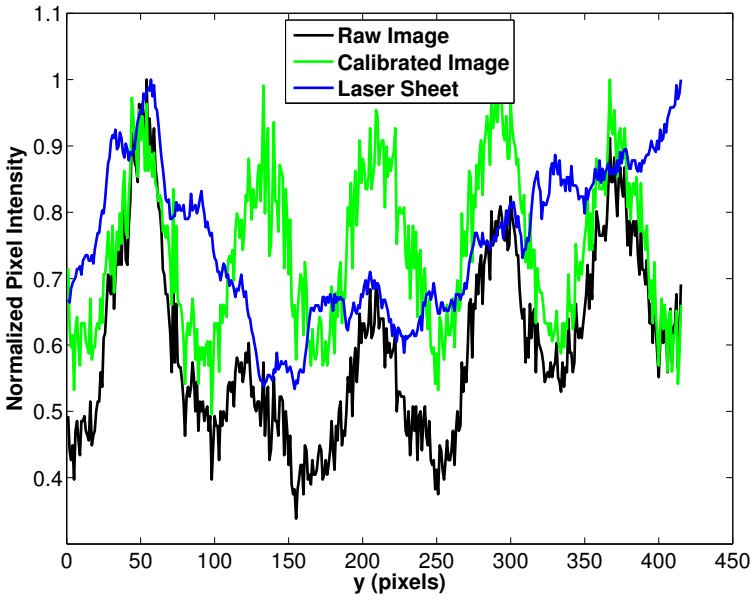


Figure 3.4: Normalized intensity profiles along the center line of the IC image before (Figure 3.3 (a)) and after spanwise correction (Figure 3.3 (c)), and a line profile of the laser sheet shown in Figure 3.2 (a) at the same pixel location.

be 75%/20%/5% for $SF_6$/acetone/air, respectively. Since the calibration test cell is filled directly from the settling chamber it is assumed that the volume fractions are the same. Using the calibration image from the IC camera, a single PLIF IC image was calibrated by taking the ratio of the IC image to the highest intensity region of the calibration image (near the side of the test cell where laser light enters) and multiplying by 75%. The resulting field represents the volume fraction of $SF_6$.

This reference IC image and all other IC camera images were then corrected for the perspective error (arising from the nonorthogonal alignment of the camera to the imaging plane) by using a MATLAB second-order polynomial transform called "cp2tform." This function requires a set of control point pairs to build the function that will map the distorted image (Figure 3.5 (a)) onto some reference image. To ensure equivalent image resolution for ease of subsequent data analysis, the calibration grid associated with the DYN camera was chosen as the reference orthogonal grid (Figure 3.6), and 11 control point pairs were manually selected to build the mapping function. The fidelity of the mapping function was verified by applying the function to the IC calibration grid image itself, which is shown in Figure 3.5 (b). It deserves note that the focus was not preserved across IC camera images because a Scheimpflug mount was not used on this camera. This resulted in a narrow focused region which was centered around the IC location. Therefore, early time dynamic images captured by this camera are slightly out of focus. While this should not have a significant effect on quantities such as mixing layer width and total intensity, it does have an impact on quantities based on gradients.

The final step is to use the principle of mass conservation to convert the rest of the images to volume fraction. This was accomplished by equating the sum of the intensity field in each image with that of the calibrated and transformed reference IC image. Ideally, this step accounts for differences in fluorescence due to post-shock temperature increases, differences in the response of the two cameras, and differences

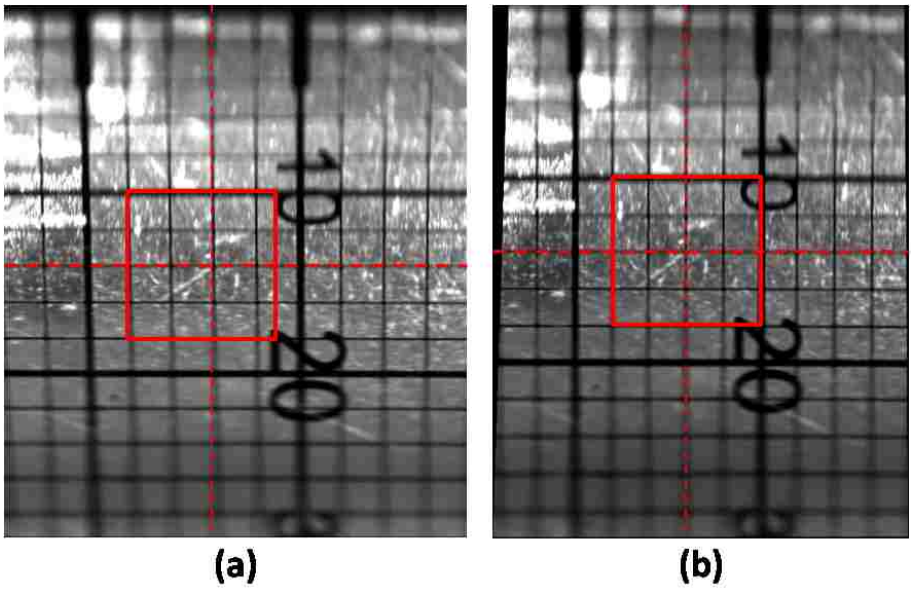


Figure 3.5: Demonstration of correction for IC camera perspective error, with (a) an image of the calibration grid before correction, and (b) the same image after applying a second-order polynomial transform function based on the orthogonal grid in Figure 3.6. Red squares are drawn on each image to emphasize fidelity of the mapping.

in laser intensity from pulse to pulse without requiring the relevant calibration data. Of course it relies upon several assumptions including that the laser light sheet thickness is roughly constant with streamwise position, the mass of the heavy gas within the imaging plane of the ICs is the same for each run of the experiment, and that the flow is mostly 2-D so that the amount of mass leaving or entering the measurement plane is negligible within a given experiment. The resulting $SF_6$ volume fraction maps can then be easily converted to mass fraction, $c_m$, or density, $\rho$.

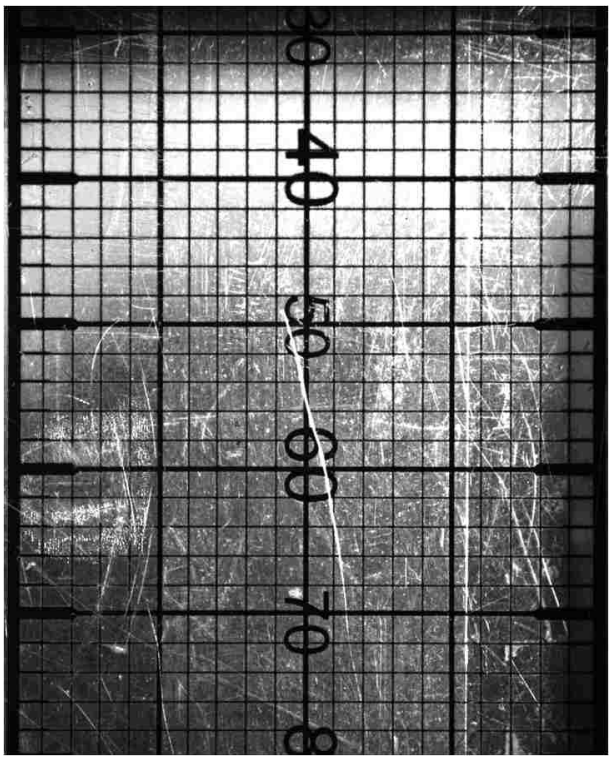


Figure 3.6: Calibration grid for the DYN camera. Served as the control image for the orthogonal mapping of IC camera images.

## 3.2 PIV Processing in the $x$-$y$ Plane

PIV image processing requires less measurement precision and calibration than is required for QPLIF image processing. To produce accurate velocity fields from PIV images, the raw particle images are first corrected for the perspective error arising from the nonorthogonal alignment of the PIV camera to the imaging plane. As with the PLIF images, the raw particle images are transformed using a MATLAB second-order polynomial mapping function called "cp2tform." To select the base-point pairs required for the transform, an orthogonal grid was generated with approximately equivalent grid spacing as the calibration grid image in Figure 3.7 (a). About 30 control point pairs were manually selected on the original calibration image and the

computer generated orthogonal grid to create the mapping function. The function was then applied to each raw particle-field image. The fidelity of the mapping function was verified by applying the function to the calibration grid image itself, which is shown in Figure 3.7 (b). A red square is placed in each image in Figure 3.7 to emphasize the effect of the transformation.

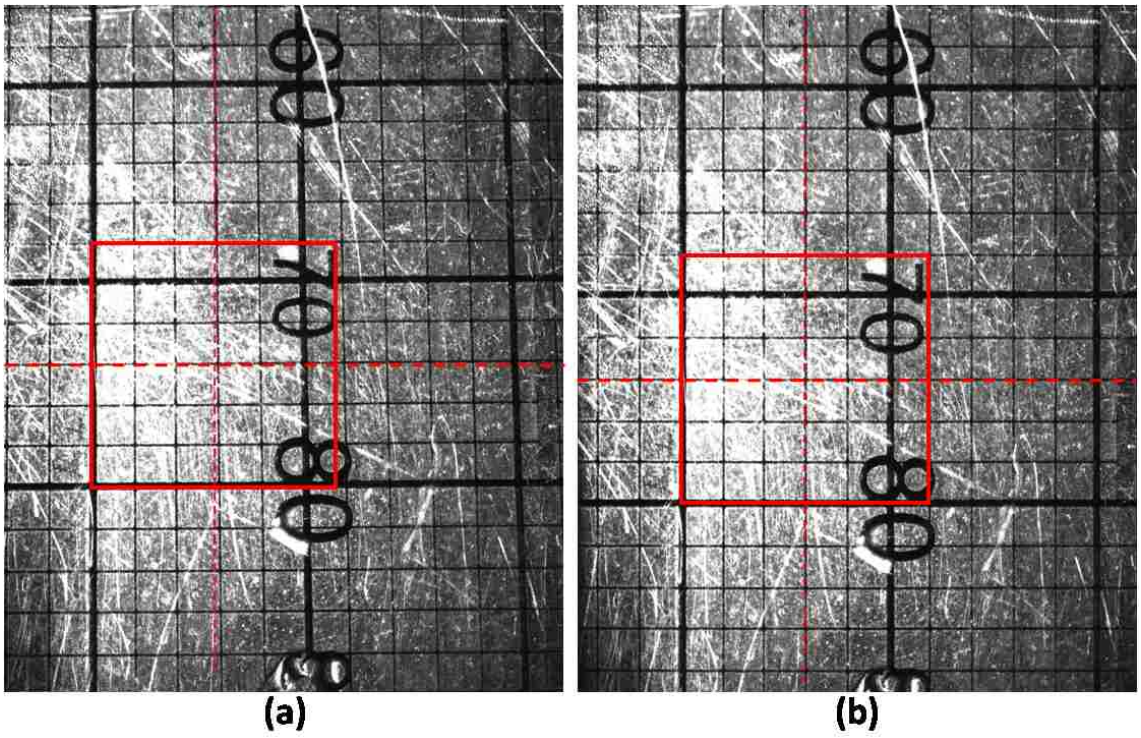


Figure 3.7: Demonstration of correction for PIV camera perspective error, with (a) an image of the calibration grid before correction, and (b) the same image after applying a second-order polynomial transform function based on a computer generated orthogonal grid. Red squares are drawn on each image to emphasize fidelity of the mapping.

The resulting transformed PIV image pairs were then processed using Insight 3G software (ver 9.1.0.0) with a recursive Nyquist processor with 50% overlap, a starting window size of 64 × 64 pixels, and a final window size of 24 × 24 pixels. This provides a vector spacing of 193 μm/vector. Vectors that did not pass a median test over a 3 × 3 neighborhood were replaced by secondary correlation peaks in some instances.

After processing, a mild Gaussian vector-smoothing filter was applied with $\sigma = 0.8$ over a $5 \times 5$ neighborhood. To determine the appropriate window size, a resolution study was performed. A late time Mach 1.50 image with good seeding density was chosen as the test case, as it was expected to have the highest level of chaotic motion, and therefore present the greatest challenge to the processing scheme. A well seeded region of the mixing layer was then processed with all available final window sizes ($8 \times 8$, $16 \times 16$, $24 \times 24$, $32 \times 32$, and $40 \times 40$). It was found that $24 \times 24$ was the smallest window processing size that did not produce bad vectors. Also, a qualitative inspection of the vorticity maps produced by each processing size shows $24 \times 24$ to have the highest level of detail without introducing noise into the measurement, as seen in Figure 3.8. The values of many quantities of interest (which are discussed in Chapter 4) were also compared between $24 \times 24$ and $32 \times 32$ final processing window sizes, and helped to confirm that $24 \times 24$ was the right choice given the resolution and particle seeding of the raw data. Specifically, changing the window size did not have a significant effect on the mean streamwise velocity, the values for circulation, or the trends in any of the measured parameters. With $24 \times 24$, the values for turbulent kinetic energy estimates, and mean positive vorticity were approximately 10% and 12% higher, respectively, than for $32 \times 32$ processing. These results, along with the methodology, are similar to those reported in Balakumar *et al.* [54].

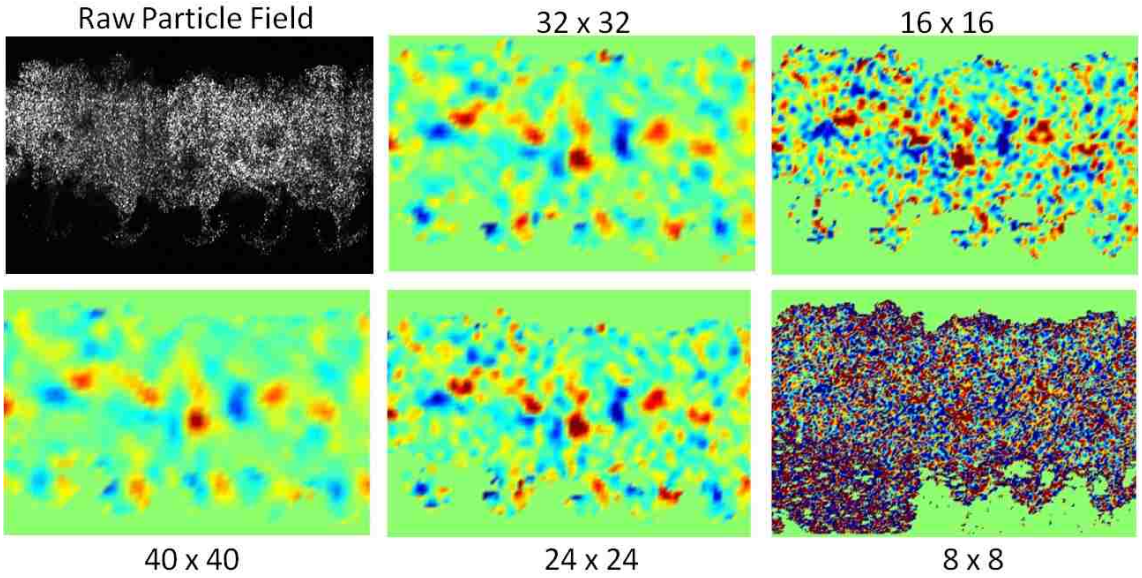


Figure 3.8: An image of a raw particle field acquired at 1050 μs in a Mach 1.50 experiment, and the vorticity maps obtained given various window sizes used for PIV processing.

## 3.3 PIV Processing in the $x$-$z$ Plane

Vertical PIV measurements did not require transformation prior to processing, as the PIV camera was aligned orthogonally to the imaging plane. Image pairs were all processed using Insight 3G software with a recursive Nyquist processor with 50% overlap. Starting and final window sizes were set equal at 24 $\times$ 24 pixels. This provided a vector spacing of 258 $\mu$m/vector. Vectors that did not pass a median test over a 3 $\times$ 3 neighborhood, were replaced by secondary correlation peaks in some instances. After processing, a mild Gaussian vector-smoothing filter was applied with $\sigma = 0.8$ over a 5 $\times$ 5 neighborhood.

# Chapter 4

# Results

The fluid dynamics in the current study are dominated by pairs of closely spaced, interacting vortices generated through baroclinic vorticity deposition. As the initial amplitudes on either side of the curtain grow, the vorticity rolls up and distorts the fluid interfaces to interact with adjacent vortices, giving rise to complex flow features that are highly dependent upon the initial conditions. The growth of initial perturbations should also be nonlinear for essentially the entire duration of the experiment not only because of interaction between the two closely spaced interfaces, but also because the initial amplitudes ($a_0$) on both interfaces are on the same scale as the wavelength of the perturbations ($ka_0 \approx 1$). Figure 4.1 gives a visual description of the flow feature nomenclature used in this report, while a list of parameters that govern the flow can be found in Table 4.1.

The current data was acquired through over 1600 runs of the experiment, yielding approximately 3200 PLIF images. By changing laser pulse timings from one run to the next, it is possible to construct an extensive time sequence of the evolving instability for each Mach number. In general, the experiments were performed to capture several images at each time step to get a measure of the variability introduced

by the initial conditions and small changes in shock speed from shot to shot. The images are then analyzed and classified based on both qualitative and quantitative criteria (i.e. structure symmetry, structure shape, seeding density, shock speed) to determine whether to include in the data set. In total, 507 individual PLIF images and 174 PIV image pairs met these selected requirements.

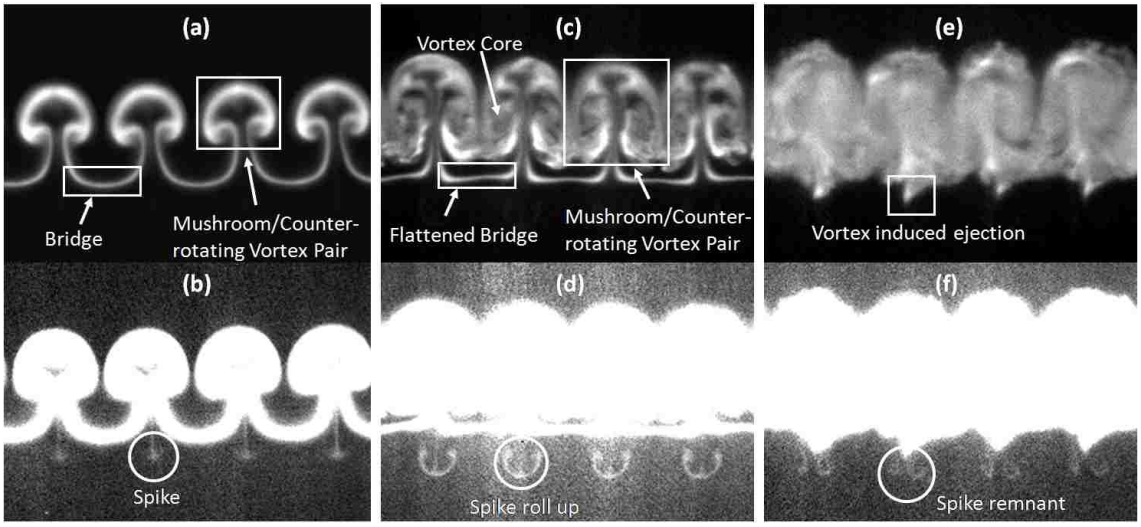


Figure 4.1: Sample density maps from Mach 1.50 experiments indicating flow field nomenclature used in the body of the text. Along the top row, (a), (c), and (e) were acquired at 125, 300, and 475 μs, respectively, while (b), (d), (f) along the bottom row are the same images with contrast adjusted to visualize the spike features.

## 4.1 PLIF Time Series Comparison

As was discussed in Chapter 2, only two PLIF laser pulses are available for each run of the experiment. Therefore, to investigate how the RM instability evolves over time, many runs of the experiment must be carried out, with varying pulse time between shots. In general, multiple experiments were performed at a particular time after shock impact. Then the laser pulse timing is varied, and experiments are performed, resulting in another set of images at a different time, and so on.

Table 4.1: List of parameters governing the flow, including input values used in Eq. 4.1, with $'$ denoting post-shock conditions when ambiguous.

| | | **Mach 1.21** | **Mach 1.36** | **Mach 1.50** |
|---|---|---|---|---|
| $\boldsymbol{\Delta v}$ | (m/s) | 104 | 158 | 222 |
| $\boldsymbol{\delta_0}$ | (mm) | 3.8 | 3.8 | 3.8 |
| $\boldsymbol{\delta_0'}$ | (mm) | 2.63 | 2.32 | 2.17 |
| $\boldsymbol{\dot{\delta}_0}$ | (mm/μs) | 0.013 | 0.029 | 0.042 |
| $\boldsymbol{\kappa}$ | ($mm^{-1}$) | 1.745 | 1.745 | 1.745 |
| $\boldsymbol{t_{0,Fit}}$ | (μs) | 30 | 20 | 15 |
| $\boldsymbol{\Gamma_{Fit}}$ | ($mm^2$/μs) | 0.045 | 0.055 | 0.062 |
| $\boldsymbol{\Gamma_{Expt}}$ | ($mm^2$/μs) | 0.07 | 0.09 | 0.13 |
| $\boldsymbol{\rho_{air}}$ | (kg/$m^3$) | 0.924 | 0.924 | 0.924 |
| $\boldsymbol{\rho_{air}'}$ | (kg/$m^3$) | 1.255 | 1.496 | 1.719 |
| $\boldsymbol{\rho_{SF_6}}$ | (kg/$m^3$) | 4.657 | 4.657 | 4.657 |
| $\boldsymbol{\rho_{SF_6}'}$ | (kg/$m^3$) | 6.682 | 8.303 | 9.932 |
| $\boldsymbol{A}$ | | 0.52 | 0.52 | 0.52 |
| $\boldsymbol{A'}$ | | 0.53 | 0.54 | 0.56 |
| $\boldsymbol{\nu}$ | ($m^2$/s) | $1.16\times10^{-5}$ | $1.16\times10^{-5}$ | $1.16\times10^{-5}$ |
| $\boldsymbol{\nu'}$ | ($m^2$/s) | $9.3\times10^{-6}$ | $8.2\times10^{-6}$ | $7.5\times10^{-6}$ |

The timings were varied from just before shock impact to as late in time as could be imaged within the test section. This corresponded to $t$= 2700 μs, 1700 μs, and 1250 μs for $M$ = 1.21, 1.36, and 1.50, respectively, where $t$=0 is the moment just before the shock wave reaches the upstream edge of the initial conditions. Early time dynamic images were captured with the IC camera, as the field of view included approximately 14 mm downstream of the initial condition location (the DYN camera did not have optical access to this region). The latest times captured on the IC camera were $t$=125 μs, 75 μs, and 40 μs for $M$ = 1.21, 1.36, and 1.50, respectively. Later times were captured by the DYN camera.

To ensure that the initial conditions remained nominally the same between experiments, structure development was carefully monitored during data acquisition. Dynamic images are highly sensitive to the initial conditions, as small differences get amplified after shock impact. It has been found previously that monitoring

the similarity of the dynamic images can therefore provide more information on IC repeatability than can the IC images themselves. Specifically, investigation of the correlation between the 2-D maps of the ICs has previously failed to differentiate the various differences in flow development observed in similar experiments [47, 50]. Therefore, initial condition similarity was confirmed by periodically repeating experiments with timings and Mach numbers that matched those that had been performed earlier. Additionally, as a general rule, only one of the PLIF laser pulses was varied from one experiment to the next for experiments at a given Mach number. This helped to monitor experimental repeatability in real time, as well as to establish the degree to which variability at one time step is transported to the next time step.

A set of images ordered in time was assembled for each Mach number to visualize the evolution of the single-mode, varicose, heavy gas curtain. These time series consist of 48, 51, and 42 images for $M = 1.21$, 1.36 and 1.50, respectively. $SF_6$ volume fraction maps of these images are shown in Figures 4.2, 4.3, and 4.4 with each image custom contrast for optimum presentation. Figures 4.5, 4.6, and 4.7 are the same images but with a constant contrast of 1% to 30% $SF_6$ volume fraction for all images to provide a sense of how the concentration decreases over time, indicating the degree of mixing. All images are labeled with time after shock interaction (in μs) and distance traveled from the initial condition location (in cm). Due to small differences in the initial conditions, small scale features do not always register from frame to frame. However, the highly repeatable nature of the dynamic images suggests that the initial conditions were more repeatable than those for any previously reported thin heavy gas curtain. Figure 4.8 demonstrates the repeatability of the Mach 1.50 experiments at 3 different post-shock times. The experimental repeatability allows for the tracking of large scale features and some small scale features through their development in time. The data sets used to generate the time series comprise several images at most times, corresponding to different individual runs of the experiment. With multiple shots to choose from at most times, images for each of the time series

were selected based on qualitative registering of flow features, and symmetry within the individual image.

In general, images show the initial conditions at $t = 0$ μs, followed by visualization of the shock wave passage, maximum compression after shock interaction, and the subsequent evolution of the instability. Perturbations on the upstream interface begin to grow immediately after shock interaction, while a phase inversion first takes place on the downstream interface. As the perturbations on either side grow, they begin to interact, leading to flow patterns that are characterized by the classic mushroom shape that is common for the the R-M instability. As mixing continues into later times, adjacent vortices begin to interact, causing an increase in the flow complexity within the mixing layer.

For ease of comparison between the different Mach number experiments, a subset of representative images from the complete time series in Figures 4.2, 4.3, and 4.4 is shown in Figure 4.9. Images were chosen to highlight the development of the instability throughout time, with images along a row showing the state of the mixing layer at a similar distance from the IC location for each Mach number. As will be discussed below, scaling the time axis with the average convection velocity of the mixing layer to give the distance traveled ($x$) appears to be an effective way to scale many of the measured quantities in this study. By comparing images along a row, Figure 4.9 helps to show the fidelity of this scaling in a qualitative sense.

It can be seen that at early times, up to $x \approx 6$ cm, the evolution for each Mach number is qualitatively very similar in terms of the shape of the structures as the main vortex pairs form. The main difference at these times is that the higher the Mach number the smaller the overall width at a given stage of vortex development. This can be attributed to the higher degree of compression with higher Mach number, and therefore, the smaller the initial width when the instability first begins to grow. Another difference is that the bridges become increasingly flatter with higher Mach

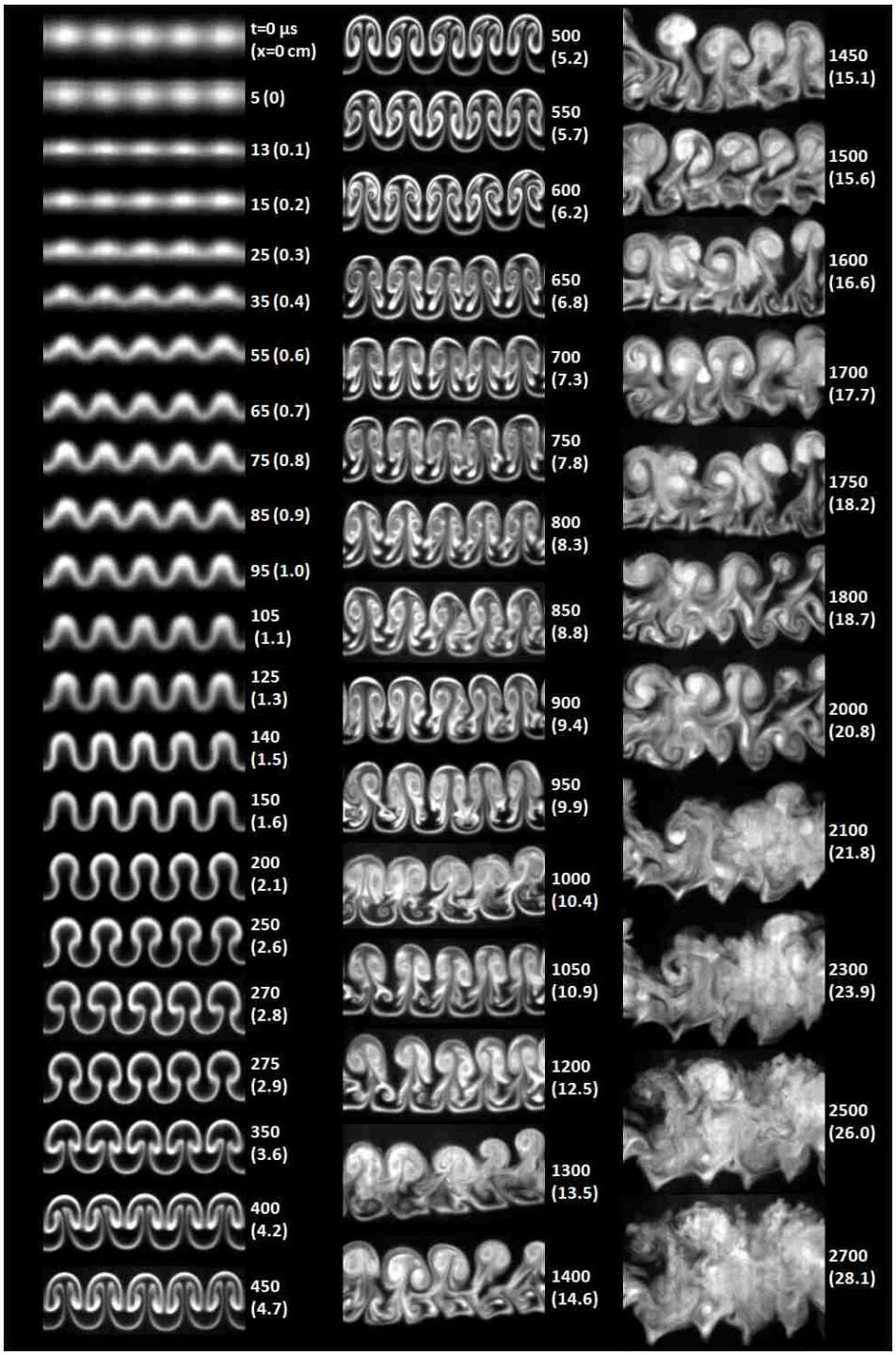


Figure 4.2: Full time evolution of $SF_6$ volume fraction maps for Mach 1.21 experiments. Each image is labeled with time $t$ and distance traveled ($x$).

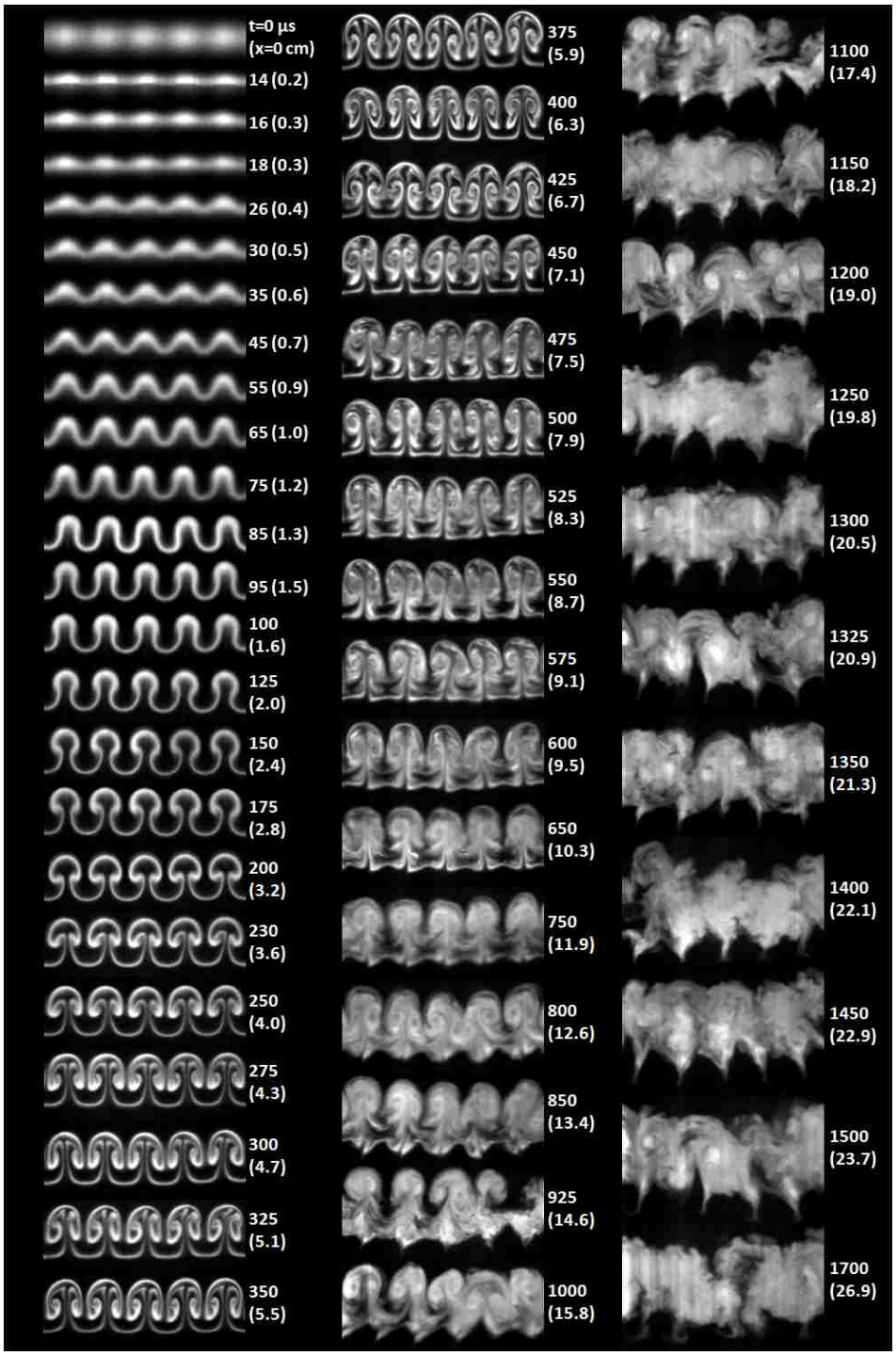


Figure 4.3: Full time evolution of $SF_6$ volume fraction maps for Mach 1.36 experiments. Each image is labeled with time $t$ and distance traveled ($x$).

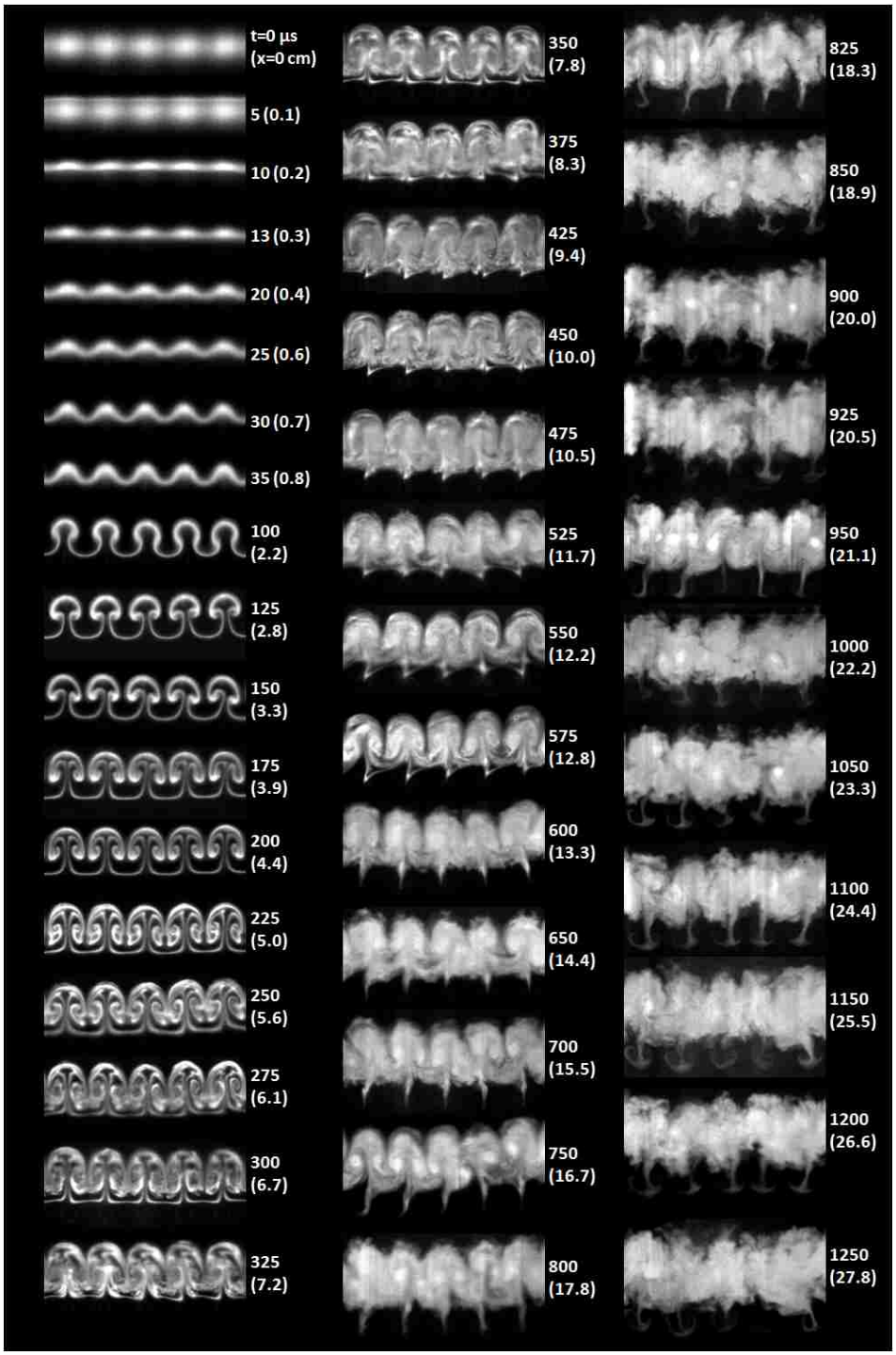


Figure 4.4: Full time evolution of $SF_6$ volume fraction maps for Mach 1.50 experiments. Each image is labeled with time $t$ and distance traveled ($x$).

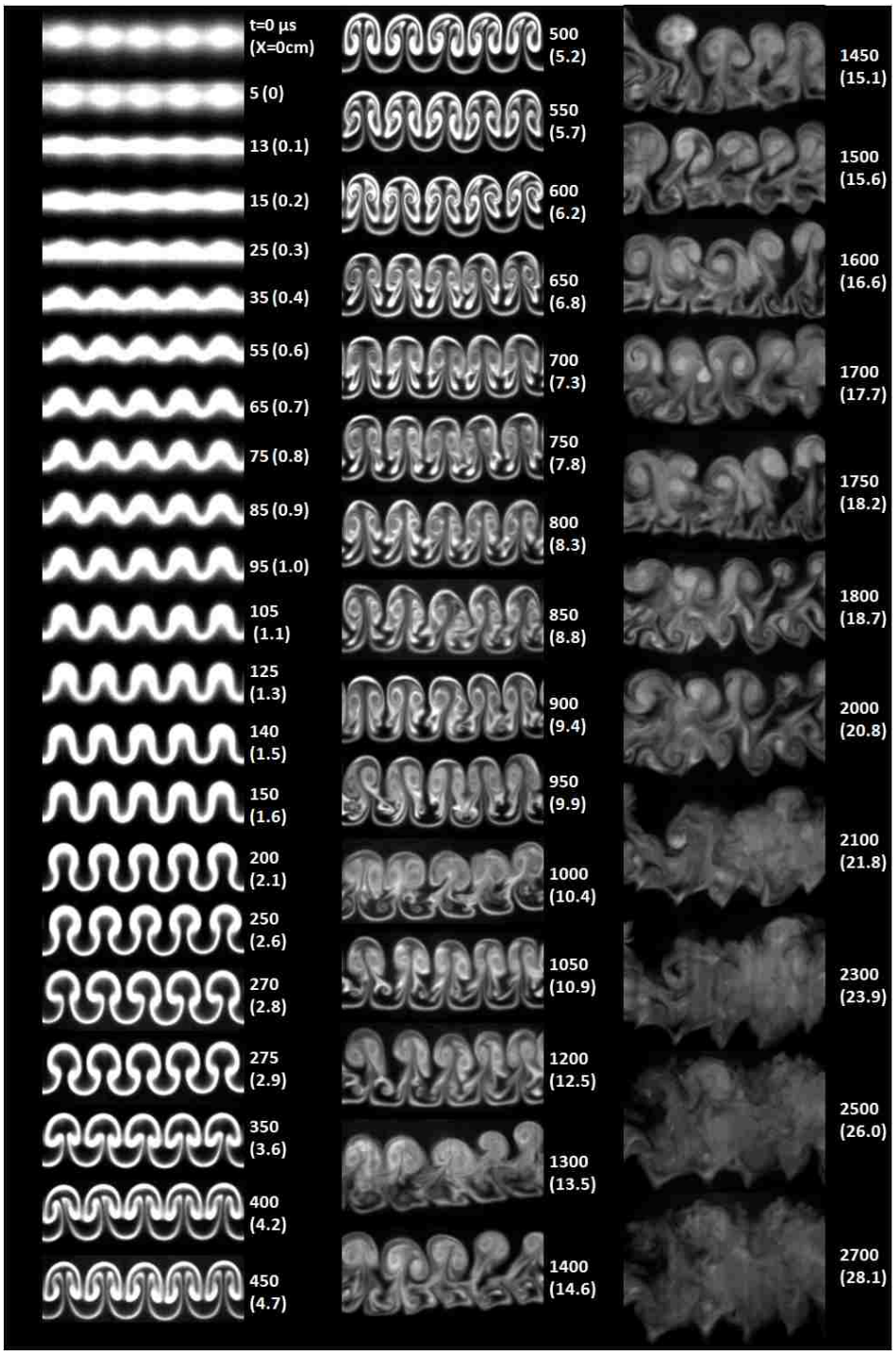


Figure 4.5: Full time evolution of $SF_6$ volume fraction maps for Mach 1.21 experiments. Each image is labeled with time $t$ and distance traveled ($x$). Contrast for all images is set at 1% to 30% $SF_6$ by volume fraction.

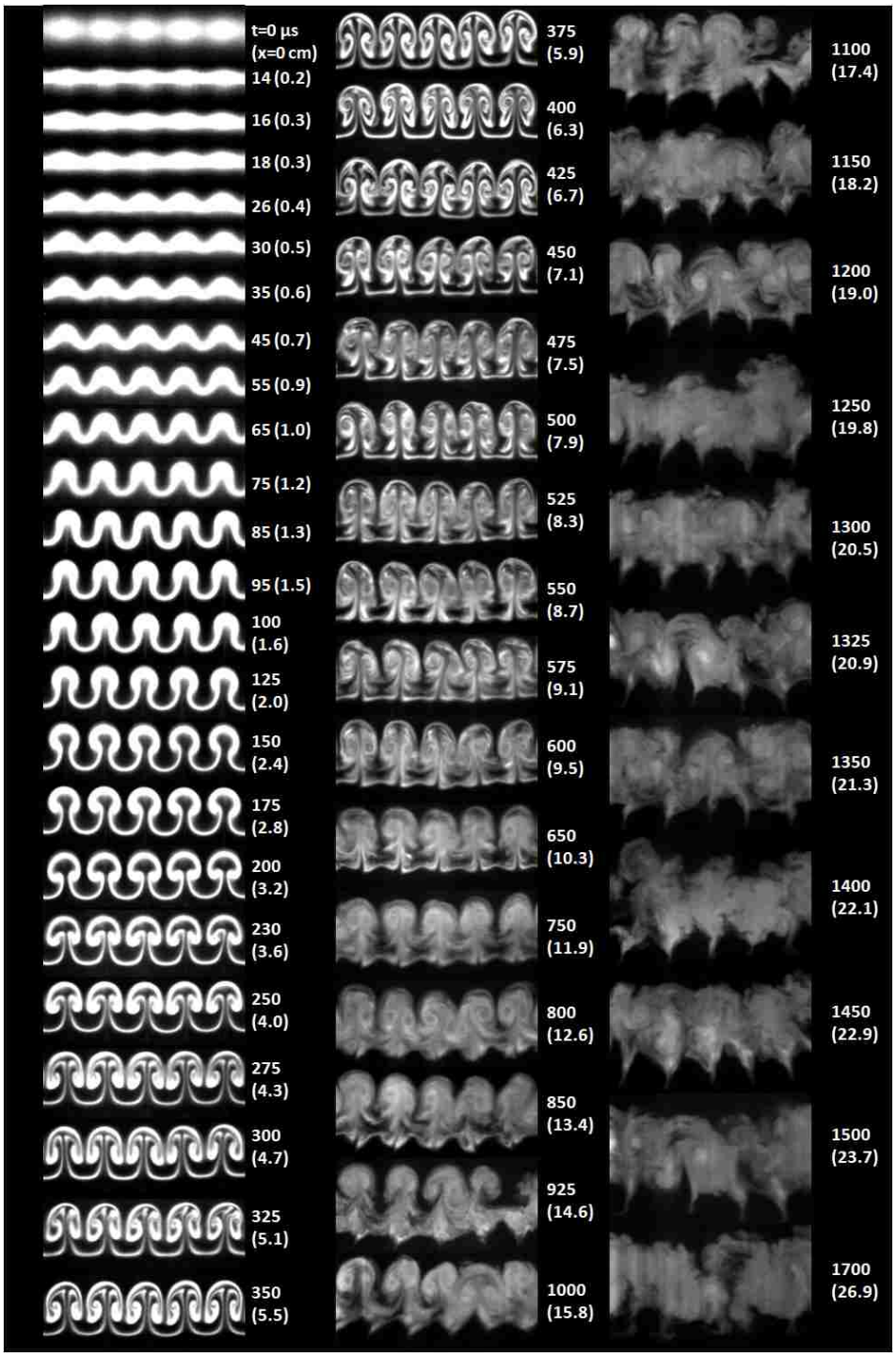


Figure 4.6: Full time evolution of $SF_6$ volume fraction maps for Mach 1.36 experiments. Each image is labeled with time $t$ and distance traveled ($x$). Contrast for all images is set at 1% to 30% $SF_6$ by volume fraction.

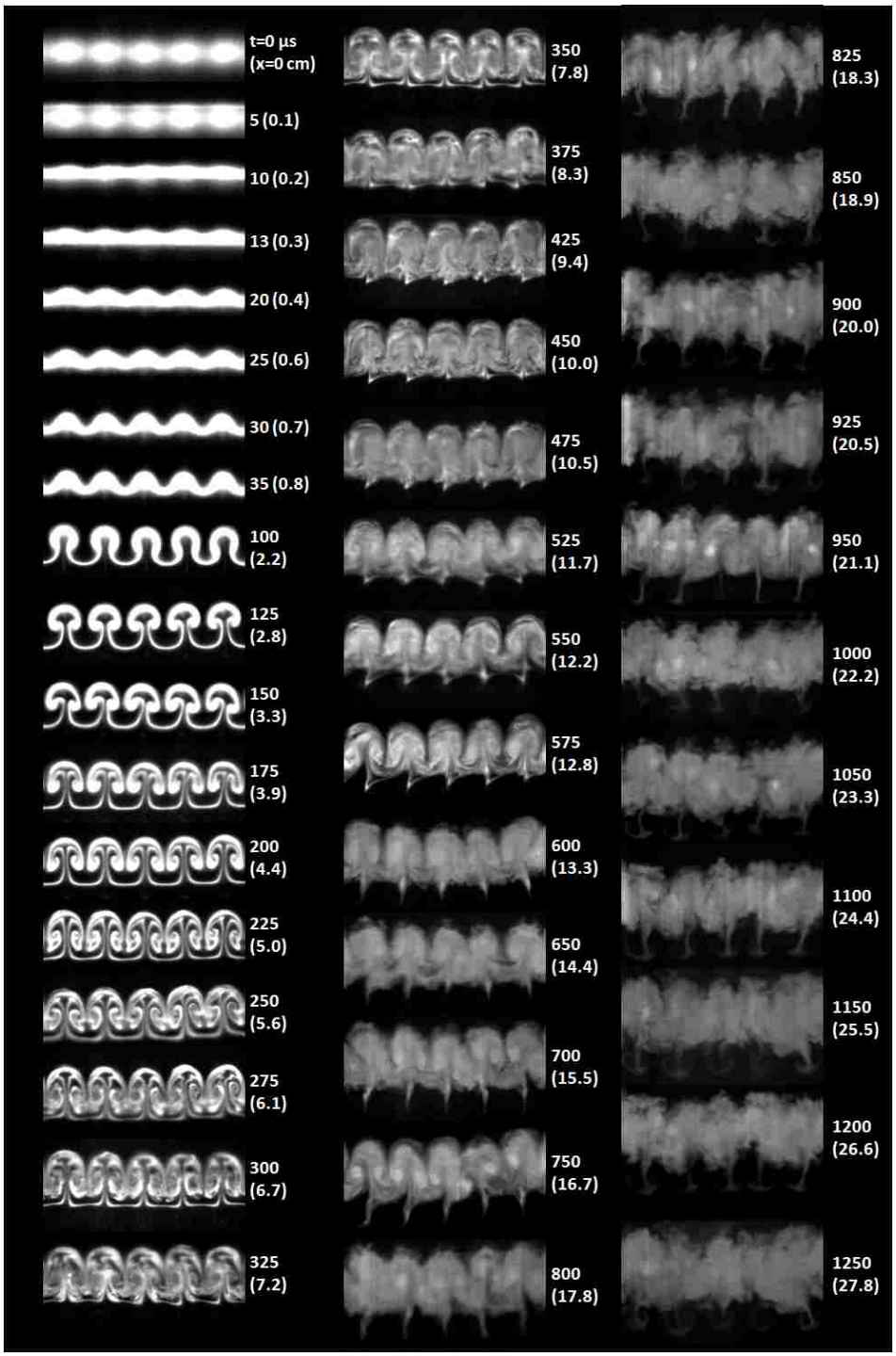


Figure 4.7: Full time evolution of $SF_6$ volume fraction maps for Mach 1.50 experiments. Each image is labeled with time $t$ and distance traveled ($x$). Contrast for all images is set at 1% to 30% $SF_6$ by volume fraction.

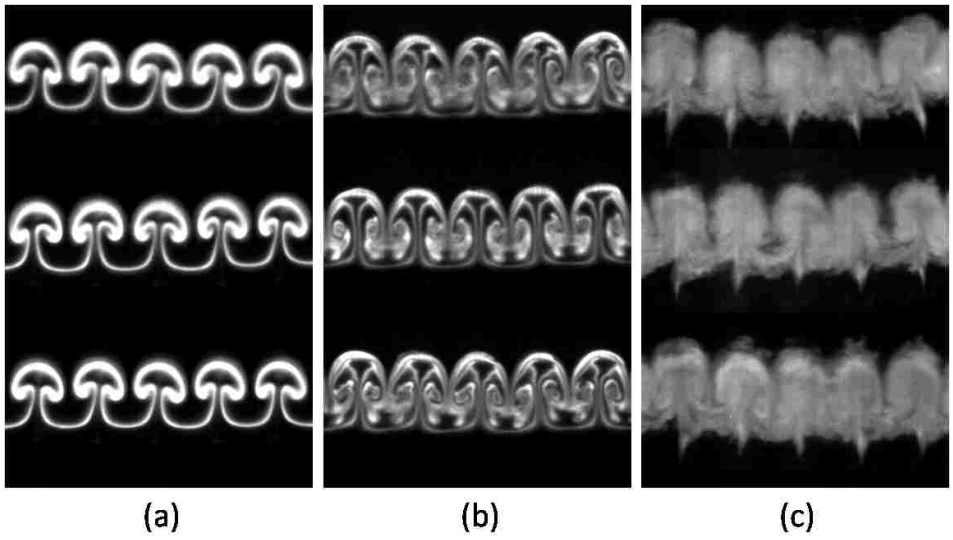


Figure 4.8: Illustration of repeatability for the Mach 1.50 experiments: PLIF images from separate runs of the experiment at (a) 150 μs, (b) 275 μs, and (c) 600 μs after shock impact.

number (e.g. see $x \approx 4.5$ cm). Flattening of flow features with increasing Mach number has been observed in past curtain experiments [47, 50], and single interface experiments [49], and may be attributable to the closer proximity of the shock wave to the moving interface at higher Mach numbers.

As time progresses to intermediate times, from 6 cm to 13 cm, the structures begin to grow differently. From a qualitative perspective, it appears that the higher the Mach number, the stronger the main vortices, and the greater the amount of $SF_6$ that is entrained by them. In Mach 1.21 experiments, the main vortices are not strong enough to continue entraining all the $SF_6$ and tend to lag behind the center of the mixing layer. Alternatively the main vortices in the Mach 1.50 experiments dominate most of the mixing layer and remain located near its center.

As the structures continue to roll up, this leads to differences in the structure shape. By $x \approx 12$ cm, the main vortices in Mach 1.21 experiments have begun to pinch off the rest of the mixing layer, giving rise to a more elongated mushroom

stem. Contrastingly, pinching occurs at a more downstream location in Mach 1.50 experiments where the main vortices have pulled the bridge material toward the spanwise center of each counter-rotating vortex pair, causing it to eject out ahead of the structure. This flow feature is labeled "vortex induced ejection" in Figure 4.1. Mach 1.36 experiments exhibit both pinching mechanisms, with main vortex pairs lagging behind the streamwise center (leading to elongation of the mushroom stems), but still strong enough to induce the bridge material toward the spanwise center of each mushroom, albeit slower in scaled time (distance traveled) compared to Mach 1.50 experiments. In the Mach 1.21 experiments, the bridge material remains bridge material throughout this intermediate time. It can also be seen at intermediate times that as Mach number is increased, small scale mixing is achieved sooner relative to the stage of large scale development. This is evident when comparing Mach 1.21 and Mach 1.50 experiments, for example, at $x \sim 9.5$ cm.

At late times, $x > 13$ cm, the differences observed at intermediate times become magnified. It is around $x \sim 13$ cm that a secondary jump in the growth rates are observed for each Mach number. For Mach 1.21, it is the continued elongation of the mushroom stems, while for Mach 1.50 it is the rapid growth of the vortex induced ejections. For Mach 1.36, both mechanisms appear to contribute. As time progresses, the ejecta itself rolls up into an opposite facing mushroom, presumably due to viscous forces. For Mach 1.50, this roll up begins at $x \sim 19$ cm, but for Mach 1.36, roll up of the ejecta is not observed until the latest time ($x \sim 27$ cm). For Mach 1.21, it is not until the latest times (after $x \sim 19$ cm) that what was formerly bridge material, begins to protrude out from the mixing layer, leading to a jagged interface on the downstream side, and a continued growth increase. The mechanism for the Mach 1.21 bridge material protrusions appears to first involve the rolling up of that material itself, as opposed to $M = 1.36$ and 1.50 experiments where the material ejects straighter out downstream.

There is also a higher degree of uniformity for small scale mixing across the mixing layer with higher Mach number. For Mach 1.50, the stronger vortices stir the entire width of the mixing layer, except for the ejected material, leading to an earlier transition to small scale mixing throughout the layer. For example, compare the uniformity of small scale mixing at $x \sim 19$ cm. Another effect of the stronger vortices is that they help to preserve spanwise symmetry through conservation of angular momentum as the mixing layer develops in time. For Mach 1.21 experiments, small differences in vortex strength between two counter-rotating vortices cause the mushrooms to tilt to one side or another, and sometimes to grow into an adjacent mushroom and effect its evolution. In terms of the large scale mixing, symmetry appears to break down within the intermediate time scale at ∼10 cm for Mach 1.21, and at late times at ∼16 cm for Mach 1.35. For Mach 1.50, the symmetry appears to be relatively maintained throughout all time that was investigated. For this reason, higher Mach number experiments were more repeatable at later times. However, the presence of small scale mixing in Mach 1.50 experiments makes it difficult to tell from the density maps what is happening with the main vortex pairs after 18 cm.

Another feature that is dependent upon Mach number is the amount of material that spikes out ahead of the mixing layer due to shock focusing on the downstream edge. See the feature labeled "spike"in Figure 4.1. This feature is generated before the formation of the main vortices, and if it consists of enough material, it can itself roll up into an opposite facing mushroom as it evolves in time. Because the spike is made up of a very small amount of material with an intensity that is just above background, further discussion of the this flow feature is reserved for Appendix C.

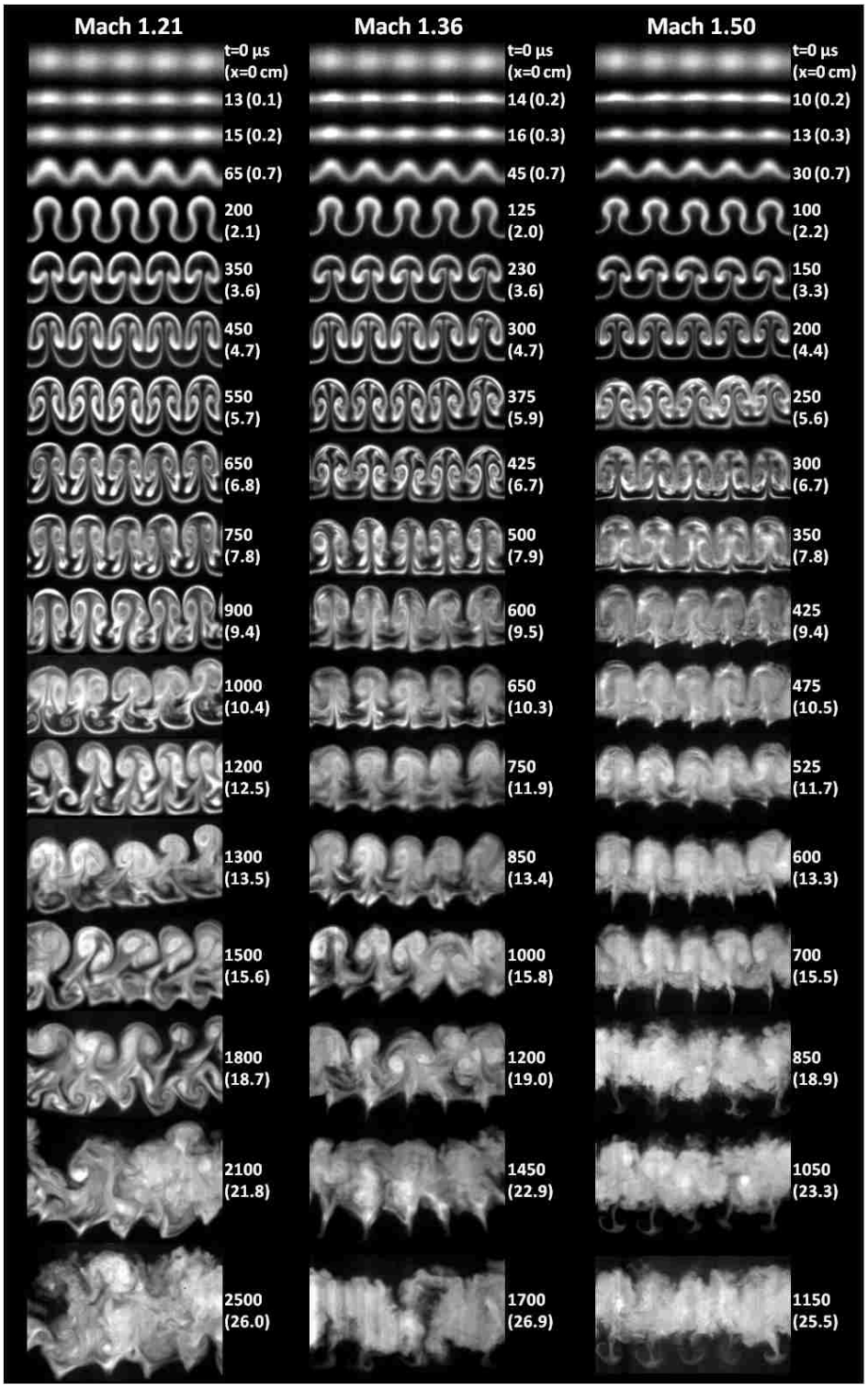


Figure 4.9: A selection of $SF_6$ volume fraction maps from each Mach number experiment. Images in each row were acquired at roughly the same location as indicated in the figure, with time $t$ and distance traveled ($x$).

## 4.2 Mixing Layer Width

The total width of the mixing layer is a common quantitative metric used to compare the large scale mixing between different experiments, models, and simulations. The present configuration may be viewed as two closely-spaced single interfaces that interact by interface coupling and feedthrough [48]. Note that the growth of perturbations is expected to be nonlinear not only because of interfacial interaction, but also because the amplitude, $a$, on both interfaces appears to quickly reach the same scale as the wavelength of the perturbations (i.e. $ka \approx 1$, where $k$ is the wavenumber). Two of the motivations for the current study are to test the ability of a simple point vortex model to capture the trends in integral width as a function of time, and to determine whether mixing layer width of experiments at different Mach numbers could be effectively scaled. This section addresses the former. Integral width, defined as the distance spanning the farthest upstream and downstream location at which $SF_6$ is present within an individual image, represents the characteristic large scale of the flow and provides a first-order measure of mixing.

While many models exist for perturbation amplitude growth in single interface studies, their applicability is limited in the current dual-interface study. One model for the mixing width is applicable to the current study [40], however, and has shown good agreement with other varicose curtain experiments [41, 44]. The model is based upon an infinite row of counter-rotating point vortices, each with the same magnitude of circulation. The input parameters for the model include the circulation, $\Gamma$, the initial width just after shock compression, $\delta_0'$ (where $'$ denotes post-shock conditions), and a single wave number, $\kappa = 2\pi/\lambda$, where $\lambda$ is the wavelength of the perturbations. This model leads to a mixing width over time of:

$$\delta(t) = \frac{2}{\kappa} sinh^{-1}\left[\kappa^2 \Gamma (t - t_0) + sinh\left(\frac{\kappa \delta_0'}{2}\right)\right] \tag{4.1}$$

where $t_0$ is the time of the virtual origin of the width growth curve. The virtual origin

was not included in the original model, but was added to account for the time taken for both the compression stage, and for phase inversion to occur on the downstream interface between $SF_6$ and air (where the shock wave is directed from heavy to light fluid) [41, 44]. The parameter values used for fitting can be found in Table 4.1.

The integral width of the curtain was measured over one perturbation wavelength at the same spanwise location for each time, as shown in Figure 4.10. The edge of the layer is taken to be the farthest streamwise location at which the $SF_6$ concentration is at least 4%. If a spike or late time remnants of a spike (diffuse opposite facing mushroom) were evident in an image, they were not included in the width measurement, as such small scale features comprise very little material, do not appear to affect the vortex dynamics, and are not accounted for in the mixing width model.

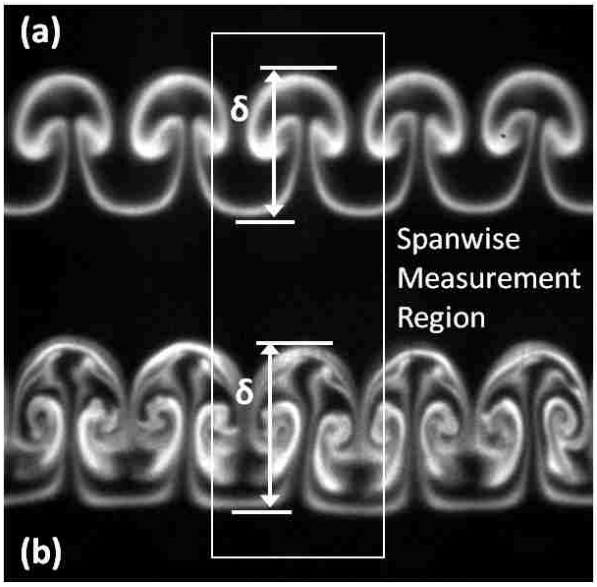


Figure 4.10: Definition of mixing layer width, $\delta$, using Mach 1.35 experiments at (a) 230 $\mu$s, and (b) 425 $\mu$s. The width is the distance between the farthest upstream and downstream extents at which at least 4% $SF_6$ volume fraction is present.

In Figure 4.11 the integral width ($\delta$) of the mixing layer is plotted against time for all time series images. As expected, the growth rate is higher as the Mach number

is increased. At late times, the flow features discussed above cause a secondary jump in the growth rate for each Mach number. For Mach 1.21, it is mainly due to the lag of the main vortices, whereas for Mach 1.50 it is due to the ejections ahead of the downstream interface that are formed by the interaction between the relatively stronger main vortex pairs. For Mach 1.36, both mechanisms contribute.

Also in Figure 4.11 are the best fit curves to each data set derived from the Jacobs *et al.* mixing width model described above. The parameters that were varied to achieve the best fits were the virtual origin, $t_0$, and the circulation, $\Gamma$. Several runs in each Mach number experiment were carried out to image the flow just after shock passage, therefore, the initial width, $\delta_0'$, was measured experimentally and fixed. For $M$ = 1.21, 1.36, and 1.50, $\delta_0'$= 2.626 mm, 2.323 mm, and 2.172 mm, respectively. The wave number, $\kappa$, was also measured and fixed at 1.745 mm$^{-1}$. The model curves, with $\Gamma_{Fit}$ = 0.045 mm$^2$/μs, 0.055 mm$^2$/μs, and 0.062 mm$^2$/μs for Mach 1.21, 1.36, and 1.50, respectively, agree fairly well with the experimental data until approximately 1000 μs, 800 μs, and 600 μs, respectively. These times correspond roughly to when secondary growth mechanisms begin to be important in the mixing layer width measurement.

This later time disagreement is likely due to a combination of physical departures from the model including the blob-like (as opposed to point) nature of the vortices, the three-dimensionality of the flow, and viscous effects. Also, in the experiment, the vortex cores are not perfectly spaced. The distance between the cores of a counter rotating vortex pair (mushroom) is slightly larger than the distance between a vortex core from one mushroom and the nearest vortex core of an immediately adjacent mushroom. In the model, the vortices are evenly spaced. It should also be noted that the circulation was measured in the experiments, as discussed below, and was found to be significantly higher (about 2 times) than those for the best fits. While the model, in its current form, does not appear to be useful for predicting

growth rate, it does appear to capture the shape of the growth up to intermediate times before secondary mechanisms become important in the width measurement. This suggests that the physics in the model is appropriate for those times, in that the flow is vortex-dominated. And this also presents the possibility that the model could be modified to be more predictive by scaling the circulation term and including a dependence on Mach number or velocity jump. Yet, more experimental data would be required to determine those modifications accurately. At later times, the model under-predicts the width and is unsuitable for comparison to the experiment because of the differences in the flow dynamics.

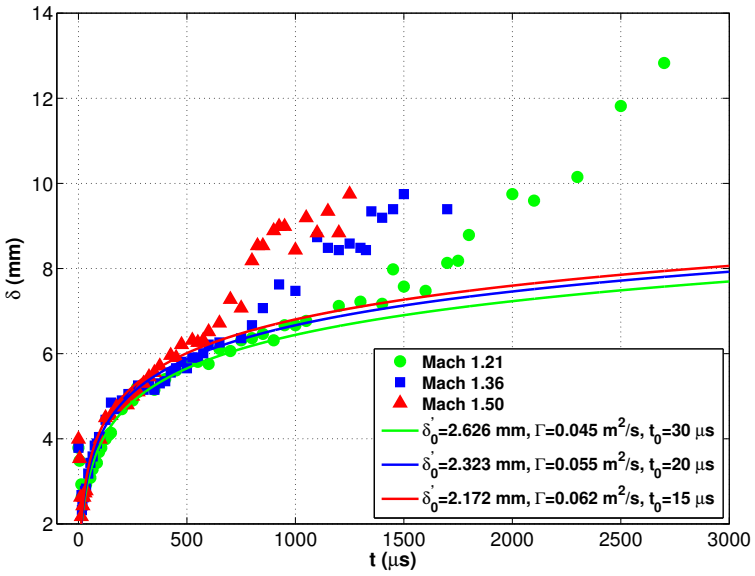


Figure 4.11: Integral width *vs.* time.

## 4.3 Scaling the Mixing Layer Width

Previous R-M studies have shown that mixing layer width can be effectively scaled amongst experiments at different Mach number, both for single interface and double interface gas curtain experiments. In this section, possible scaling methods are discussed, and several figures are provided to demonstrate the fidelity of each.

Most experimental efforts to scale growth rate have been motivated by nondimensionalizing Richtmyer's linear formulation so that

$$\kappa a - \kappa a_0 = \kappa^2 a_0 A \Delta v t \tag{4.2}$$

The nondimensional time is then taken as

$$t^* = \kappa^2 A \Delta v a_0 t \tag{4.3}$$

and the nondimensional perturbation amplitude is then $\kappa a - \kappa a_0$, where it has sometimes been found that the fidelity of the scaling can be improved if the post-shock or the average of pre-shock and post-shock values of $a_0$, or $A$ are used. In studies where the linear growth regime can be measured experimentally, the term $\kappa a_0 A \Delta v$ can be replaced by $\dot{a}_0$ [12, 27], the measured initial growth rate, assuming that linear stability is a reasonable estimate for the growth, so that

$$t^{**} = \kappa \dot{a}_0 t \tag{4.4}$$

This scaling has proven to be more effective still, presumably because it accounts for the finite diffusion thickness present in experiments, but not accounted for in Richtmyer's impulsive model, as well as any other effects due to the passing shock wave. However, this scaling requires that experiments must first be performed for

each initial condition and each Mach number, and therefore is not predictive. It should be noted that when the initial growth rate cannot be experimentally measured, a growth rate reduction factor, $\psi$, can be added to the impulsive model, and therefore to $t^*$, to improve the scaling by accounting for the reduction in growth rate when the interfacial density profile has some slope, as opposed to being discontinuous [12, 49].

Measured in the current experiment, is the growth of integral width, $\delta$, which is dependent upon the growth of the perturbations, $da/dt$ on both sides of the fluid layer. In the limit of a thick curtain with no interaction between the two interfaces, one would expect $d\delta/dt = 2da/dt$, based on Richtmyer's formula if the initial perturbations are sufficiently small in amplitude. With this motivation, previous gas curtain experiments introduced the nondimensional time parameter [47]

$$\tau = 2\kappa A \Delta v t \tag{4.5}$$

It was found that simply using the pre-shock value for $A$ was the more effective way to collapse the growth rate with scaled time, $\tau$. It is worth noting that $\tau$ does not include a dependence on $a_0$, which is difficult to quantify due to the diffusion thickness in curtain experiments, and therefore was excluded. Moreover, it is not appropriate to substitute $\delta_0$ for $a_0$ because the scaling is then no longer tied to the linear stability analysis.

Because $t^{**}$ lacks predictive capability and simply forces a curve fit at early times, and because $\tau$ is not universal for a variety of initial conditions because it does not include a dependence on $a_0$, both methods of scaling the time axis are lacking. In the present study, the only parameter that changes with Mach number and affects the growth according to the linear stability formulation is $\Delta v$, if pre-shock values are used. Therefore it is more intuitive to simply scale the time axis with the convection velocity of the mixing layer and essentially plot the width as a function of distance

traveled, $x$, as shown in Figure 4.12. This will be the preferred scaled time for the rest of this dissertation unless otherwise noted. But for comparison to the previous work available in the literature, plots with $t^{**}$ (with $\dot{\delta}_0$ replacing $\dot{a}_0$ in Equation 4.4) and $\tau$ are also presented below. Note that the trends in the plots with $\tau$ are exactly the same as with $x$ because pre-shock values for $A$ were used to calculate $\tau$.

Plotting width against distance traveled (by scaling the time axis with the average convection velocity, $\langle\bar{u}\rangle$), as in Figure 4.12, achieves an effective collapse of the data in the sense that the growth rate with distance traveled is equivalent for each Mach number case until the latest times where the Mach 1.21 structures grow faster. This tertiary growth rate increase for Mach 1.21 experiments occurs after 23.5 cm, and appears due to the interaction of bridge material that leads to the jaggedness observed on the downstream interface. The average convection velocity for the structures was measured by ensemble averaging over the mean streamwise velocity for each mixing layer within a given Mach number experiment, so that $\langle\bar{u}\rangle = 104$, 158, and 222 m/s for $M = 1.21$, 1.36, and 1.50, respectively. Here over bars denote averaging within a given realization, and angle brackets denote ensemble averaging over a set of realizations. At earlier positions (up to approximately 13 cm), before secondary growth features add another level of complexity to the mixing layer evolution, there exists an offset in width between each data set, as the higher the Mach number the greater the compression, and the smaller the initial width of the mixing layer after shock passage. The width axis can itself be normalized by the post shock width for each Mach number, $\delta_0'$, to attempt to account for this offset, as in Figure 4.13. However, this normalization appears to overcompensate for the offset. This is consistent with previous gas curtain work [47].

Normalized width ($\delta/\delta_0'$) is plotted against $t^{**}$ in Figure 4.14. Using the measured early time growth rate (calculated from $t^{**} \leq 4$) to scale the time axis forces a collapse of the data at these early times, however a fairly good collapse of the data

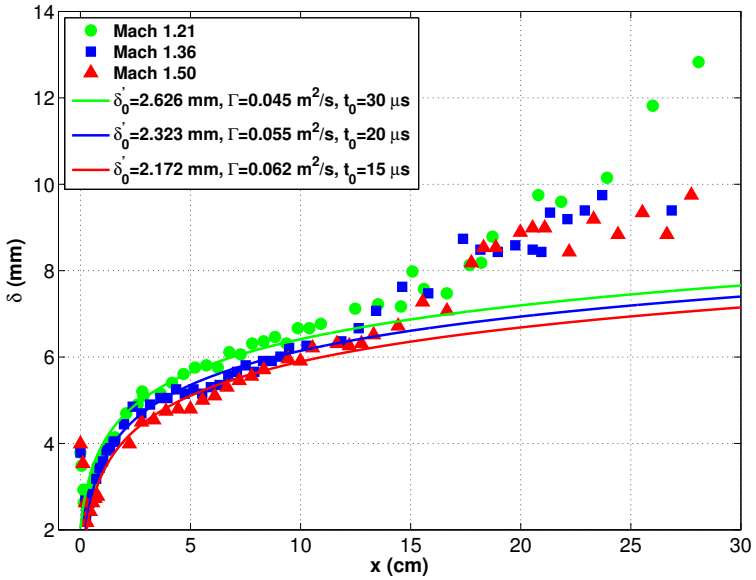


Figure 4.12: Integral width *vs.* distance traveled shows the same growth rate, but with a vertical offset separating the experiments.

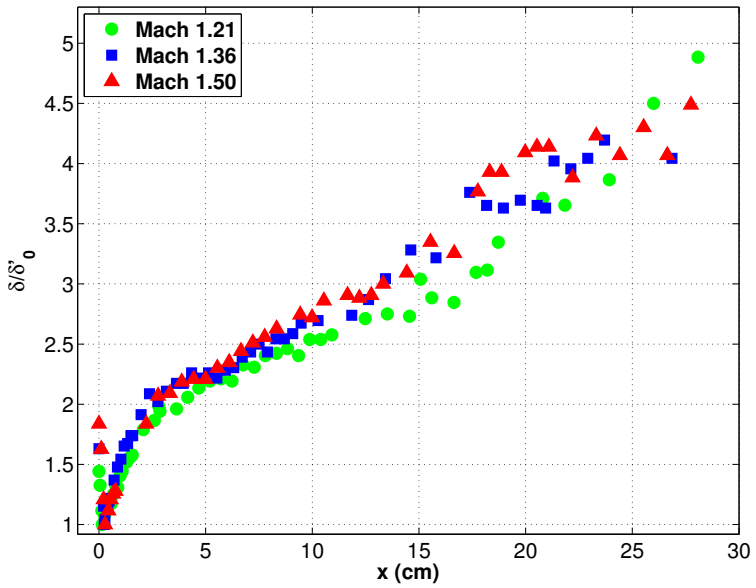


Figure 4.13: Normalized integral width *vs.* distance traveled. Normalizing the width using $\delta_0'$ overcompensates for the offset.

is maintained well past $t^{**} = 4$ to $t^{**} \approx 40$ with the Mach 1.21 experiments growing faster thereafter.

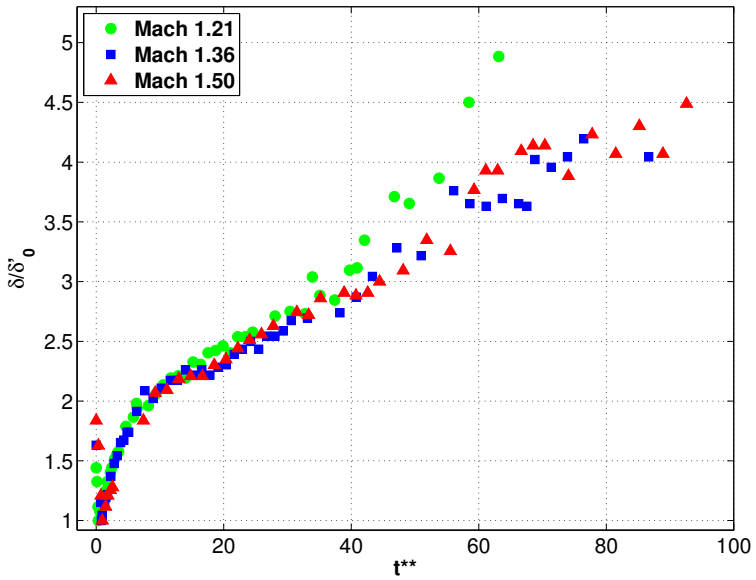


Figure 4.14: Normalized mixing layer width width *vs.* $t^{**}$ collapses the data up to $t^{**} = 40$.

It was found that the most effective way to collapse the growth rate data for the longest duration of time was to plot $x$ (or equivalently, $\tau$) against a nondimensional width, $\delta^*$, defined as

$$\delta^* = \frac{\delta}{\delta_0'} M^{-0.4} \tag{4.6}$$

Here, the width axis is scaled both by the initial post-shock width, and the Mach number, $M$, of the experiment. The $\delta^*$ scaling was first introduced by the University of New Mexico [55] to collapse single cylinder initial condition numerical experiments with Mach numbers ranging from $M = 1.2$ to $M = 2.5$. Here, as seen in Figure 4.15, this scaling does a remarkable job of collapsing the present gas curtain experiments up to $x \approx 25$ cm ($\tau \approx 475$). While the $\delta^*$ scaling is not based on the available theory

for R-M instability growth, it warrants future study for its potentially predictive capability when paired with the proper time axis scaling, which here is found to be the distance traveled, $x$.

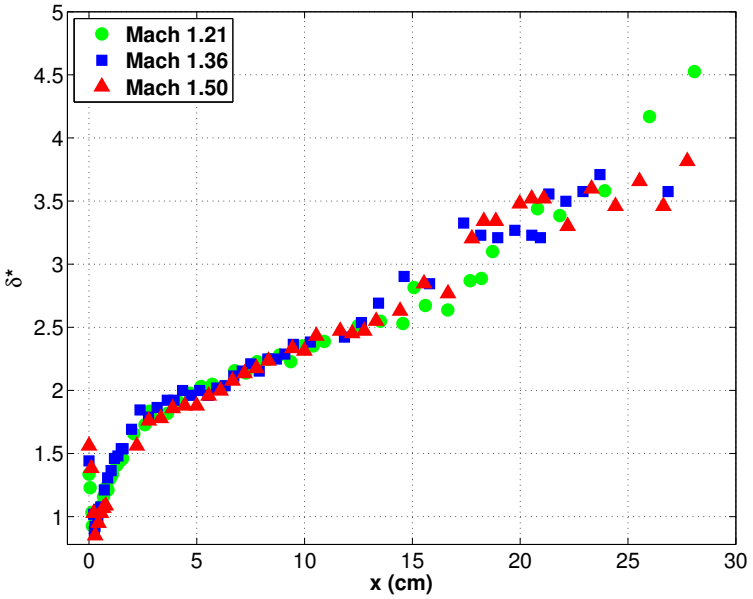


Figure 4.15: Scaled integral width *vs.* distance traveled.

While integral width is a useful metric to compare between different experiments, simulations, and models, and is a simple measurement to make, it is very limited in what it can tell about the mixing and the mechanisms that drive it, especially at smaller scales in the flow. Previous experiments have shown that quantitative measurements of smaller scale features, such as the instantaneous mixing rate, do not scale similarly with velocity [47]. This highlights the need for additional metrics to compare between experiments, simulations, and models, and to gain an understanding for the physics involved in the mixing process.

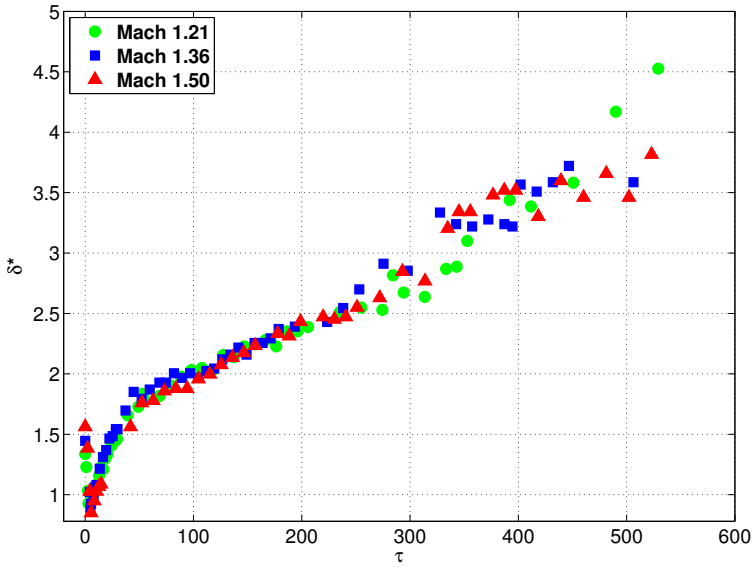


Figure 4.16: Scaled integral width *vs.* $\tau$. Is equivalent in terms of the trends in the data to Figure 4.15.

## 4.4 Simultaneous PIV/PLIF Data

The current work is the first to obtain the time evolution of both the density and the velocity field in a R-M Mach number experiment. Moreover, that they are acquired simultaneously can allow for quantification of density-velocity cross-correlations, which are necessary for calculating terms of the Reynolds stress (turbulent momentum transport), and turbulent mass flux. Figures 4.17, 4.18, and 4.19 show demonstrations of simultaneous PIV/PLIF data evolving over time for each Mach number. It shows the evolution of the quantitative density maps, the raw particle fields used for PIV, and the vorticity and turbulent kinetic energy (TKE) maps that can be derived from the velocity fields. These latter two quantities, which will be discussed more thoroughly in later sections, help to show show which length scales contain energy, where that energy is located spatially, and how that impacts the mixing observed in the density fields. In concert, these maps provide much more quantitative information about the evolution of the R-M instability than previously achievable, and can serve as a reference for subsequent discussion.

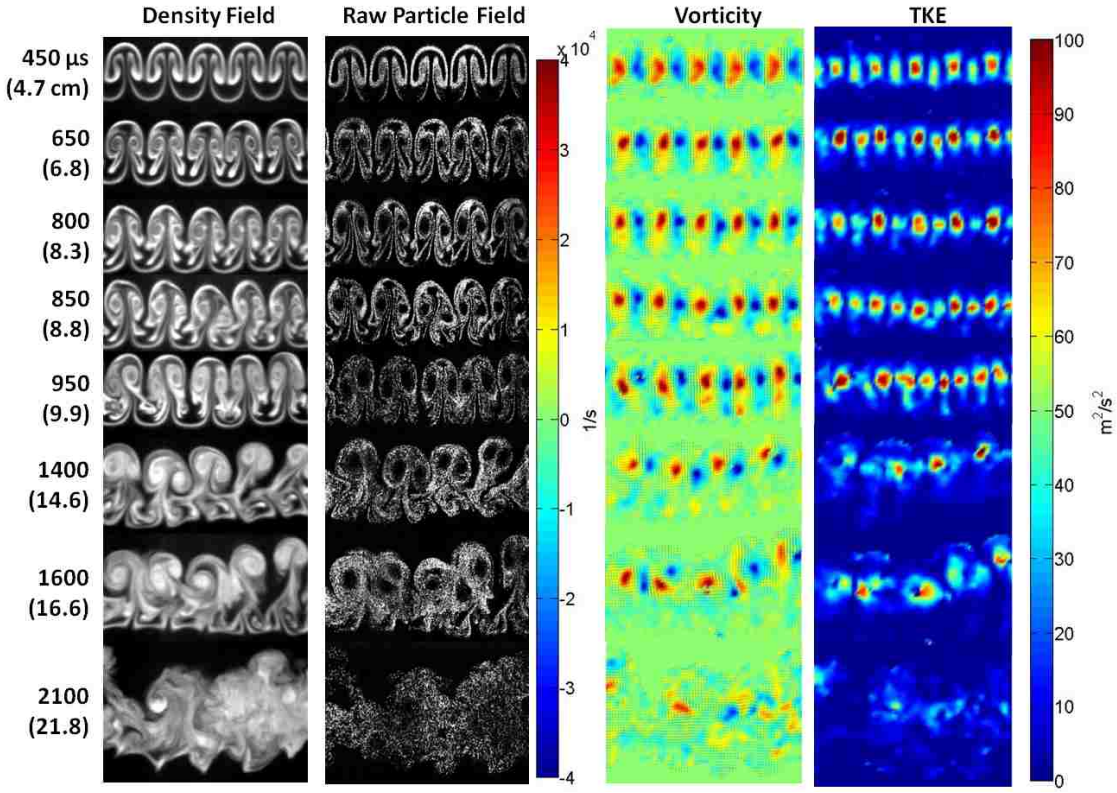


Figure 4.17: Mach 1.21: Demonstration of simultaneous PIV/PLIF.

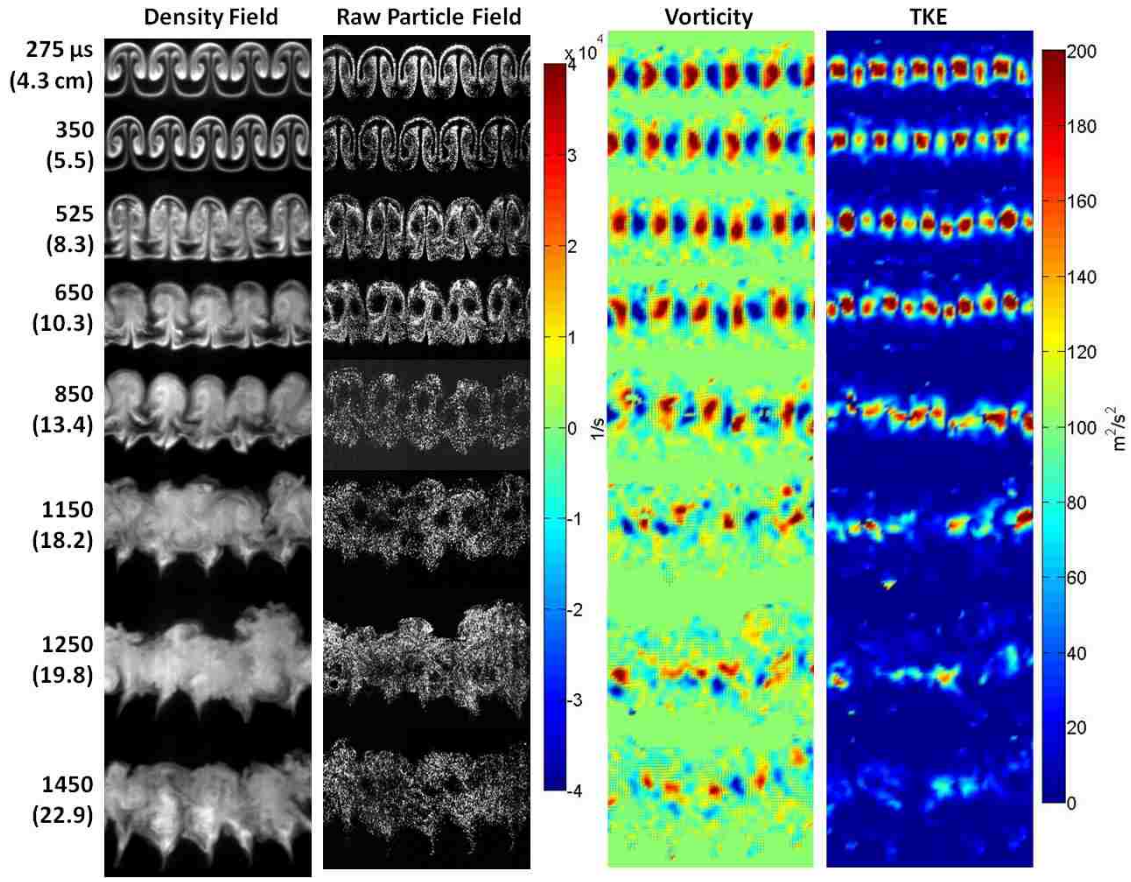


Figure 4.18: Mach 1.36: Demonstration of simultaneous PIV/PLIF.

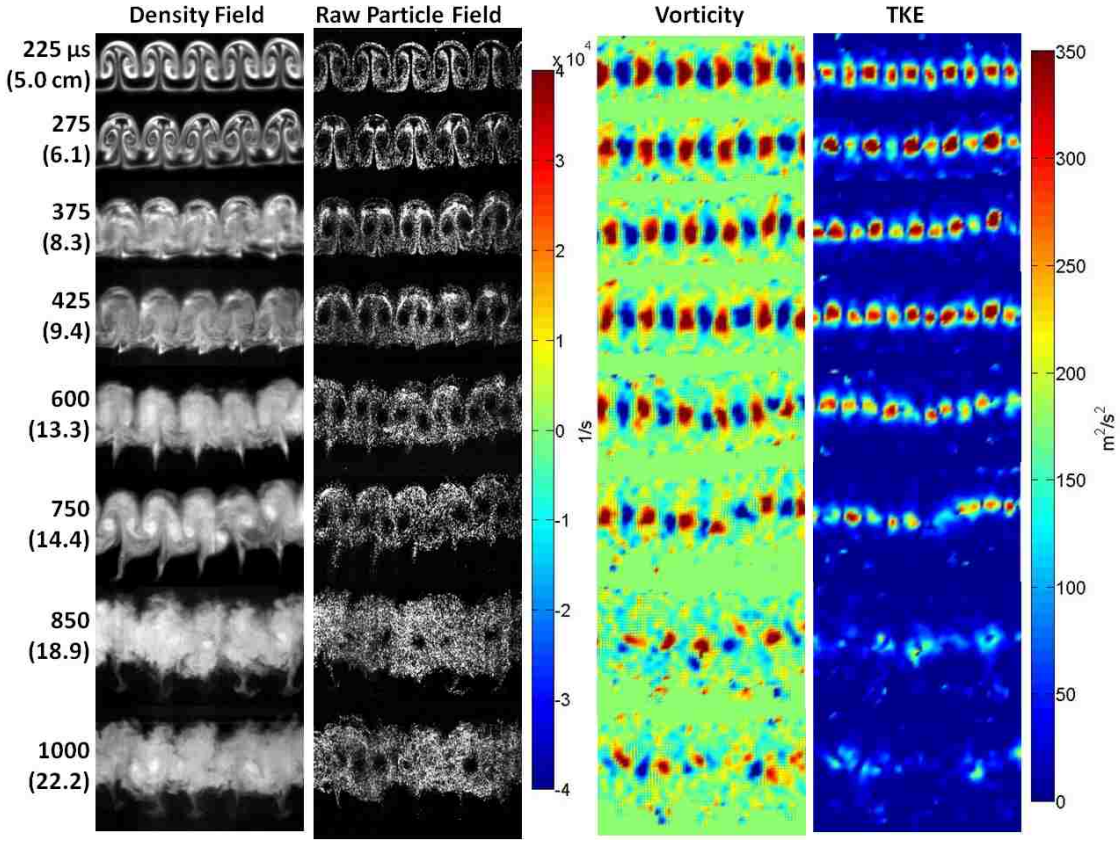


Figure 4.19: Mach 1.50: Demonstration of simultaneous PIV/PLIF.

## 4.5 Vorticity

The time evolution of the 2-D vorticity field (curl of the velocity field, $\vec{\omega_z} = \partial\vec{v}/\partial x - \partial\vec{u}/\partial y$) for each Mach number is shown in Figure 4.20, with color scale held constant for all maps. The vorticity maps that are presented correspond to velocity fields that were acquired simultaneously with PLIF images. The numbers in parentheses represent the streamwise position of the structures in centimeters, with images along a row acquired at roughly the same scaled time, $x$. As expected, values for vorticity are higher in the higher Mach number case, where the main vortices also dominate a greater region of the flow. It is believed that these differences account for the disparity in large scale flow morphology seen in PLIF images at later times, as discussed above. In each case, as time progresses, the array of alternating blobs of positive and negative vorticity begin to lose their symmetry, which then precipitates a transition of the vorticity field to a more disordered state, and a break up of the main vortices into smaller blobs, indicating a transfer of energy to smaller scales. The onset of the disorder, from Figure 4.20, appears to have begun by the second to last row, which is approximately when the secondary growth jump is observed in the integral width plots (as observed in Figure 4.12). In this way, interaction of the main vortices, as they grow in time, appear to cause both a lack of symmetry in the flow field, and further growth in the total mixing width, $\delta$.

The sum of all positive and negative vorticity in each vorticity map was calculated over 5 wavelengths, and is presented in Figure 4.21. As can be seen, the amount of vorticity decreases with time for each Mach number, and at a faster rate for higher Mach numbers. The decrease in vorticity over time could be accounted for by a transfer of motion to smaller, under-resolved length scales, as it is clear in Figure 4.20 that the flow field is trending in that direction. But the decrease could also be accounted for by 3-D effects or viscous forces which appear as sink terms in the equation for vorticity production (Equation 1.4). Most likely, all three factors

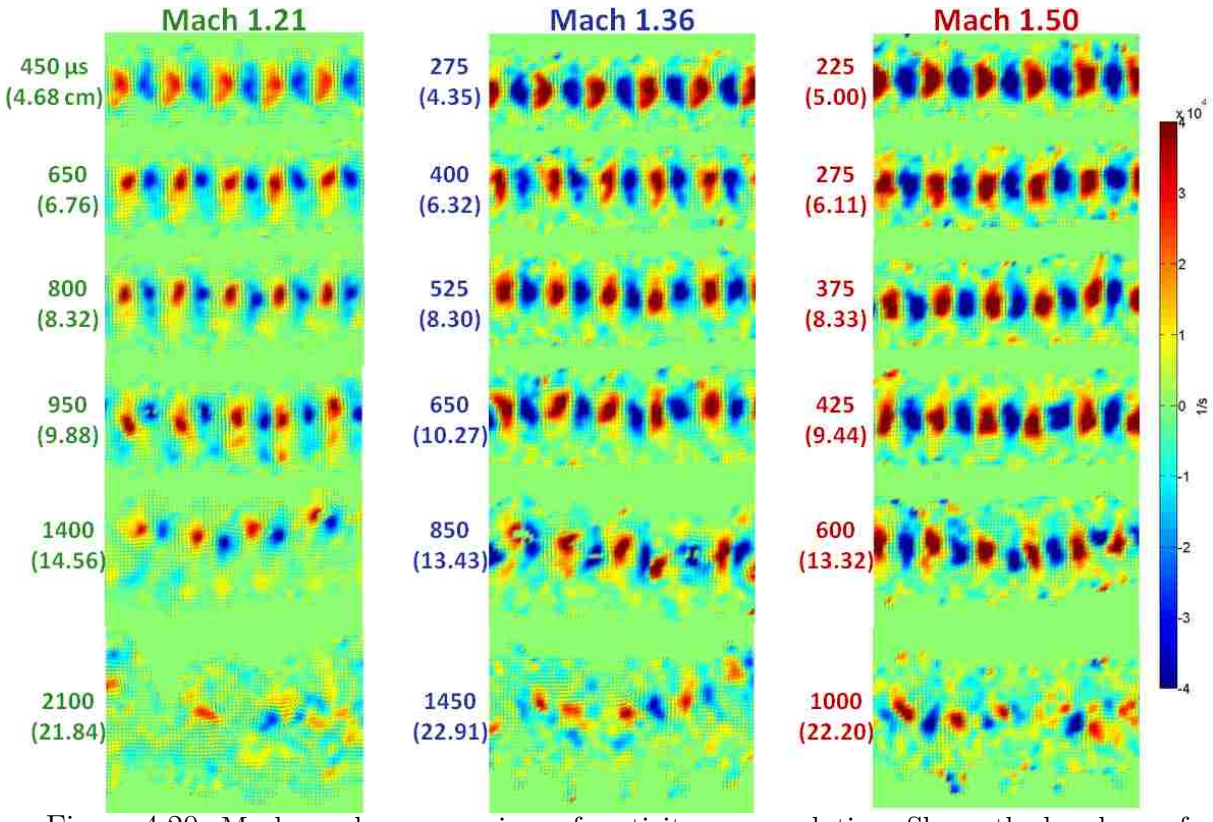


Figure 4.20: Mach number comparison of vorticity map evolution. Shows the break up of the main vortices over time.

contribute, but the degree to which each does is unknown. Figure 4.22 shows the total positive and negative vorticity plotted against distance traveled. Similar to the mixing width data, the rate at which the vorticity changes with distance traveled is roughly the same for all Mach numbers. Note that the absolute values in Figures 4.21, and 4.22 are dependent upon the resolution of the velocity maps, and therefore the PIV processing window size. Since all maps were processed with 24×24 window sizes, the relative values for total vorticity are meaningful. However, it deserves note that there is a measurement bias due to the seeding of only $SF_6$ (and not air) which results in an unquantified error in the total vorticity value, which may not be the same for each Mach number. At later times when the mixing layer is more uniformly mixed, this error is expected to be insignificant.

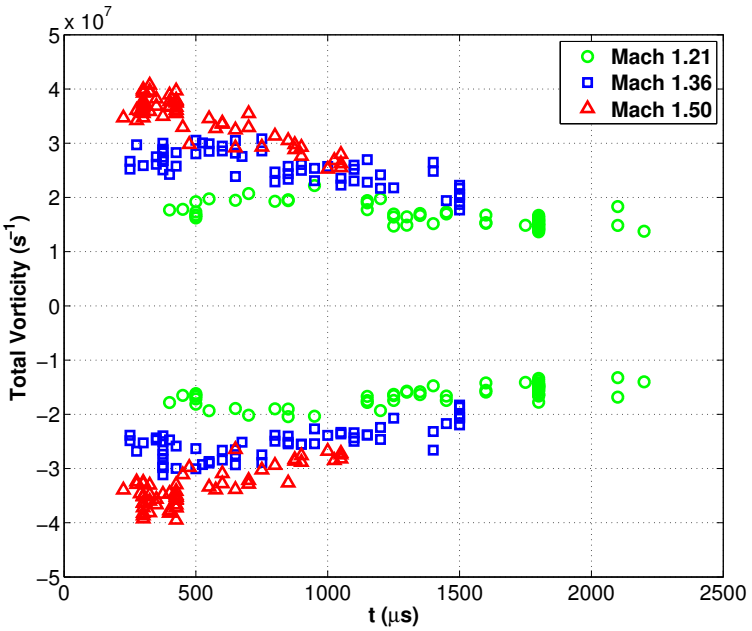


Figure 4.21: Sum of the positive and negative vorticity in the mixing layer is initially greater with increasing $M$, and decreases over time for each case. The rate of the decay is higher for higher $M$.

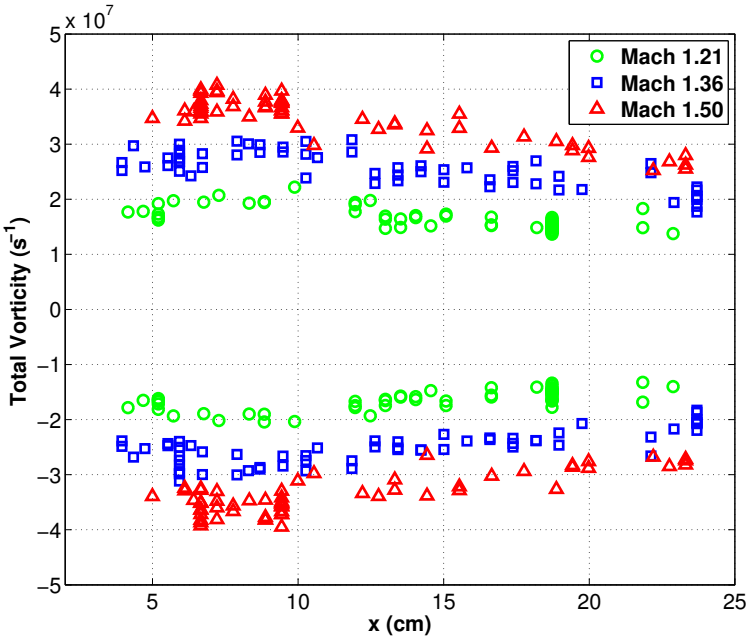


Figure 4.22: Sum of the positive and negative vorticity in the mixing layer is greater with increasing M for all scaled times, and decreases at approximately the same rate with scaled time for each case.

## 4.6 Circulation

Circulation, $\Gamma$, was calculated from the velocity field via a line integral of the tangential velocity component, $\Gamma = \oint \vec{u} \cdot \vec{dl}$. The calculation was made using a rectangular path enclosing a selected positive valued vortex. For each velocity field, up to 5 vortices were chosen, and the circulation of each was used to get an average value for circulation in a given field. At later times, when the velocity field becomes less ordered, only the strongest, most defined regions of vorticity were selected. This resulted in unreliable measurements after roughly $x = 18$ cm. Figure 4.23 shows an example of the rectangular regions used to calculate average circulation for a single velocity/vorticity map. Figure 4.24 shows the average circulation of the main vortices over time for each Mach number. Similar to vorticity, the average circulation decreases with time for all cases, and with a faster rate for higher Mach numbers. The decrease in circulation over time provides further evidence that energy is being transferred out of the main vortex pairs and into smaller scales. Also similar to vorticity and mixing width data, when plotted against position the rate at which the circulation changes with distance traveled is similar in all cases, as seen in Figure 4.25. Between $x = 6$ and 10 cm, when the main vortex cores have formed, but before they begin breaking down to smaller scales, the average values for $\Gamma$ are approximately 0.07, 0.09, and 0.13 mm$^2$/$\mu$s for $M = 1.21$, 1.36, and 1.50, respectively. These values are significantly higher than those for the best fit in the Jacob's mix width model, $\Gamma_{Fit}$, discussed in Section 4.2.

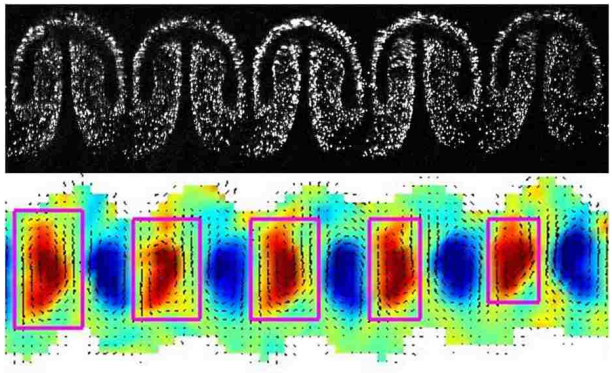

Figure 4.23: Up to five wavelengths were used to calculate an average circulation for each time. The top image shows the raw PIV data at 300 μs in a Mach 1.36 experiment, for an example. The bottom image shows the velocity field with arrows, and vorticity with the color map. The magenta boxes indicate the path along which the line integral was calculated.

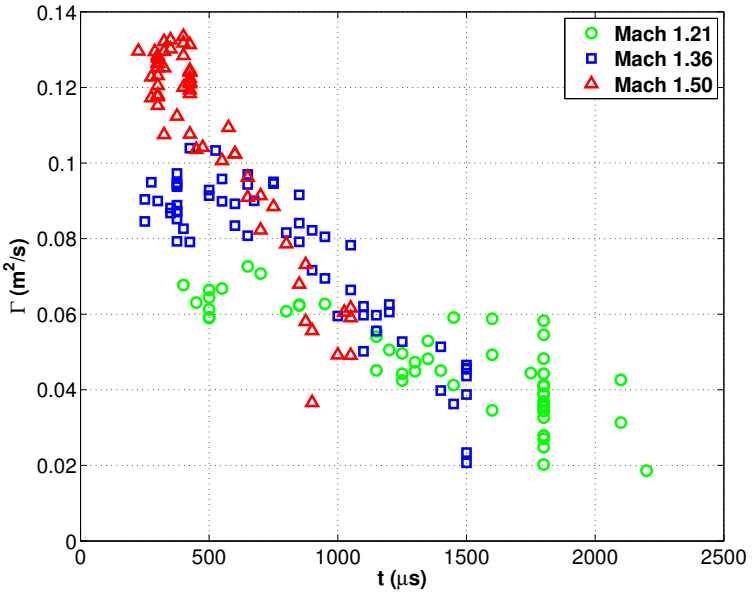


Figure 4.24: Mean circulation of up to 5 of the strongest vortices in the flow. Calculated by the line integral of the tangential component of velocity.

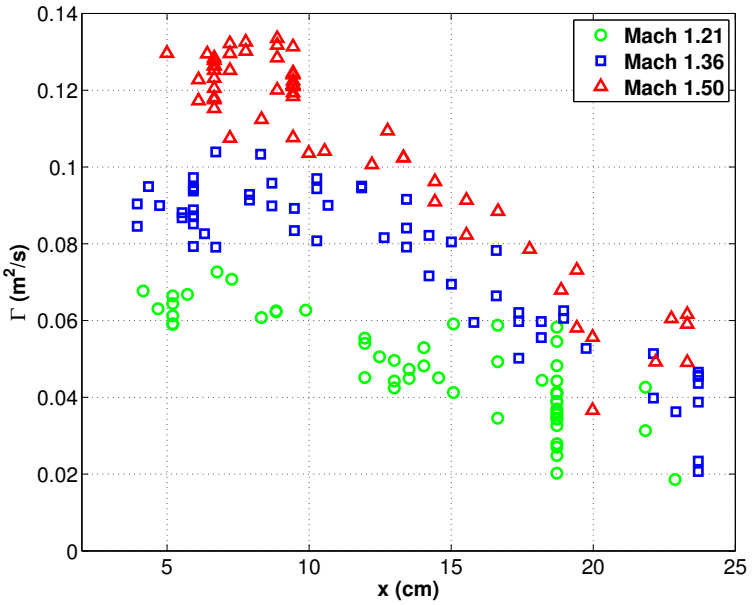


Figure 4.25: Rate of decrease of circulation with respect to scaled time is approximately the same for each case.

## 4.7 Velocity Fluctuations and Turbulent Kinetic Energy Estimates

Figures 4.26 and 4.27 show both streamwise and spanwise RMS velocity fluctuations as a function of streamwise position for different times throughout each Mach number. Inset in each plot is the density map acquired simultaneously with the velocity field to aid the reader. These plots can provide information about the state of turbulence within the mixing layer, and how chaotic the flow is. Without ensemble averages, the velocity fluctuations had to be calculated from instantaneous realizations. The RMS velocity fluctuations were calculated by first computing $\bar{u}$ and $\bar{v}$, the whole field mean of the streamwise and spanwise velocity fields, respectively. Then $\sigma_u$ and $\sigma_v$ were calculated for each streamwise position within the mixing layer by taking the RMS of the fluctuations along the spanwise direction so that

$$u'(x,y) = u(x,y) - \bar{u} \quad , \quad v'(x,y) = v(x,y) - \bar{v} \tag{4.7}$$

$$\sigma_u(x) = \sqrt{\overline{u'^2(x,y)}^{\,y}} \quad , \quad \sigma_v(x) = \sqrt{\overline{v'^2(x,y)}^{\,y}} \tag{4.8}$$

where the subscript y on the overbar indicates spanwise averaging, and $u'$ and $v'$ are the velocity fluctuations. For each Mach number case, at earlier times the velocity fluctuations are about 3 times higher in the streamwise direction with a peak at the center of the structure, while there is a local minimum in the spanwise fluctuations at the same location. These features can be explained by considering the vortex dominated structures at these early times. It is at the streamwise center of the main vortices where the streamwise velocity has the highest and lowest values. Considering an individual mushroom, the highest velocity is on the outside of the structure where material is moving faster relative to the bulk mixing layer velocity. Where the material wraps around forming the inner part of the mushroom, the slowest speeds are present. The local minimum in the spanwise fluctuations occurs because right along the streamwise center of the vortices, there is relatively little spanwise velocity.

As time progresses, the structure in these plots is lost, indicating that the velocity field is becoming more disordered, which helps confirm what is observed qualitatively in the vorticity fields. At late times, the streamwise and spanwise fluctuations obtain comparable values, providing some indication that the flow may be transitioning to an isotropic turbulent regime, although the third velocity component would be required for an accurate characterization of the true nature of the turbulence in the mixing layer.

The evolution of the probability density functions (PDFs) for the fluctuations of both components of velocity are presented in Figures 4.28, 4.29, and 4.30, with

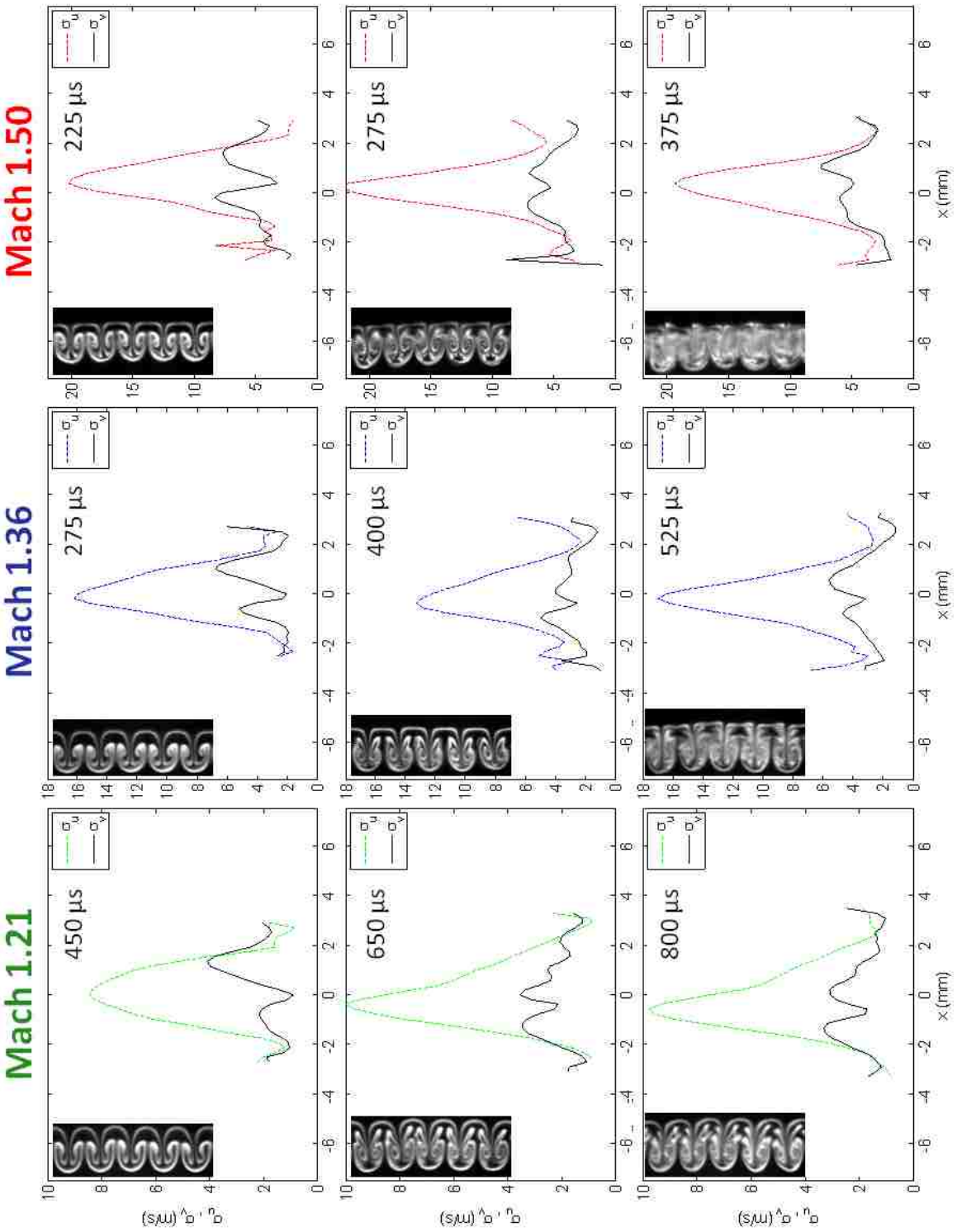


Figure 4.26: RMS of velocity fluctuations at earlier times shows flow directionality.

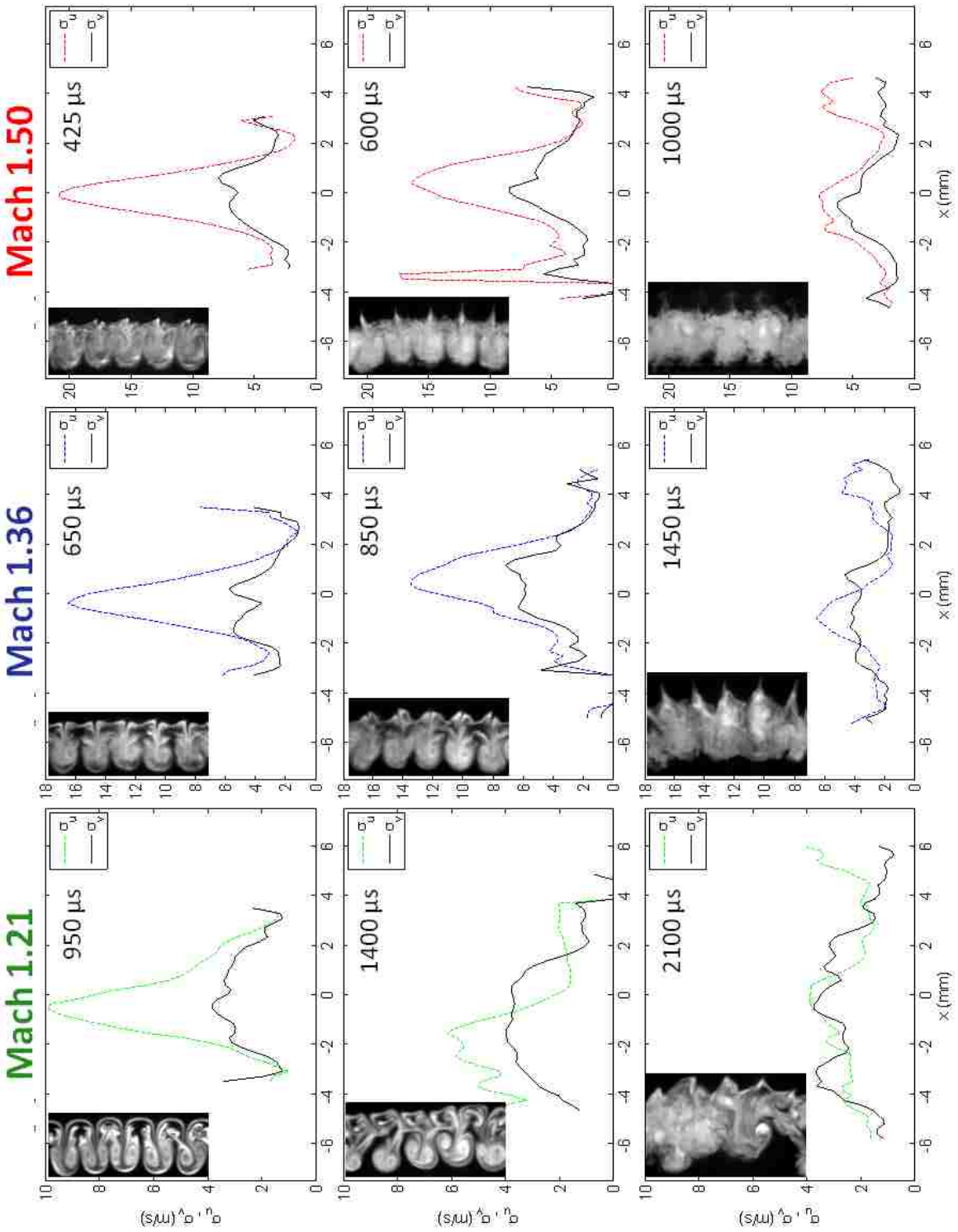


Figure 4.27: RMS of velocity fluctuations at later times provides some indication that the flow is transitioning to a state of isotropic turbulence.

a bin size of 0.25 m/s for all plots. Because turbulence is characterized by large intermittent fluctuations in velocity, the PDFs in a developing turbulent flow tend to develop non-Gaussian profiles with long tails [56]. Non-Gaussian profiles with long tails are observed at earlier times for the streamwise component, $u'$, for all three Mach numbers, but caution is required in the interpretation of these PDFs because they are calculated from single realizations. As a result, this feature is not necessarily an indication of a turbulent flow field in these experiments. Meanwhile, the PDFs of the spanwise component, $v'$, have relatively short tails. The PDFs of $v'$ also tend to be symmetric about the mean, owing to the spanwise symmetry of the flow. However, at earlier times the PDFs of $u'$ tend to be asymmetric with a higher probability for extreme negative (upstream) fluctuations than for extreme positive fluctuations. This is presumably due to the directionality of the shock wave. As time progresses, both distributions become increasingly narrow about the 0 value, and the PDFs for $u'$ become more symmetric with much shorter tails, indicating that if the flow can be defined as turbulent, the turbulence is decaying.

Comparing between Mach numbers, the PDFs of both $u'$ and $v'$ are wider with increasing $M$ for a given scaled time, $x$, indicating a wider range of scales over which velocity fluctuations occur, as more energy is deposited by higher Mach number shock waves. Also, the peak in the streamwise distribution for the higher Mach numbers tends to occur at a positive value up to $x = 10$ cm, while for Mach 1.21, the peak generally occurs very close to 0 m/s for all times, suggesting that there is a threshold Mach number, above which the directionality of the shock wave is important for this feature.

From the velocity fluctuations, it is possible to estimate the turbulent kinetic energy (TKE) field from available components as

$$K_{12}(x,y) = \frac{1}{2}(u'^2(x,y) + v'^2(x,y)) \tag{4.9}$$

where the subscript, '12', indicates that TKE was calculated from the streamwise and

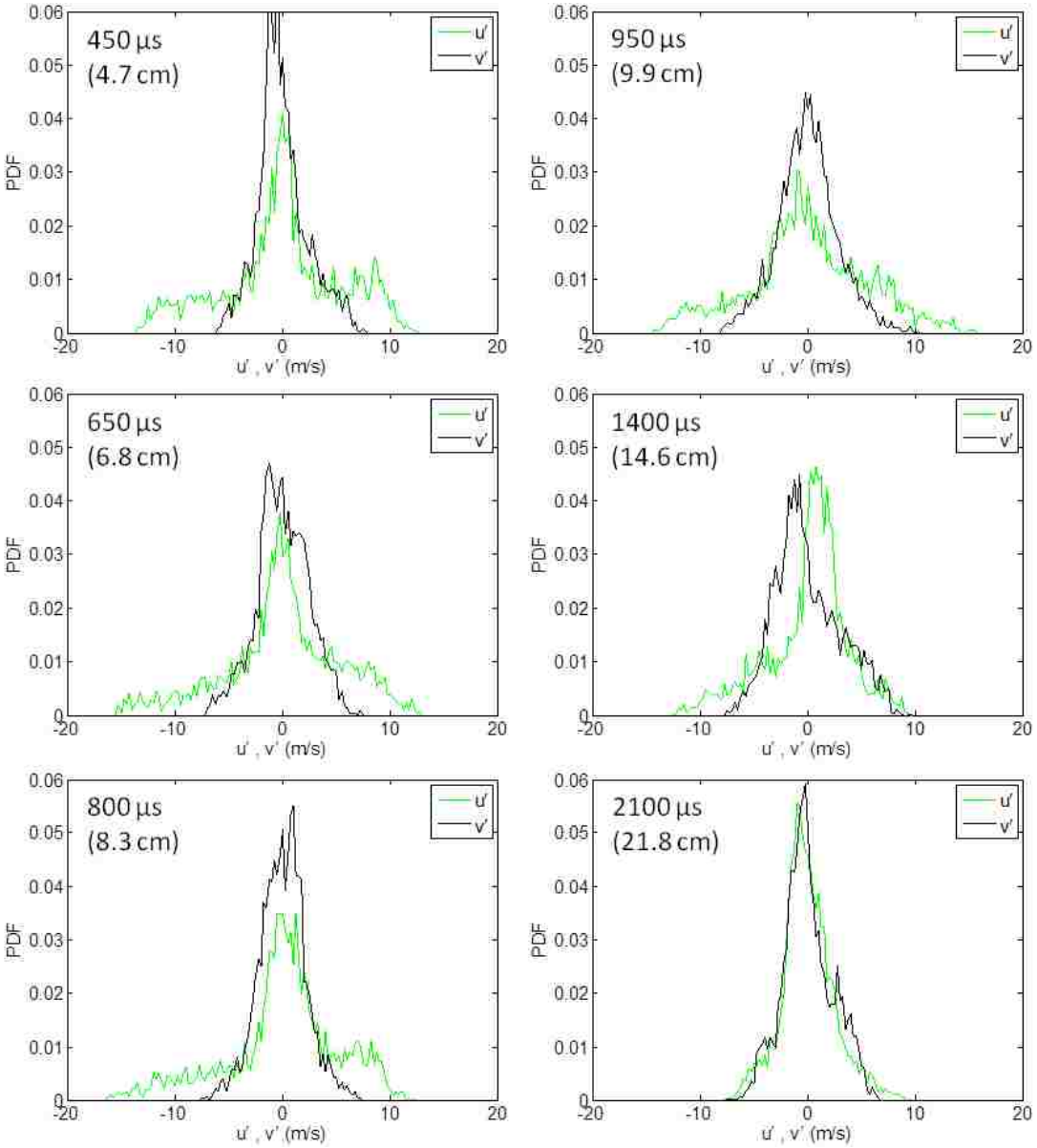


Figure 4.28: Time evolution of PDFs for velocity fluctuations in Mach 1.21 experiments.

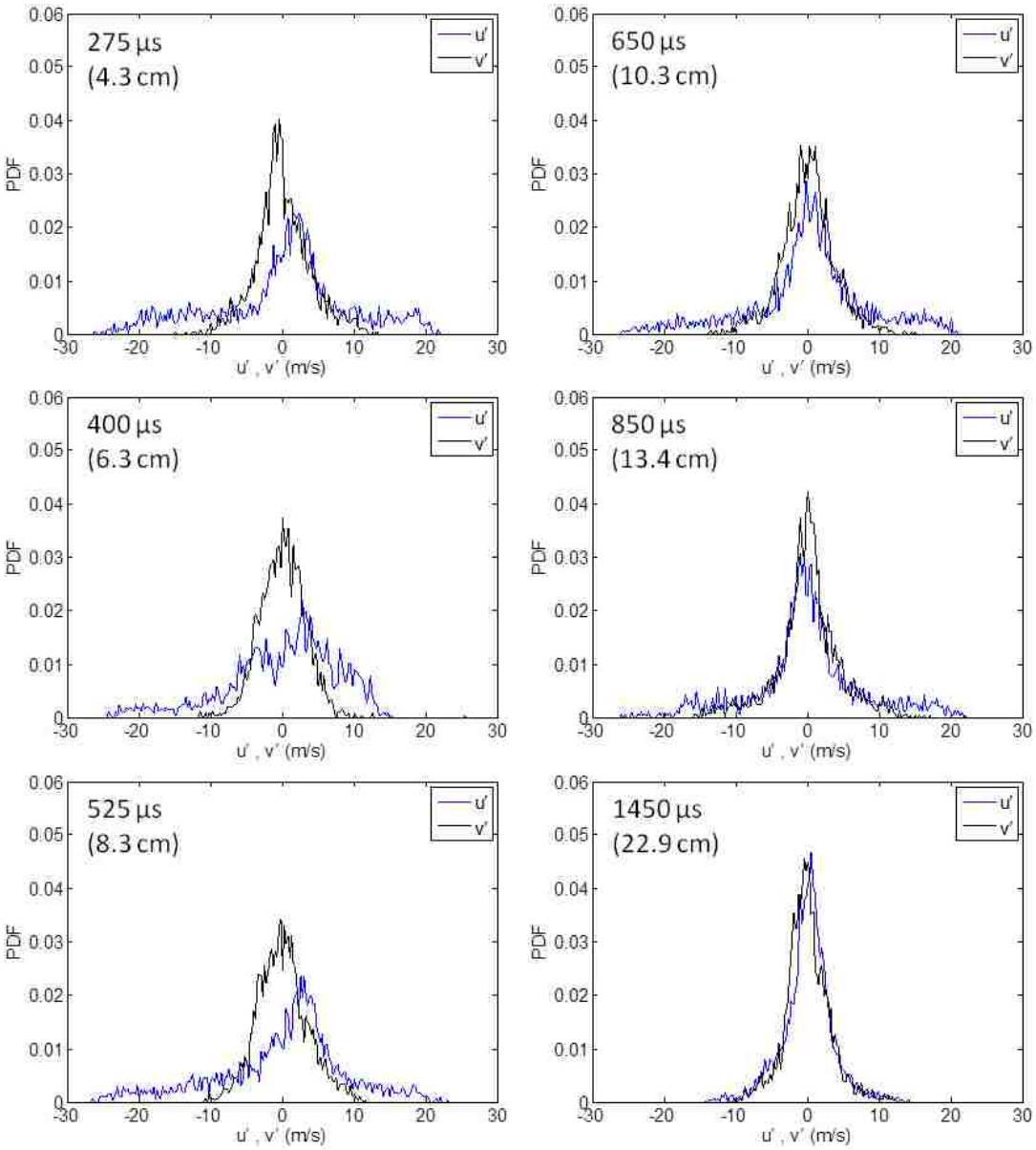


Figure 4.29: Time evolution of PDFs for velocity fluctuations in Mach 1.36 experiments.

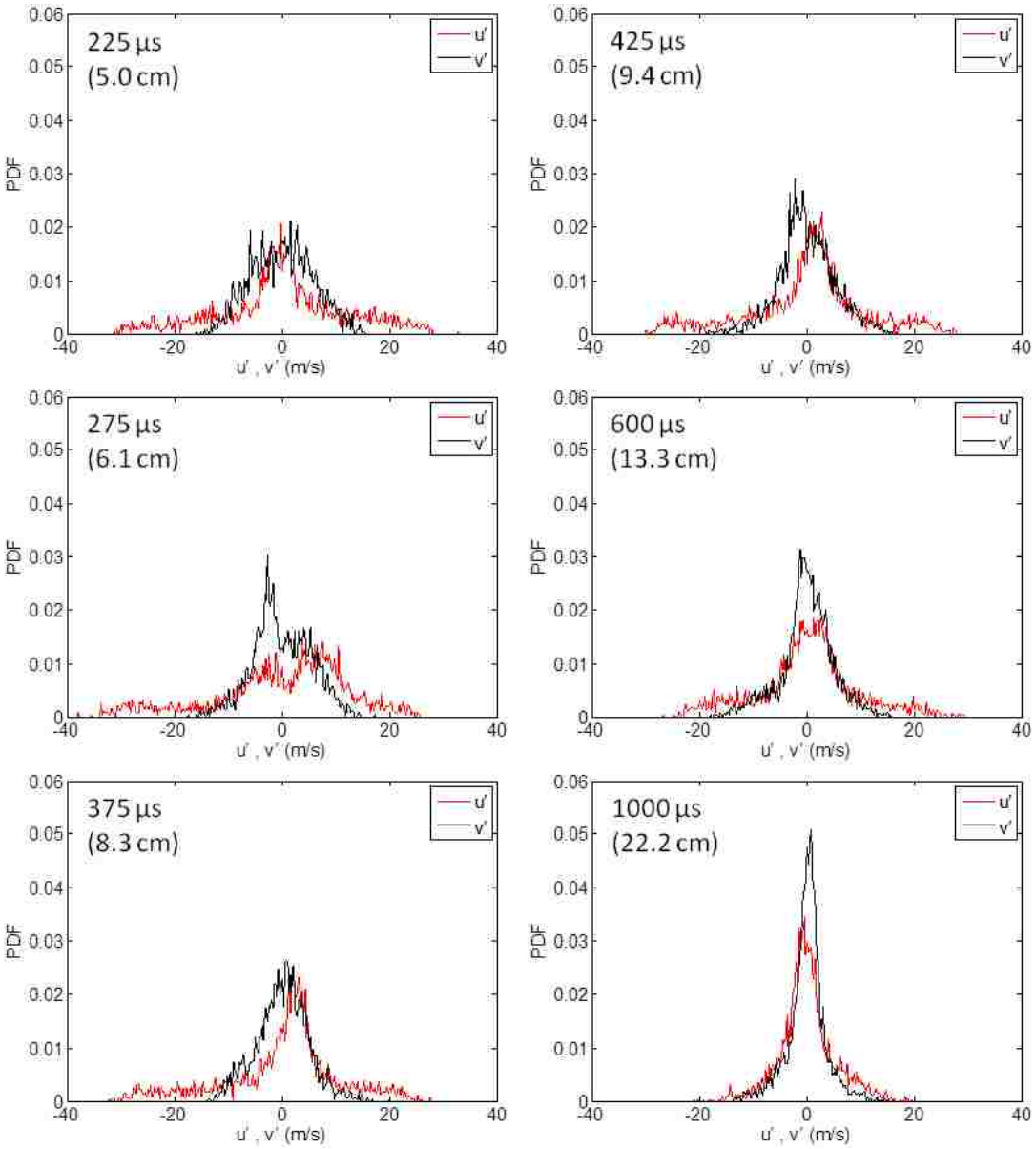


Figure 4.30: Time evolution of PDFs for velocity fluctuations in Mach 1.50 experiments.

spanwise components of velocity only (and not the vertical out of plane component).

Without ensemble averages it is not possible to calculate the true ensemble TKE. Instead, presented here is a pseudo-TKE (hereafter referred to as TKE) derived from spatially averaging over instantaneous realizations as described in Equation 4.9. Nonetheless, this method is still valuable for validation of numerical simulations where averages must also be obtained from single realizations. Even when ensemble averages are available for experimental studies of R-M flows, the fluctuating quantities can still be influenced by small differences in the ICs from shot to shot, as small differences are amplified over time, leading to unknown effects on R-M turbulence statistics [54]. Additionally, small changes in the shock speed can lead to significant differences in the location of the mixing layer from shot to shot, which also contributes error to the measurements [54].

The average TKE, $\overline{K_{12}(x,y)}$, is plotted in Figure 4.31. As can be seen, the average TKE decreases with time for each case, and at a faster rate for higher Mach numbers, indicating that energy is being transferred to smaller scales as the flow becomes more mixed. If $\overline{K_{12}(x,y)}$ is plotted against scaled time, differences in the overall values and the rate of change persist, as shown in Figure 4.32. However, if TKE is nondimensionalized using the convection velocity, $\Delta u = \langle \bar{u} \rangle$ for each Mach number case, and then plotted against scaled time, the data collapse fairly well as can be seen in Figure 4.33. In this way, the collapse of this data is achieved through use of a single parameter, $\Delta u$, applied to both axes.

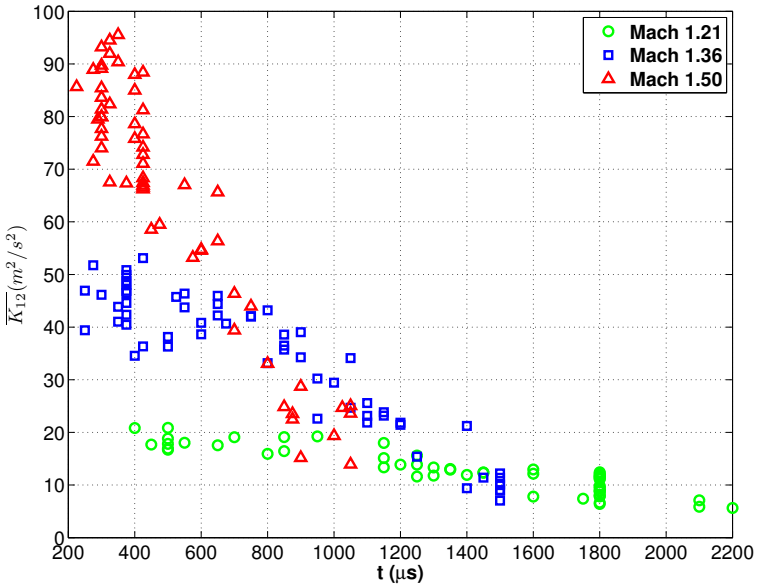


Figure 4.31: Mean of turbulent kinetic energy estimates *vs.* time.

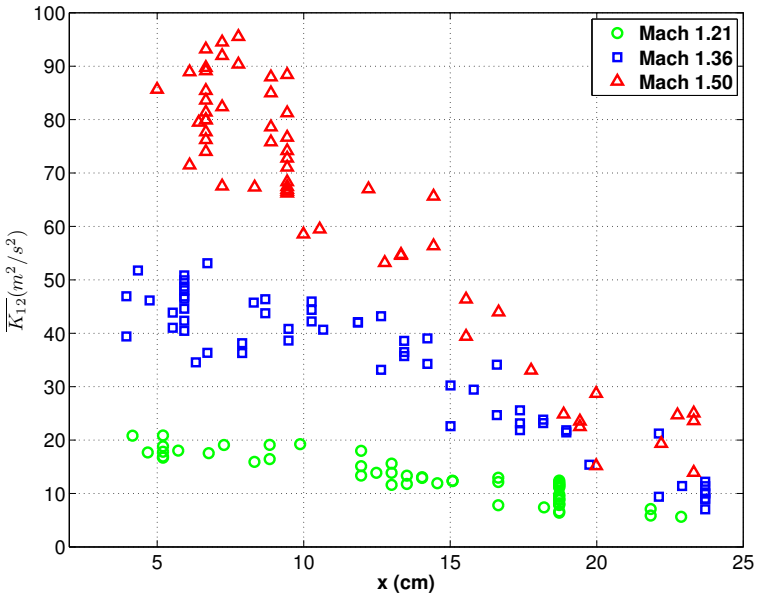


Figure 4.32: Mean of turbulent kinetic energy estimates *vs.* position.

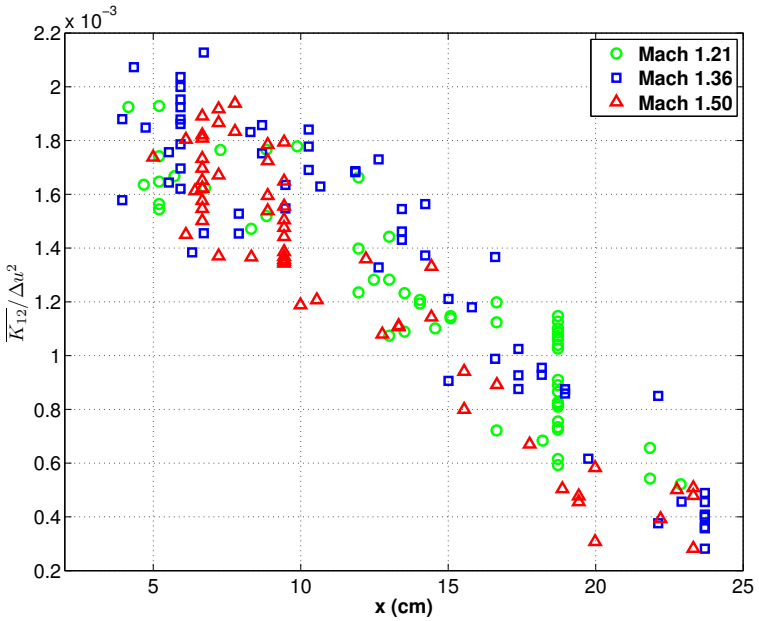


Figure 4.33: Mean of turbulent kinetic energy estimates normalized by $(\Delta u)^2$ *vs.* position.

## 4.8 Reynolds Number

The Reynolds number ($Re$) is a dimensionless number that can provide a measure of the ratio of inertial forces to viscous forces, and it's value is often used to denote the nature of the flow. Low $Re$ implies a laminar flow regime where viscous forces dominate. High $Re$ implies a turbulent flow regime where inertial forces dominate.

In RM flows, the choice of characteristic length scale and velocity remains an open question. In this study, $Re$ is defined in three ways, based on growth rate, circulation, and TKE as follows,

$$Re_\delta = \frac{\delta\dot{\delta}}{\nu} \tag{4.10}$$

$$Re_\Gamma = \frac{\Gamma}{\nu} \tag{4.11}$$

$$Re_K = \frac{\sqrt{K_{12}}\delta}{\nu} \tag{4.12}$$

where $\nu$, the post-shock kinematic viscosity ($\nu = \mu/\rho$), was determined by using normal shock relations to determine the temperature and density of both $SF_6$ and air after the passage of the particular Mach number shock wave. The temperature determines the dynamic viscosity, $\mu$. The value of $\nu$ was then taken as the average of $\nu_{air}$ and $\nu_{SF_6}$ at the appropriate conditions, so that $\nu = 9.3 \times 10^{-6}$, $8.2 \times 10^{-6}$, and $7.5 \times 10^{-6}$ m$^2$/s for $M = 1.21$, 1.36, and 1.50, respectively. Each of the time dependent Reynolds number quantities is plotted against scaled time, $x$, in Figures 4.34, 4.35, and 4.36.

$Re_\delta$ does not show obvious differences between Mach numbers, and contains a lot of scatter due to the measurement of the growth rate at each time, which is highly

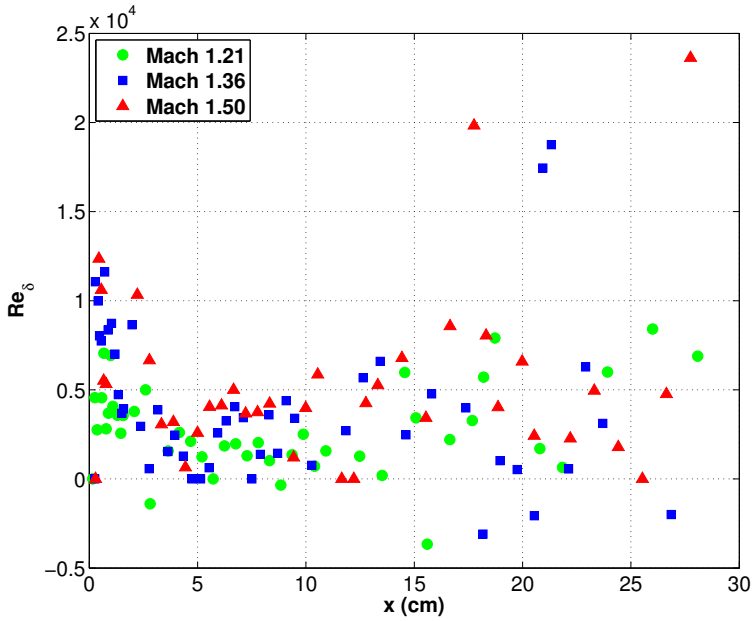


Figure 4.34: $Re_\delta$ as a function of distance traveled gives a similar value for each Mach number.

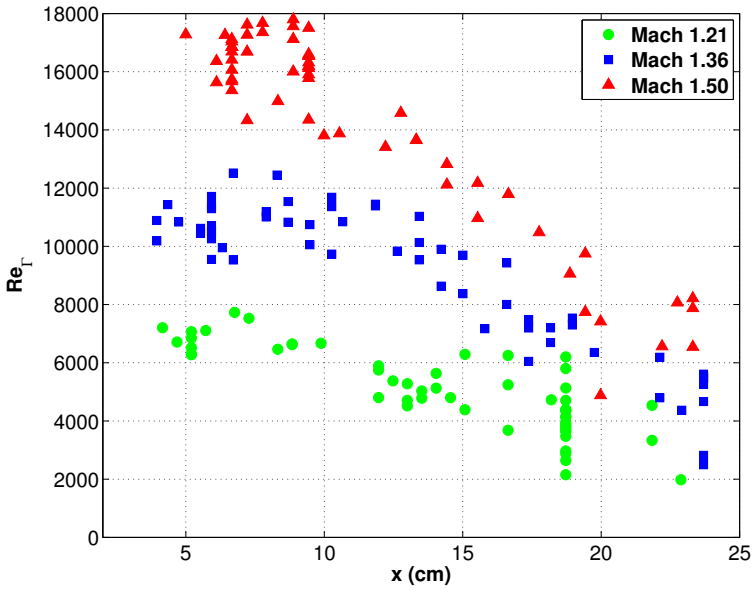


Figure 4.35: $Re_\Gamma$ as a function of distance traveled.

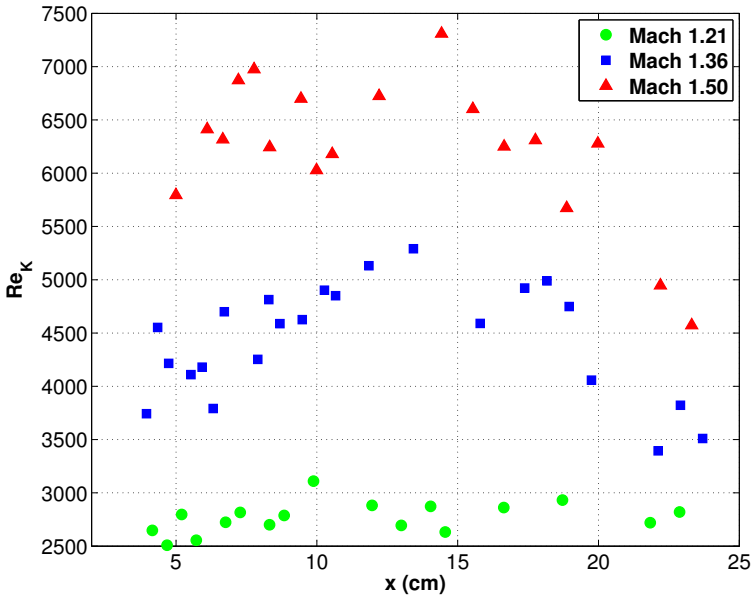


Figure 4.36: $Re_K$ as a function of distance traveled.

dependent on the variability of the ICs from one run of the experiment to the next. For this reason, this method of calculating the Reynolds number in RM experiments is generally regarded as unreliable. Still, the average value of $Re_\delta$ is roughly 5,000, which is below the currently accepted minimum value of 10,000 necessary for fully developed turbulence [57, 58]. The data used in Figure 4.34 are those from the density time series of Figures 4.2, 4.3, and 4.4.

The data used to calculate $Re_\Gamma$ include all valid PIV data, while for $Re_K$ it is only the PIV data for which there exists a simultaneous PLIF image from Figures 4.2, 4.3, and 4.4. Both of these plots show differences with Mach number, with higher $M$ yielding higher $Re$, as would be expected. The maximum measured $Re_\Gamma$ occurs between $x = 5$ and 10 cm for each Mach number and is approximately 7,000, 11,000, and 17,000 for Mach 1.2, 1.36, and 1.5, respectively. The maximum $Re_K$ occurs between $x = 10$ and 15 cm for Mach 1.36 and 1.50, but stays relatively constant for Mach 1.21. The peak values for each case are 3,100, 5,300, and 7,300 for Mach 1.2, 1.36, and 1.50, respectively.

## 4.9 Instantaneous Mixing Rate

In a recent paper, Tomkins *et al.* [59] estimated the instantaneous mixing rate, $\chi(x,y,t) \equiv D(\nabla c \cdot \nabla c)$, from quantitative concentration fields, $c(x,y,t)$, for the first time in shock accelerated flows. The mixing rate appears as a sink term in an expression for evolution of the scalar "energy" $c^2$, and thus $\chi$ is a measure of the instantaneous reduction rate of scalar fluctuations in the field. A subsequent study found differences in $\chi$, based on qualitative concentration maps, between experiments at 2 different Mach numbers, even when the time axis was scaled appropriately for collapse of the mixing width growth rate data [47]. This provided indication that the time scale for small scale mixing (which is included in $\chi$) is different than that for large scale mixing (mixing layer width, $\delta$). The current study is the first to use quantitative concentration maps to calculate instantaneous mixing rates to study Mach number effects in RM flows. The molecular diffusivity between gases, is estimated to be $D = 0.98 \times 10^{-5}$ m$^2$/s for air-$SF_6$, and the concentration maps are based on volume fraction, $c_v$ of $SF_6$. Spatial maps of $\chi(x,y) \equiv D(\nabla c_v \cdot \nabla c_v)$ can be found in Figure 4.37.

Before computing $\chi$ a threshold of 4% $SF_6$ was applied to each volume fraction map to eliminate the contribution of background noise to the measurement. However, this biases the mixing rate toward higher values by artificially creating high gradients near the borders of the mixing layer. To eliminate this bias, all values less than 4% $SF_6$ were set to a value of 4% before computing $\chi$. This does bias the results slightly toward lower than true values (by eliminating some gradients at the edge of the mixing layer), but has the advantage that it will only include contributions based on real concentration gradients in the flow field. The gradient at a given pixel location, (i,j), was calculated using the 8 adjacent pixels (4 orthogonal, 4 diagonal). With

pixel spacing $\Delta x$, $\chi(i,j)$ was then computed as

$$\chi(i,j) = D(\frac{(c_v(i,j+1) - c_v(i,j-1))^2 + (c_v(i+1,j) - c_v(i-1,j))^2}{8\Delta x^2} + \frac{(c_v(i+1,j+1) - c_v(i-1,j-1))^2 + (c_v(i+1,j-1) - c_v(i-1,j+1))^2}{16\Delta x^2}) \tag{4.13}$$

Spatially integrating over the map of $\chi(x,y)$ allows for the computation of the total 2-D diffusion-driven mixing rate, $\chi_{total} = \int\int \chi dxdy$, in each image. Figure 4.38 shows the total mixing rate plotted against time for each Mach number. At early times, as the deposited vorticity strains and stretches the heavy gas, the interfacial length is increased and the gradients are steepened, causing $\chi_{total}$ to increase rapidly, eventually reaching a peak where the diffusion based true molecular mixing is occurring approximately an order of magnitude faster ($\approx 14 \times$ as fast) than that of the curtain in absence of a shock wave. As the instability grows and small scale velocity fluctuations add to the straining and stirring, the structures become more mixed, resulting in less intense concentration gradients, and hence reduced instantaneous mixing rates. Because mixing occurs faster for higher Mach numbers, $\chi_{total}$ falls off more rapidly with increasing Mach number after the peak value is obtained.

Plotting $\chi_{total}$ against position, as in Figure 4.39, appears to collapse the data fairly well, especially after 15 cm, where all Mach numbers appear to asymptote to the same value. If inspected closely, however, some small differences do persist after scaling the time axis. For example, even in scaled time, $x$, the higher Mach number experiments show a faster increase at early times and a slightly faster decrease after peak value, indicating a quicker transition to a more uniformly mixed state, as is also evidenced by a qualitative inspection of both the concentration maps in Figure 4.9 and the $\chi$ maps in Figure 4.37. Figure 4.40 demonstrates the consistency of the current results with those from Orlicz *et al.* [47], with current results plotted over the same time and scaled time ranges. Notice that in Figure 4.37, as the vortex cores

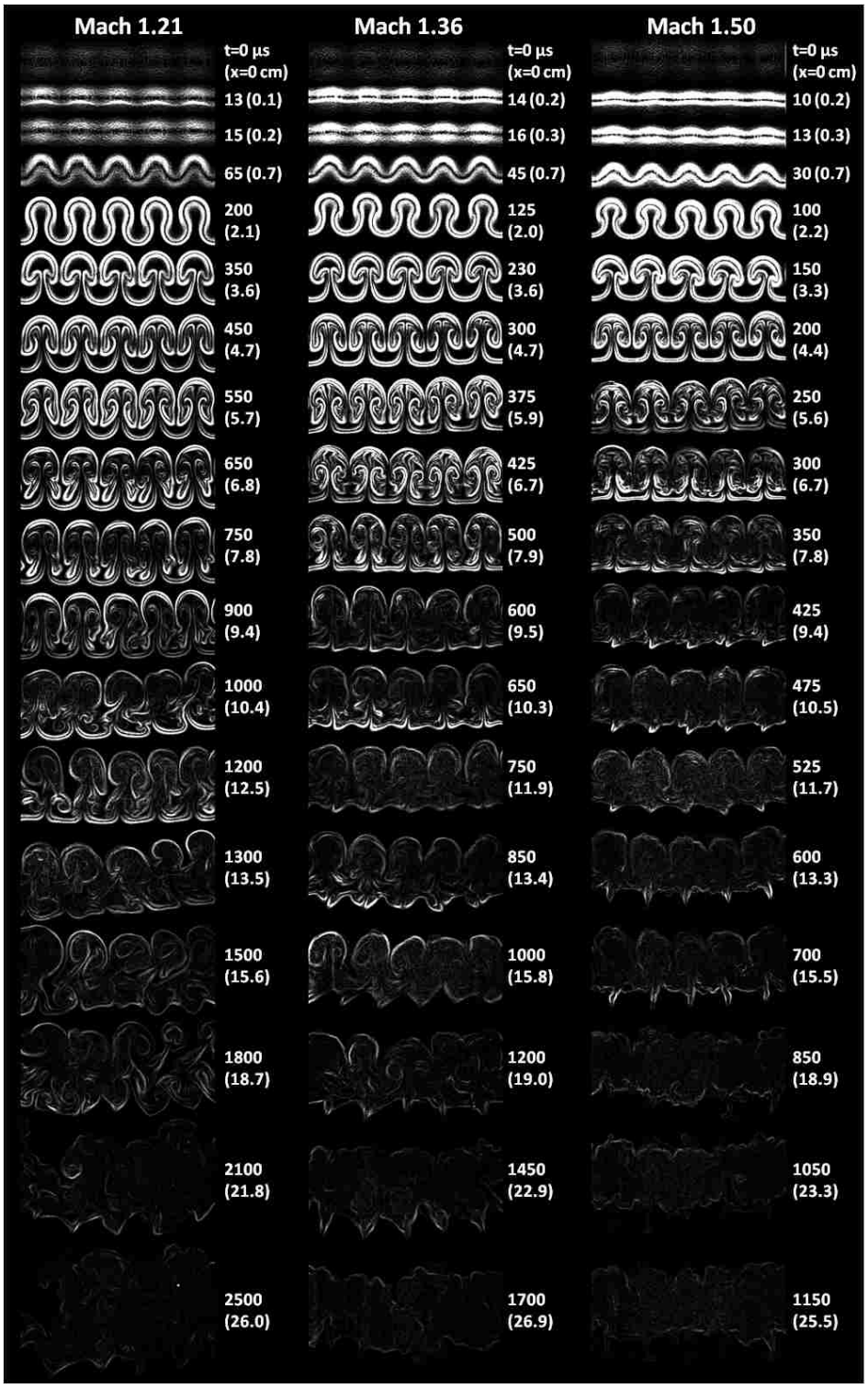


Figure 4.37: Maps of $\chi(x, y)$ corresponding to the volume fraction maps in Figure 4.9, giving time, $t$, and distance traveled, $x$. Images before 10 cm are set to a contrast of [0:640] 1/s; images after 10 cm are set to [0:384] 1/s.]

roll up, and the gradients are reduced, their contributions to $\chi$ become increasingly smaller. While, intuitively, these active regions would be expected to contribute highly to the mixing rate throughout time, their role may in fact be limited by the lack of freshly supplied air because of their location at the center of the mixing layer. This result was also observed by Tomkins *et al.* [59]. Thus, although the uniformity of mixing in these regions is relatively high, it does not necessarily imply that the amount of mixing between the heavy gas and air that takes place in these regions is high as well, relative to the rest of the mixing layer.

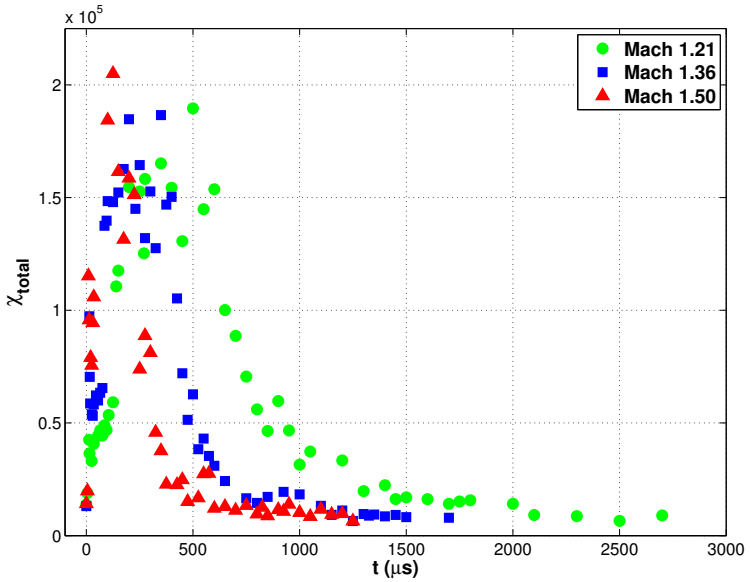


Figure 4.38: $\chi$ as a function of time.

To further quantify aspects of the mixing processes, PDFs of $\chi$ are presented in Figures 4.41, 4.42, and 4.43 for $M = 1.21$, 1.36, and 1.50, respectively. The bin size was set to 0.5 for all plots. Initially, the population of nearly all levels of $\chi$ increases as the deposited vorticity stretches and strains the interface, intensifying the gradients. After $x \approx 4$ cm, the population of nearly all levels begins to decrease with time as the diffusion based mixing begins to catch up with the straining effects caused by the velocity field.

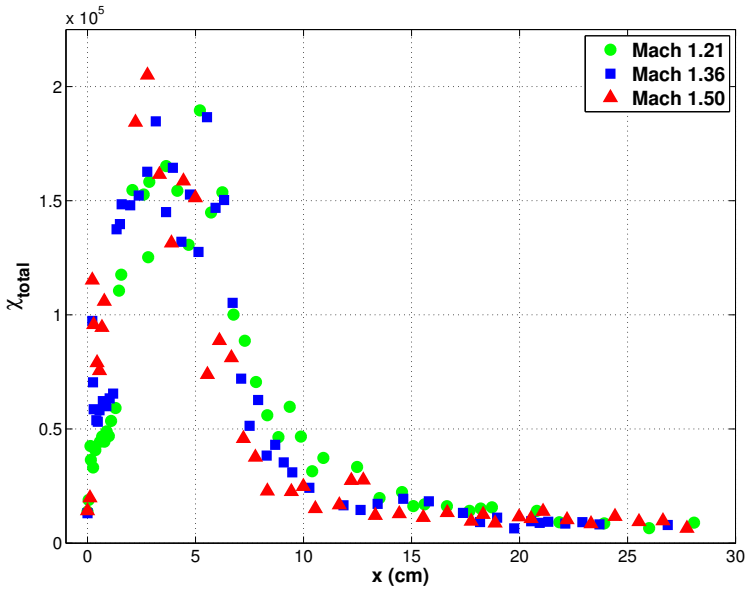


Figure 4.39: $\chi$ as a function of distance traveled.

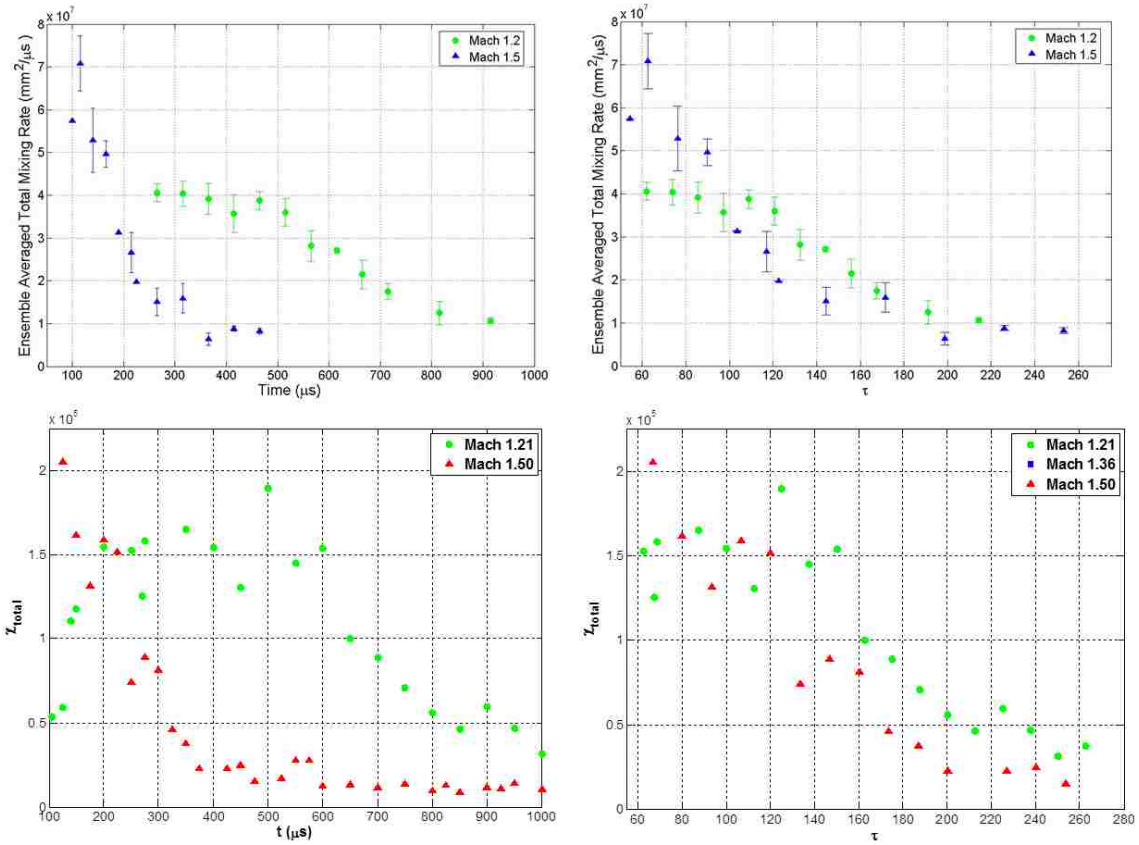


Figure 4.40: *Top*: Results for $\chi$ based on qualitative concentration maps from Orlicz *et al.* [47] comparing Mach 1.21 and Mach 1.54 experiments. *Bottom*: Current quantitative results over the same time (*left*) and scaled time (*right*) ranges as the previous study. Demonstrates consistency between the two studies.

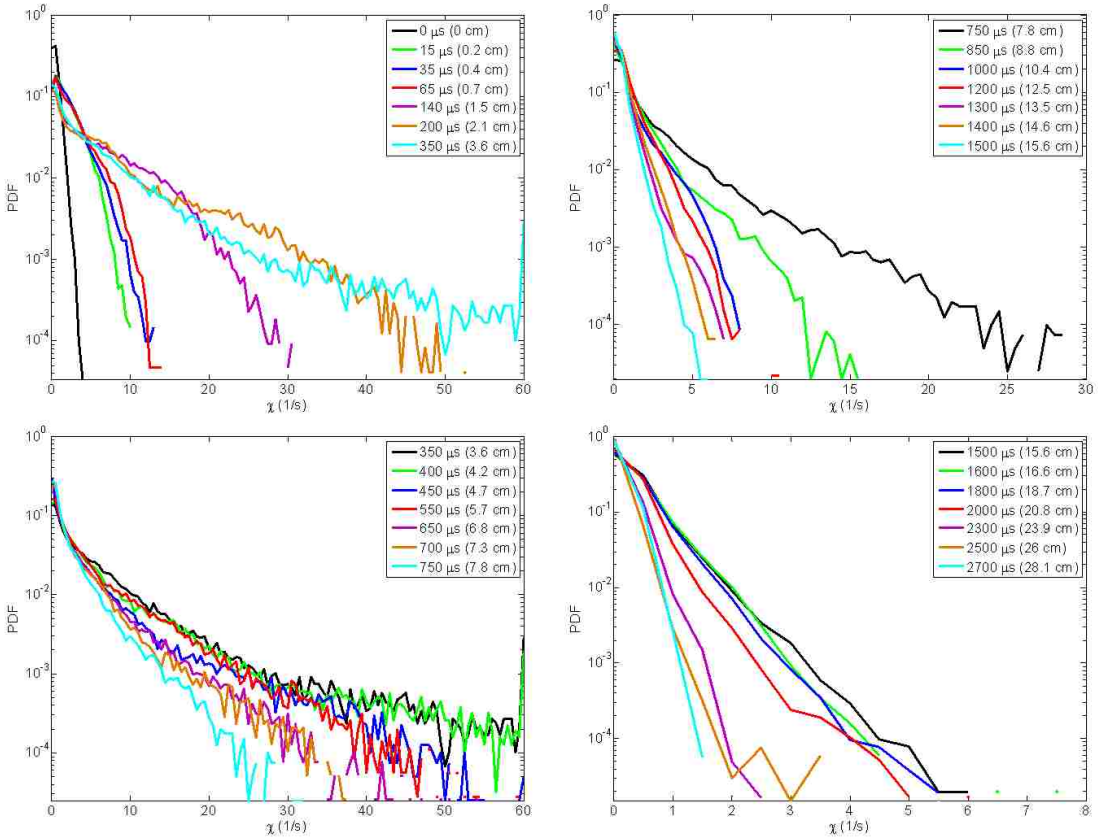


Figure 4.41: Time evolution of PDFs for $\chi$ in Mach 1.21 experiments.

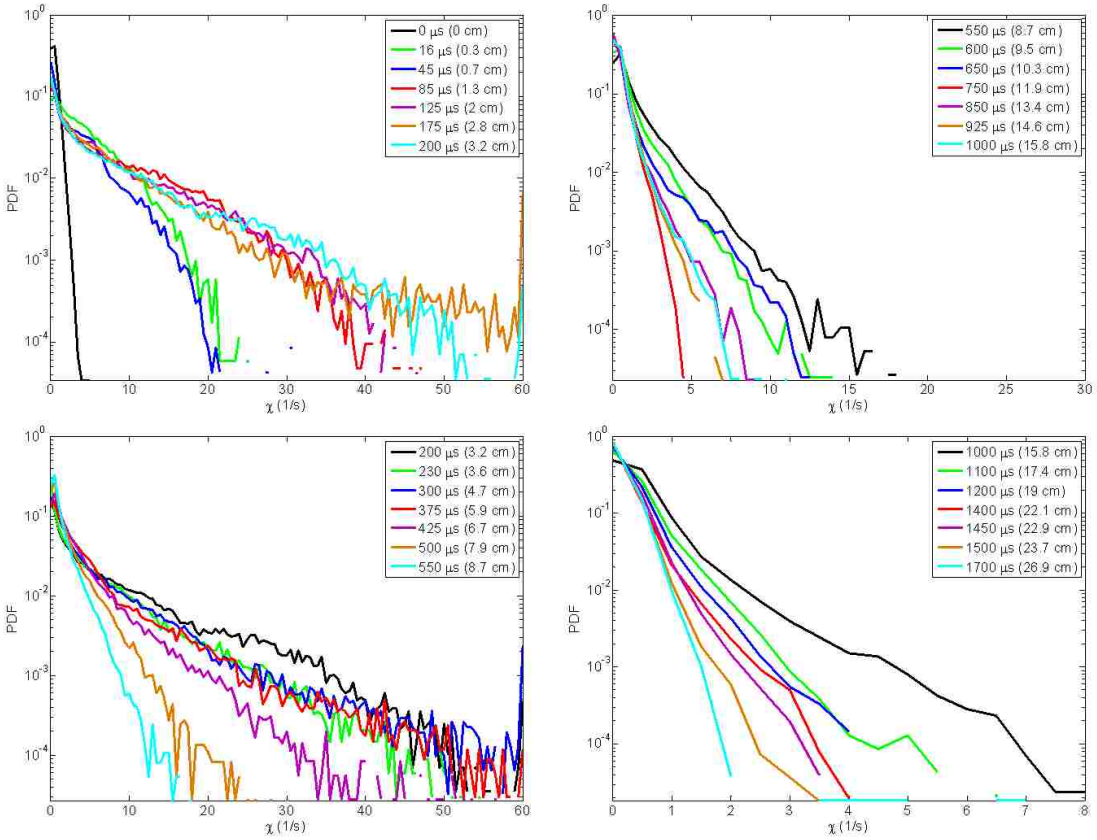


Figure 4.42: Time evolution of PDFs for $\chi$ in Mach 1.36 experiments.

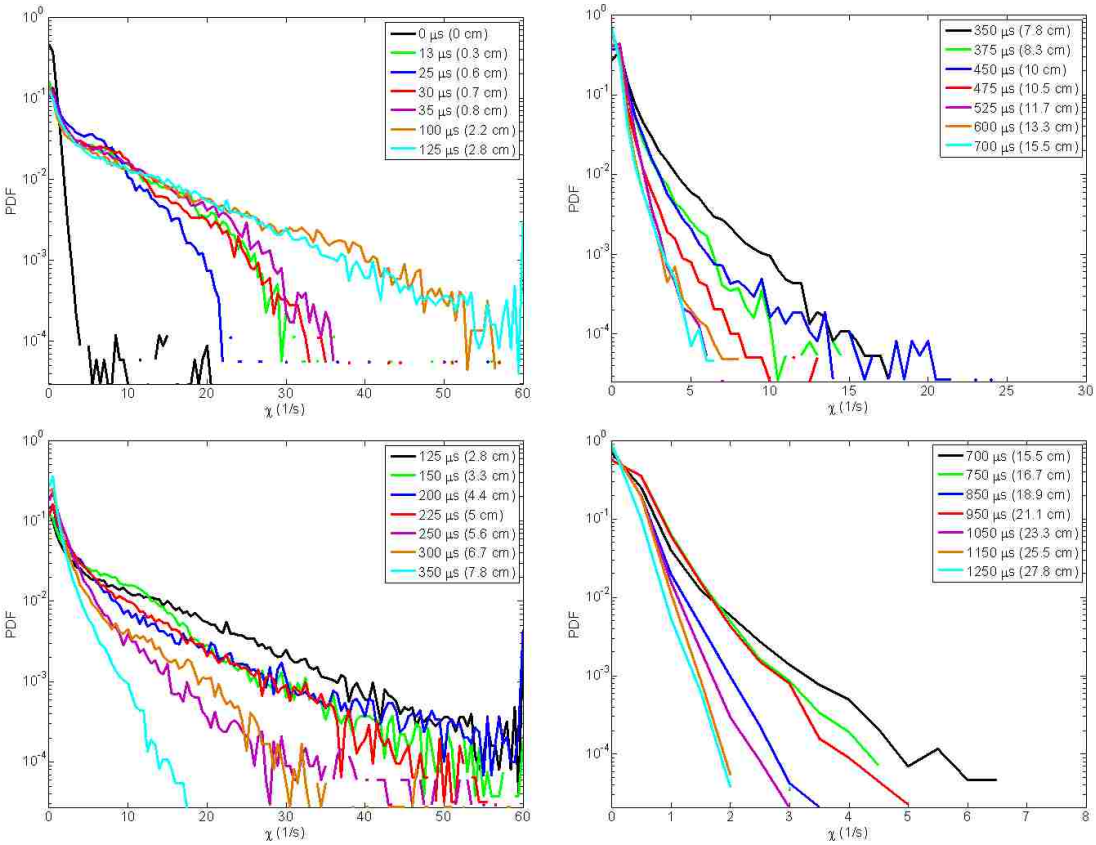


Figure 4.43: Time evolution of PDFs for $\chi$ in Mach 1.50 experiments.

## 4.10 Density Self Correlation

While $\chi$ provides a measure of the instantaneous mixing rate, the density self-correlation (DSC) parameter $b$ provides a measure of the mixedness of a variable density flow field, and can be defined using fluctuating or mean density fields as [60]

$$b = \overline{-\rho' \left(\frac{1}{\rho}\right)'} = \bar{\rho}\,\overline{\left(\frac{1}{\rho}\right)} - 1 \tag{4.14}$$

By definition, $b$ is non-negative and is equal to 0 when two fluids are fully mixed. Conversely, high values of $b$ indicate that the fluid is spatially inhomogeneous. The density self-correlation parameter appears as an unclosed multiplier in the production term of the mass flux equation for variable density flows, and therefore is important for mass transport and fluid mixing in the current experiment. The DSC parameter is one of the evolved quantities in the Reynolds averaged Navier-Stokes (RANS) turbulence model used at Los Alamos National Laboratory (named 'BHR'for Besnard-Harlow-Rauenzahn), but because it is unclosed, experimental validation data is required to know when to initialize the turbulence model during a simulation, and what values to initialize it with. The current experiment, with high resolution quantitative PLIF imaging, provides an opportunity to bound the initial value of the DSC parameter, as well as the time scale upon which initialization of a turbulence model may be appropriate.

Due to a lack of ensemble averages in the present study, $b$ must be calculated from spatially averaging over instantaneous realizations. While not ideal, previous experiments have shown that trends in $b$ calculated from instantaneous realizations are similar to those from ensemble averages, with instantaneous realizations yielding values approximately 2-3 times higher throughout the mixing layer [54]. Larger differences exist on the edges of the mixing layer where high density material projec-

tiles contribute highly to the fluctuating quantities and result in significantly higher values of $b$ when instantaneous realizations are relied upon. Understanding of these differences is important for validation of simulations that only allow the calculation of averages from single realizations [54]. Therefore, even if not accurate for the true initialization value, single realization spatial averaging may be preferable for consistency with numerical data for validation purposes.

In the current study, the bias toward much higher values at the streamwise edges of the mixing layer is removed by spatially averaging over only those pixels where $SF_6$ is present. The DSC can then be calculated from instantaneous realizations using spanwise averaged mean quantities,

$$\bar{\rho}(x) = \overline{\rho(x,y)}^{y} \tag{4.15}$$

$$\overline{\frac{1}{\rho}}(x) = \overline{\frac{1}{\rho}(x,y)}^{y} \tag{4.16}$$

$$b(x) = \bar{\rho}(x)\overline{\frac{1}{\rho}}(x) - 1 \tag{4.17}$$

or using fluctuating quantities,

$$\rho'(x,y) = \rho(x,y) - \overline{\rho(x,y)}^{y} \tag{4.18}$$

$$\left(\frac{1}{\rho}\right)'(x,y) = \left(\frac{1}{\rho}\right)(x,y) - \overline{\left(\frac{1}{\rho}\right)(x,y)}^{y} \tag{4.19}$$

$$b(x,y) = -\rho'(x,y)\left(\frac{1}{\rho}\right)'(x,y) \tag{4.20}$$

$$b(x) = \overline{b(x,y)}^{y} \tag{4.21}$$

Then, for both cases, the mean and maximum values of $b$ for the field are defined as,

$$\bar{b} = \overline{b(x)}^{x} \tag{4.22}$$

$$b_{max} = \max[b(x)] \tag{4.23}$$

Plotted in Figure 4.44 is $b_{max}$ and in Figure 4.45 is $\bar{b}$ *vs.* scaled time for each Mach number. One should use caution in the interpretation of $b$ at early times computed from instantaneous realizations, as the mixing layer is clearly not yet turbulent. Nonetheless it can still be useful for the quantitative information it provides about the state of mixedness in the flow field. Interestingly, the peak values in both figures occur at roughly the same scaled time ($x$ = 1.5 cm), and then quickly decrease to the same value by 5 cm before asymptoting at the same rate. As noted above, one potential use for experimental $b$ values could be to determine when to turn on a turbulent mixing model when running a simulation, and what value should be used to initialize it. Preliminarily, 5 cm scaled time is one candidate for the time of initialization, as $b$ is similar for all Mach numbers thereafter, and an inspection of the PLIF images reveals that this time is right before the onset of smaller scale mixing in the vortex cores.

In Figure 4.46, several plots show $b(x)$ for each Mach number at various scaled times. These plots indicate along which streamwise location across the mixing layer is the mixing most uniform. At early times the values are higher for higher Mach number as the fluid is more highly stretched and strained, leading to sharper gradients. As time progresses mixing occurs more thoroughly for Mach 1.50, leading to lower values of $b(x)$ near the center of the mixing layer, consistently lower than the other Mach number experiments.

Using only pixel values where $SF_6$ is present has the advantage that it closer approximates the true value of $b$ that would be obtained from ensemble averages. However, it then fails to capture all of the spanwise nonuniformity that exists at

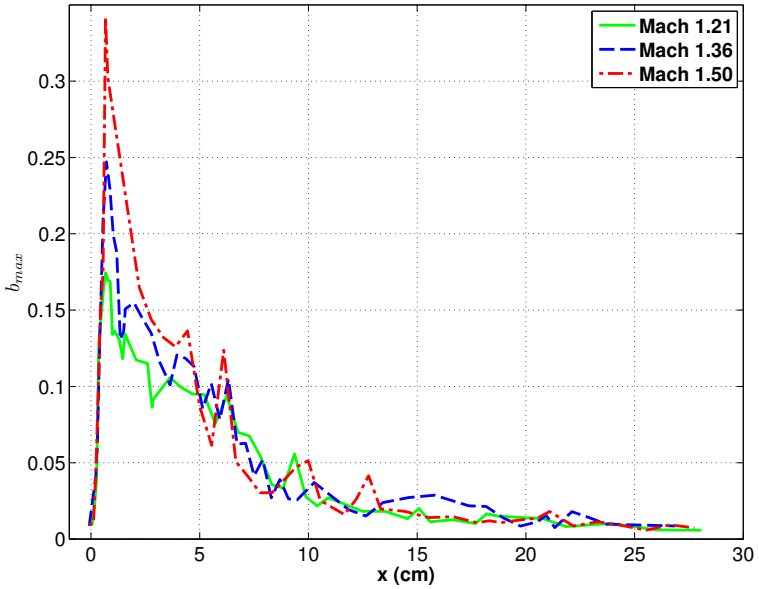


Figure 4.44: $b_{max}$ as a function of distance traveled.

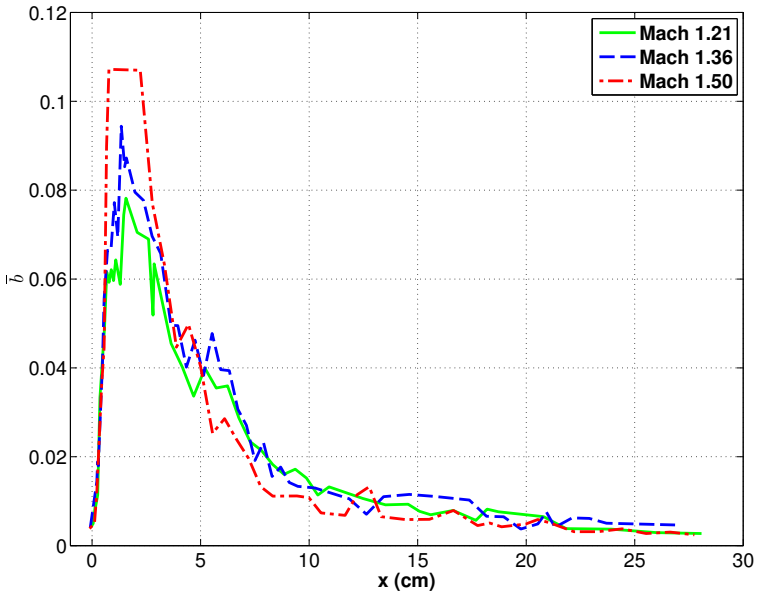


Figure 4.45: $\bar{b}$ as a function of distance traveled.

a given streamwise location. For example, in the Mach 1.21 density map at $t = 1800$ μs in Figure 4.9, pure air is observed penetrating well into the mixing layer. This does not contribute to the density fluctuations, and hence the DSC, in the current analysis. Figure 4.47 shows the difference between using whole field vs. just signal portions of the mixing layer at four different times in Mach 1.21 experiments. These plots show $b(x)$ calculated using both methods, and to the right of each plot is the density map, $b(x, y)$ using the whole field, and $b(x, y)$ using just values where $SF_6$ is present. Necessarily, using the whole field (as opposed to just signal) will always lead to equal or higher values of $b$ for all locations.

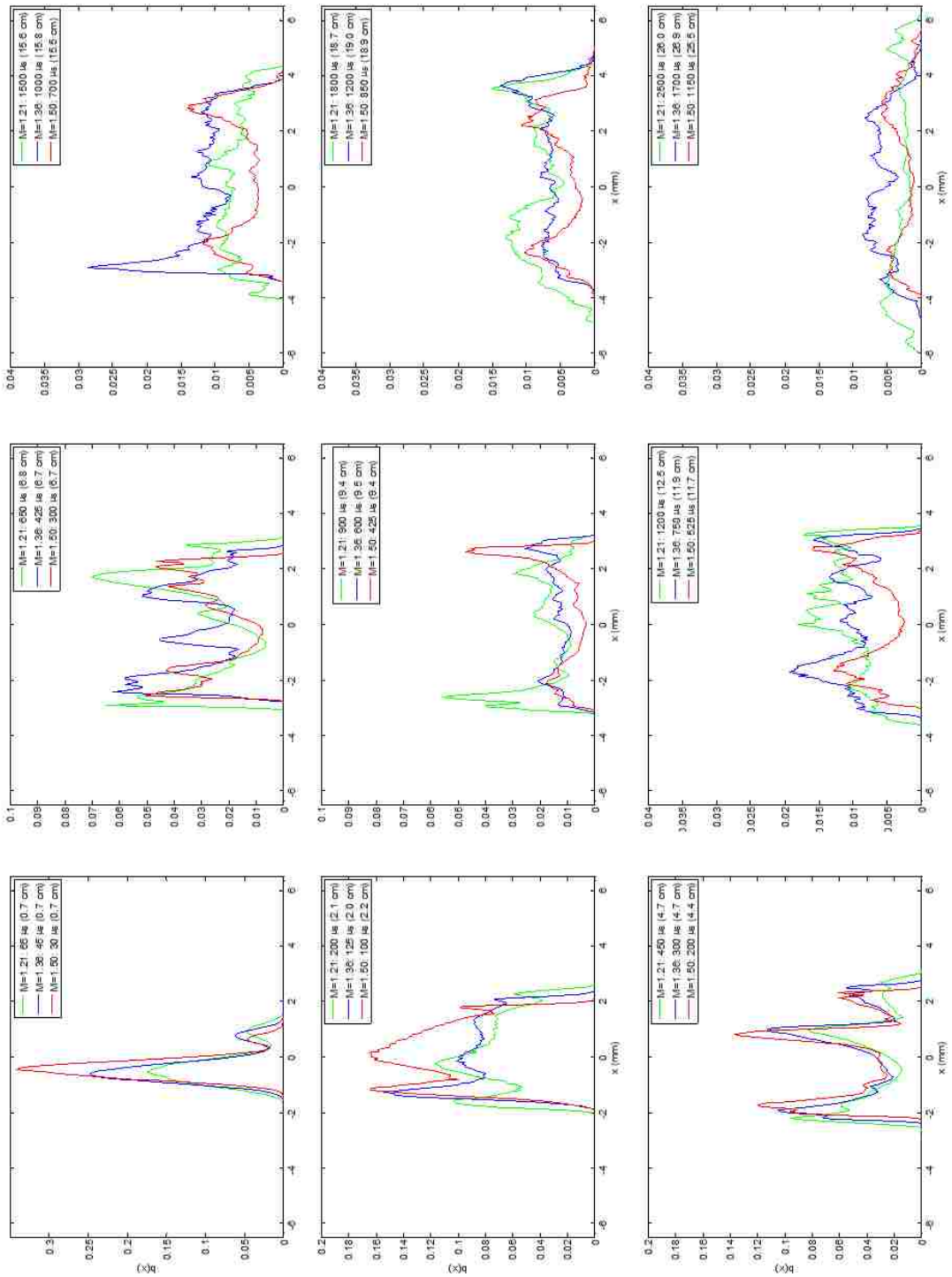

Figure 4.46: Comparison of $b(x)$ for different Mach numbers at various scaled times. Here, $x = 0$ denotes the streamwise center of mass of the mixing layer. Note that the vertical scale is not the same for all figures.

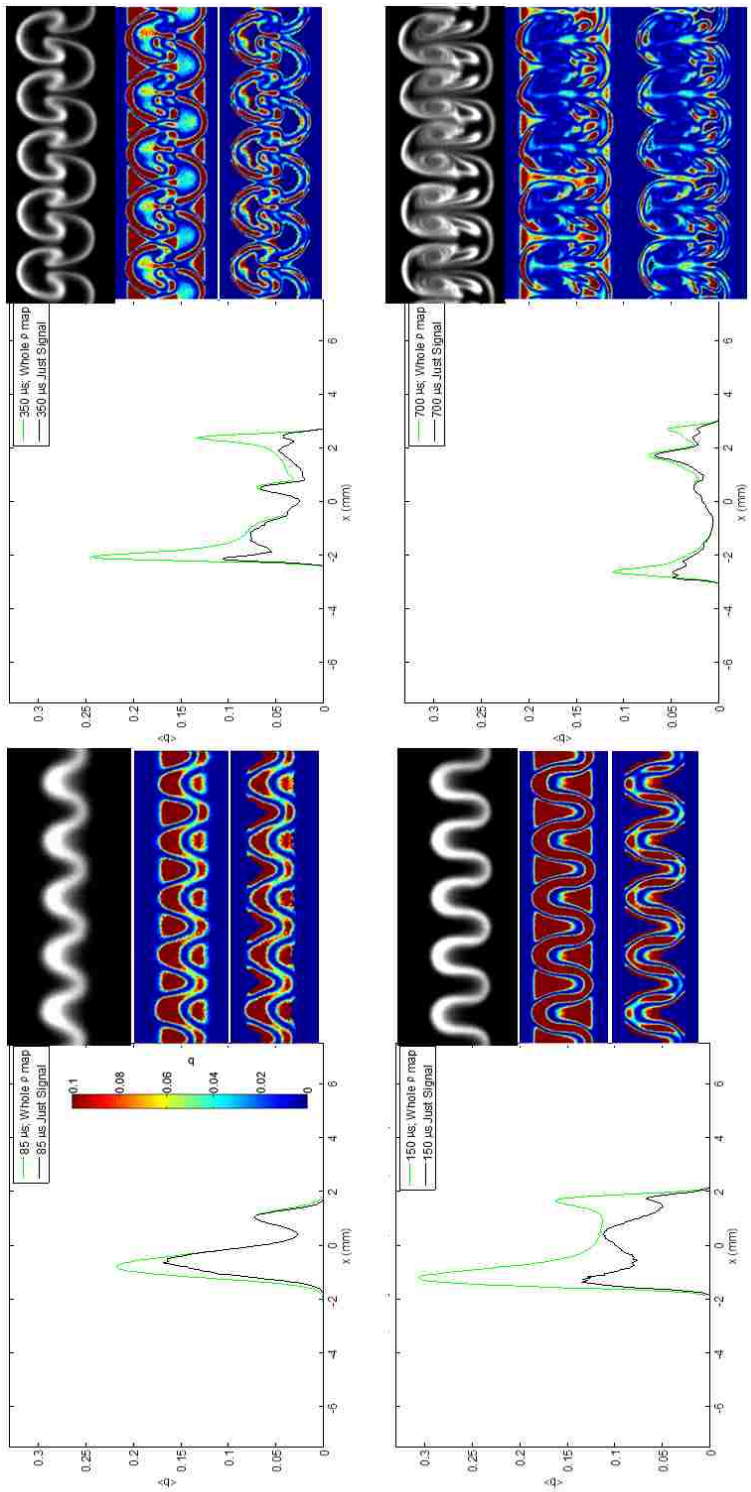


Figure 4.47: Demonstration of the differences in $b$ when spatially averaging over all pixels vs. spatially averaging over only those pixels where $SF_6$ is present. Plots show $b(x)$ at four different times in Mach 1.21 experiments. 2-D plots to the right show from top to bottom: the density map, $b(x, y)$ from the whole field, $b(x, y)$ from only pixels where $SF_6$ is present.

## 4.11 Power Spectral Density

The power spectra of the density field is another metric that can provide information about the mixedness of a variable density flow field. Shown is Figure 4.48 is the power spectral density (PSD) for the density maps at four different scaled times for each Mach number. At the first scaled time ($x = 0.55$ cm) the primary wavelength (indicated by a vertical line on the plot) is still dominant. Later at $x = 5.5$ cm, the roll up of the structures is captured by the PSDs in the emergence of peaks at smaller wavelengths. Over time, the peak at the primary wavelength decreases as the spectra smooths out for all wavenumbers, reflecting the degree to which fluid mixing has occurred. By the latest time shown ($x = 22$ cm), the peak at the primary wavelength has disappeared for each Mach number, as a combination of true mixing and asymmetric material transport (the latter, seemingly more important in Mach 1.21 experiments) serve to broaden the spectrum.

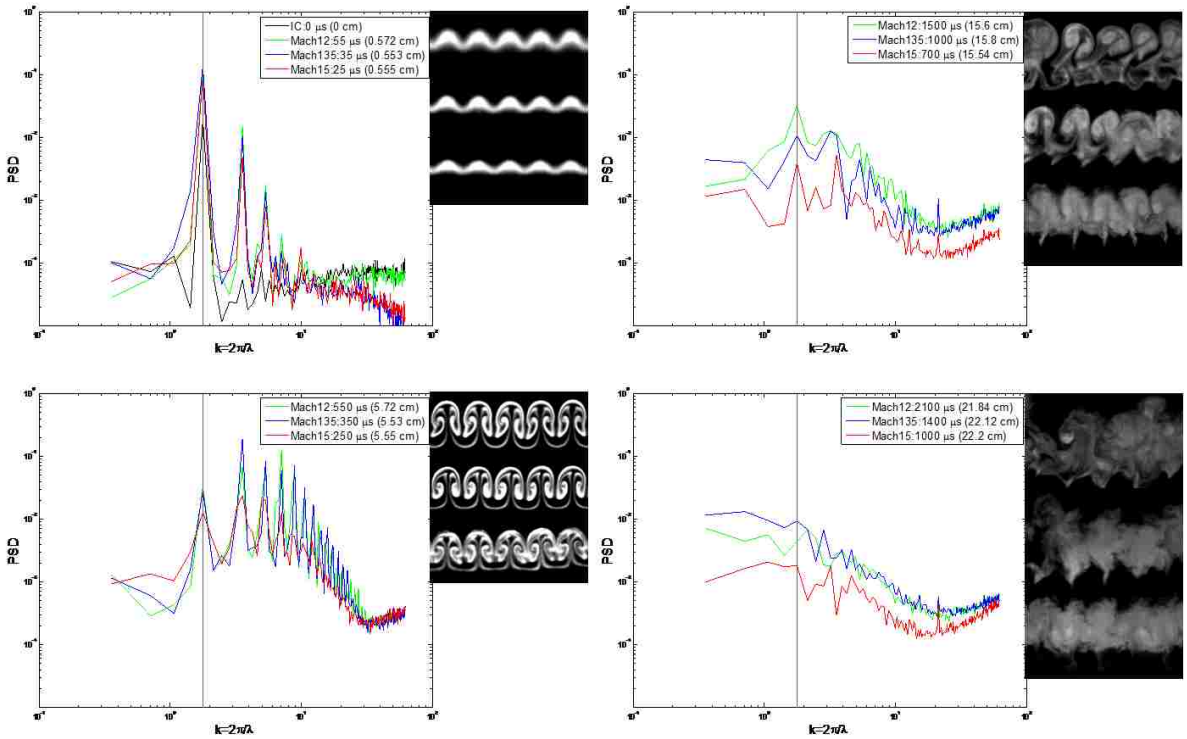


Figure 4.48: PSDs of the density field at four different scaled times. Density maps corresponding to each plot are in order of increasing Mach number from top to bottom.

## 4.12 Other Measures of Mixedness

The total area over which there exists signal at or above the 5% $SF_6$ volume fraction level is plotted against distance traveled in Figure 4.49. Total area gives a sense of how spread out the mixing layer has become in two dimensions, and perhaps is more useful for quantifying the degree of mixing than the total width, $\delta$ (presented above in Sections 4.2 and 4.3), because measurements of $\delta$ can be influenced by projectile features that do not make large contributions to the true molecular mixing of the two fluids. An increase in the area where heavy gas is present implies an increase in molecular mixing. As can be seen in Figure 4.49, after $x = 10$ cm, the total area decreases with increasing Mach number, implying the somewhat counterintuitive result that lower Mach number shock waves generate more mixing over a given distance traveled. A related measure of mixedness is the mean volume fraction of $SF_6$ among all pixels that contain signal, $\overline{c_v}$. Only those pixels at or above the 5% $SF_6$ volume fraction level were considered. Shown in Figure 4.50 is a plot of $\overline{c_v}$ *vs.* distance traveled. Because the PLIF images were processed using a conservation of mass assumption, $\overline{c_v}$ takes the form of an inverse function of the total area. Therefore, after 10 cm, $\overline{c_v}$ increases with increasing Mach number, also implying more mixing for lower Mach numbers over a given amount of distance traveled. Note that this is not to be confused with the uniformity of mixing. As seen in the PLIF images of Figure 4.9, the uniformity of mixing appears to increase with increasing Mach number at a given distance traveled.

If diffusion is the mechanism by which two fluids molecularly mix, then one could arrive at a first order approximation for the total area, and the mean volume fraction over a given amount of time using the diffusion length scale for two dimensional diffusion,

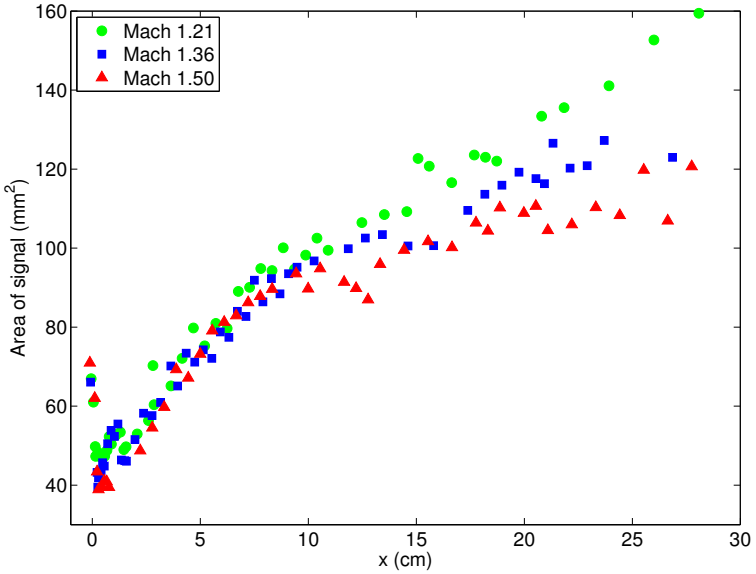


Figure 4.49: Area of PLIF signal as a function of distance traveled.

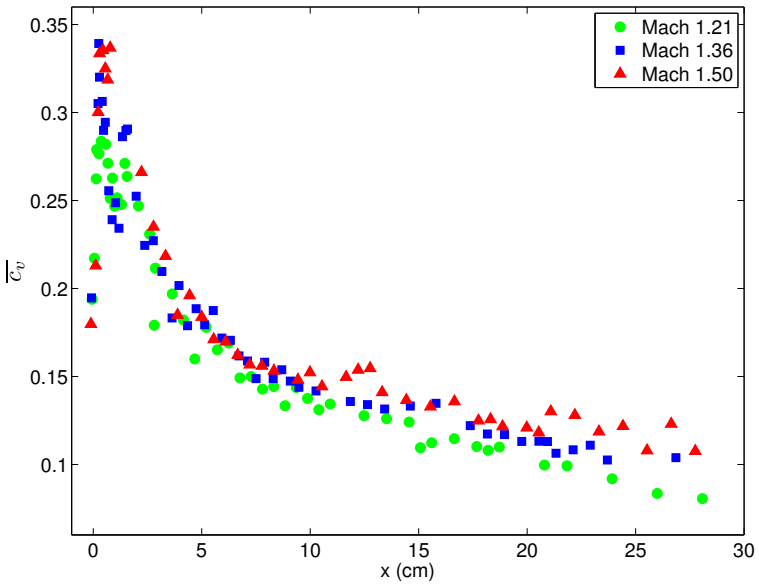


Figure 4.50: $\overline{c_v}$ as a function of distance traveled.

$$d = \sqrt{4D\Delta t} \tag{4.24}$$

where $D$ is the coefficient of diffusivity between air and $SF_6$ and $\Delta t$ is time. The total time of the experiment is $\Delta t$ = 2700, 1700, and 1250 μs for $M$ = 1.21, 1.36, and 1.50, respectively. Then the diffusion length is $d$ = 325, 258, and 221 μm (or in pixels, $d$ = 6.4, 5.1, and 4.4) for $M$ = 1.21, 1.36, and 1.50, respectively. If time variant concentration gradients and motions due to the velocity field are ignored, a single pixel sized parcel of heavy gas located at the interface with air should diffuse out over a distance $d$ in the direction of the air. Only those locations in the flow field that are near the interface between heavier gas and air will actually contribute to area enhancing diffusion based mixing. Therefore, a custom code was written to find the length of the interface at the 5% $SF_6$ volume fraction level. Presented in Figures 4.51 and 4.52 is the variation of interface length with time and distance traveled, respectively. Because the interfacial length changes in time due to stretching and straining imposed by the velocity field, followed by subsequent mixing, a choice for the number of pixels that will contribute to an increase in the area must be estimated. This was achieved by linearly interpolating between the data points in Figure 4.51 and finding the average interface length of the interpolation, $L_{avg}$. Then, the interfacial area at the latest time, $A_{final}$ in each experiment may be estimated as,

$$A_{final} = A_0 + dL_{avg} \tag{4.25}$$

where $A_0$ = 66 mm$^2$ is the area of the initial conditions. Using this expression, $A_{final}$ was estimated to be 108, 92 and 86 mm$^2$ for $M$ = 1.21, 1.36, and 1.50, respectively, as shown in Table 4.2. Experimentally measured values for the final mixing layer area are 160, 127 and 121 mm$^2$ for $M$ = 1.21, 1.36, and 1.50, respectively. Hence the experimentally measured values are approximately 1.4 times greater than the estimated values using Equation 4.25 for each Mach number case. This suggests

that diffusion plays a dominant role in the mixing process, and that it can be used to explain the differences observed in the mixing layer area between different Mach number experiments.

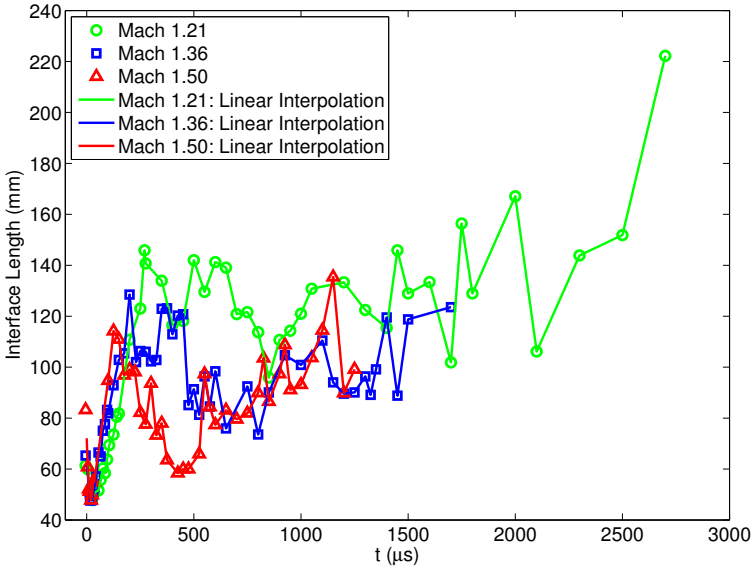


Figure 4.51: Interface length at the 5% $SF_6$ volume fraction level as a function of time. Linear interpolation was used to estimate average interfacial length over time for each Mach number case.

Table 4.2: List of values pertaining to Equation 4.25. Measured values of the final interfacial area are approximately 1.4 times higher than estimated values for each Mach number.

| | | $M = 1.21$ | $M = 1.36$ | $M = 1.50$ |
|---|---|---|---|---|
| $d$ | (μm) | 325 | 258 | 221 |
| $L_{avg}$ | (mm) | 130 | 99 | 88 |
| $\Delta t$ | (μs) | 2700 | 1700 | 1250 |
| $A_0$ | ($mm^2$) | 66 | 66 | 66 |
| $A_{final}(Estimated)$ | ($mm^2$) | 108 | 92 | 86 |
| $A_{final}(Measured)$ | ($mm^2$) | 160 | 127 | 121 |

The discrepancy between the estimated and measured final area is likely attributed to a number of simplifying assumptions used in this analysis. These include: the interfacial length is constant and equal to the average interfacial length

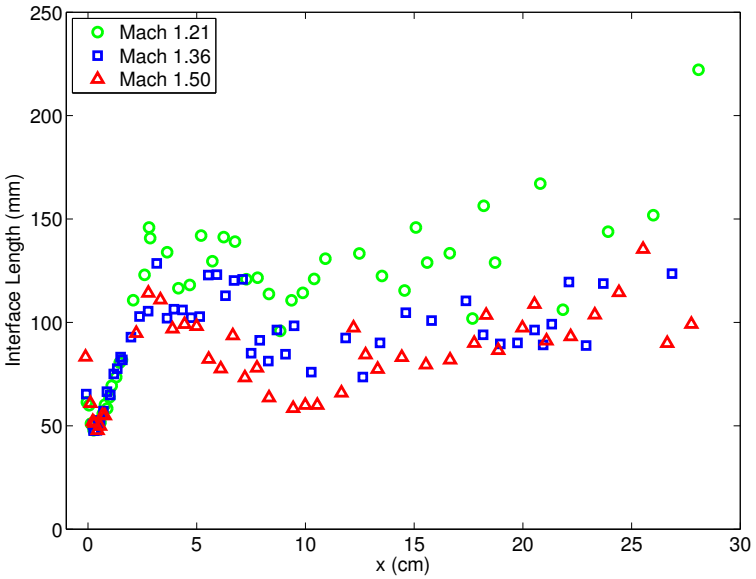


Figure 4.52: Interface length at the 5% $SF_6$ volume fraction level as a function of distance traveled.

measured from the experiments, $D$ is constant in space and time, the interface is initially sharp, the resolution of the camera is enough to distinguish between stirring (closely spaced material lines transported by the velocity field) and molecular mixing (diffusion based) at all times, the total mass of acetone (hence $SF_6$) in the imaging plane is constant for all realizations, and 3-D contributions to mixing or apparent mixing are not important. Nonetheless, this diffusion based analysis provides some justification for the observation that lower Mach number shock waves generate more mixing at the same scaled time. It is likely at least partly due to the additional real time and the additional interfacial length (because of less compression in lower Mach number experiments) over which diffusion acts.

While the total signal area and $\overline{c_v}$ indicate how much air has mixed with $SF_6$, the streamwise profile of the mean volume fraction of $SF_6$, $\overline{c_v}(x)$, can indicate how uniform is the mixing. Figure 4.53 compares $\overline{c_v}(x)$ for each Mach number at nine different scaled times, with the center of mass location indicated by 0 mm on each

horizontal axis. It is important to note the distinction between $\overline{c_v}$, the mean volume fraction of $SF_6$ among only those pixels that contain signal, and $\overline{c_v}(x)$, the mean volume fraction of all pixels along a given streamwise location. The plots of $\overline{c_v}(x)$ in Figure 4.53 are similar for each Mach number in terms of the number of local peaks and troughs until intermediate times beginning at 6 cm scaled time, when the structures begin to grow differently (as it was noted in Section 4.1). The existence of multiple peaks and troughs illustrates a lack of uniformity of the mixing across the mixing layer. Conversely, a top hat shaped profile would indicate completely uniform mixing, at least in a spanwise averaged sense. By ∼7 cm, the number of local peaks in the Mach 1.50 experiments begin reducing. At this scaled time, the number of local peaks in $\overline{c_v}(x)$ is 5, 4, and 3 for $M = 1.21$, 1.36, and 1.50, respectively. By ∼16 cm it is 3, 2, and 1 for $M = 1.21$, 1.36, and 1.50, respectively, indicating that mixing is indeed occurring more uniformly throughout the mixing layer, even in scaled time, as Mach number is increased. At ∼26 cm, $\overline{c_v}(x)$ for the Mach 1.50 experiment is the smoothest of the 3 cases, and the most symmetric about the streamwise center of mass location, confirming that it is the most uniformly mixed. Nonetheless, the Mach 1.50 case does have the highest values of $\overline{c_v}(x)$, which is consistent with the previous observation from Figure 4.50 that higher Mach number results in less overall mixing between the air and heavy gas when compared at the same distance traveled.

Information about the amount and uniformity of mixing is also contained in PDFs of the volume fraction of $SF_6$, which are shown in Figures 4.54, 4.55, and 4.56. A threshold of $c_v = 0.05$ was applied to the images before processing to eliminate contributions due to background noise, and bin size was set to 0.005 for all cases. Again, the features of the PDFs are fairly similar for each Mach number until after 6 cm scaled time. At that point, the Mach 1.50 experiments begin developing a local trough at low values of $c_v$, followed by a similar pattern in Mach 1.35 experiments beginning at 12 cm. This feature of the PDFs is labeled "trough" in Figures 4.55 and 4.56. As time progresses, the peak distribution for all Mach numbers becomes

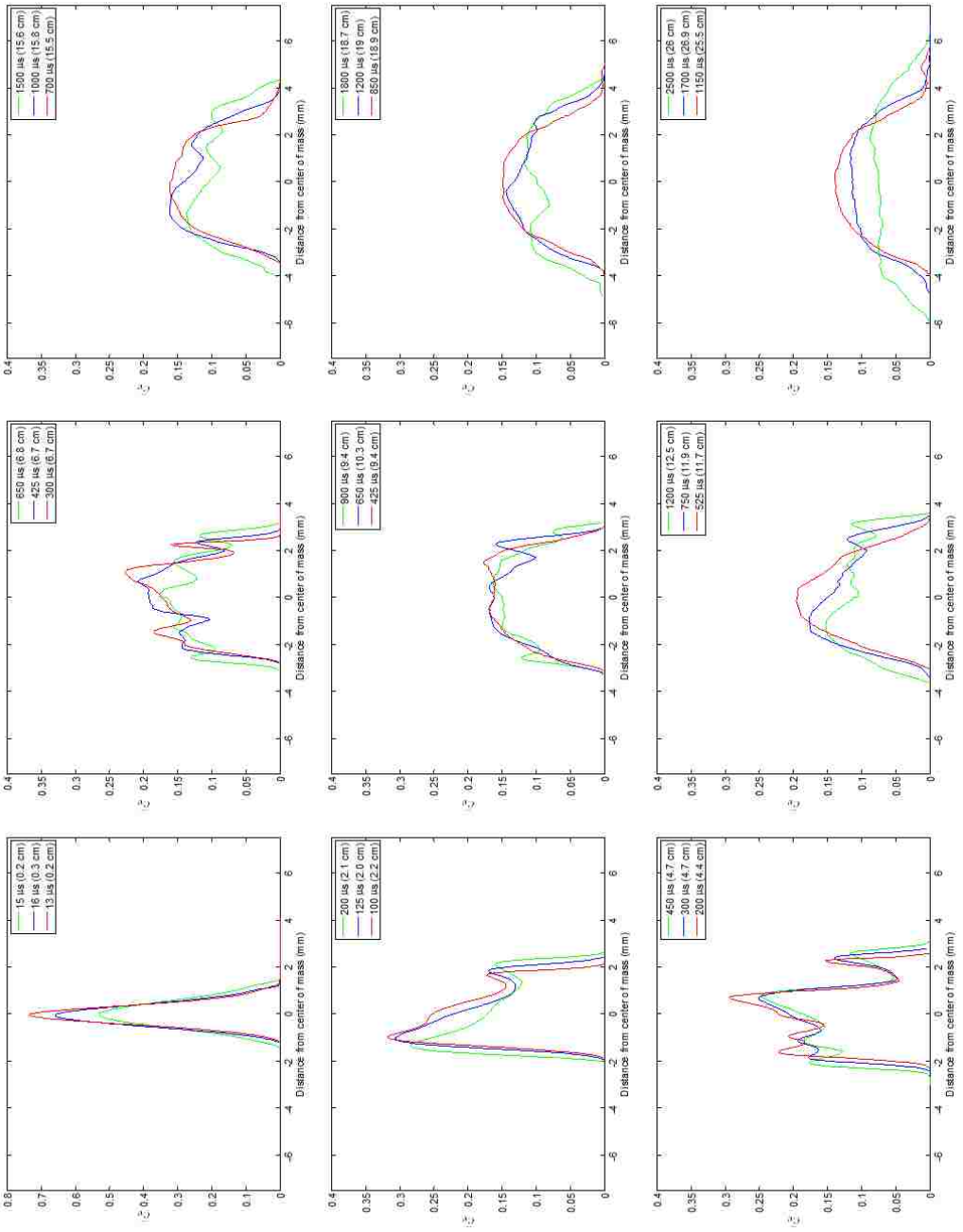


Figure 4.53: Time evolution of streamwise profile of volume fraction of $SF_6$, $\overline{c_v}(x)$. Each plot compares $\overline{c_v}(x)$ for each Mach number at roughly the same distance the structure has traveled.

increasingly narrow, indicating increasing mixing uniformity for all cases, with peak probabilities occurring at higher values for higher Mach numbers, again indicating that as $M$ increases, less air is mixed with the heavy gas. An inspection of the 2-D volume fraction maps was required to interpret the local trough feature observed at low values of $c_v$ in the higher Mach number experiments. The values at the low local peak ($c_v \approx 0.06$) correspond only to values along the interfacial length for the higher Mach number cases. Because the interfacial area is fairly large, there is a local peak in the PDF at this low volume fraction region. Then, because the uniformity of mixing throughout the mixing layer is relatively higher, there is a second much larger peak near the mean value for the interior region of the mixing layer where the vortex cores do not have a fresh supply of pure air to mix with. In Mach 1.21 experiments, which have undergone more mixing with air, and is less uniformly mixed, there are values throughout the mixing layer corresponding to $c_v \approx 0.06$, and hence no trough is observed.

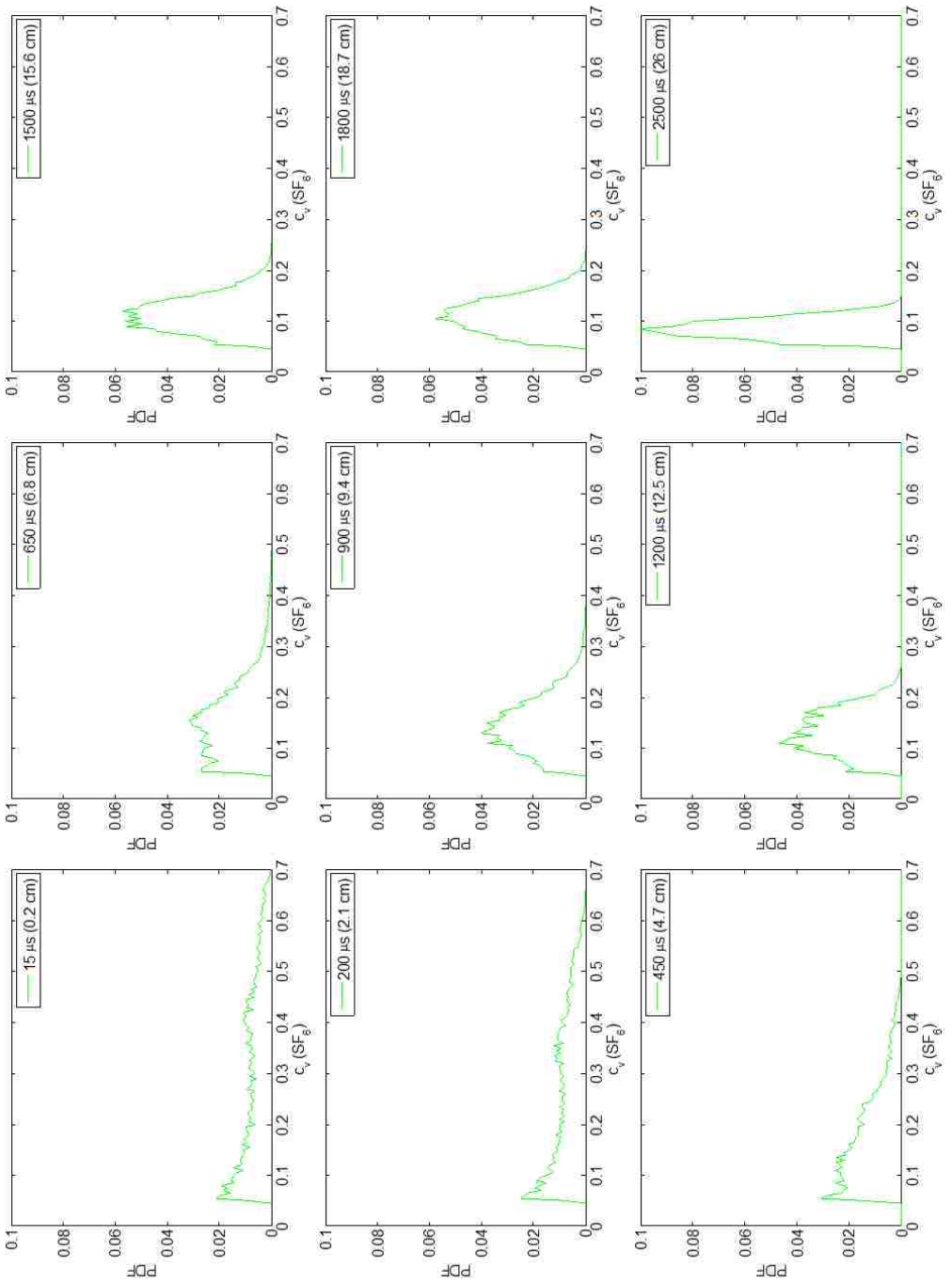


Figure 4.54: Time evolution of PDFs for volume fraction of $SF_6$ in Mach 1.21 experiments.

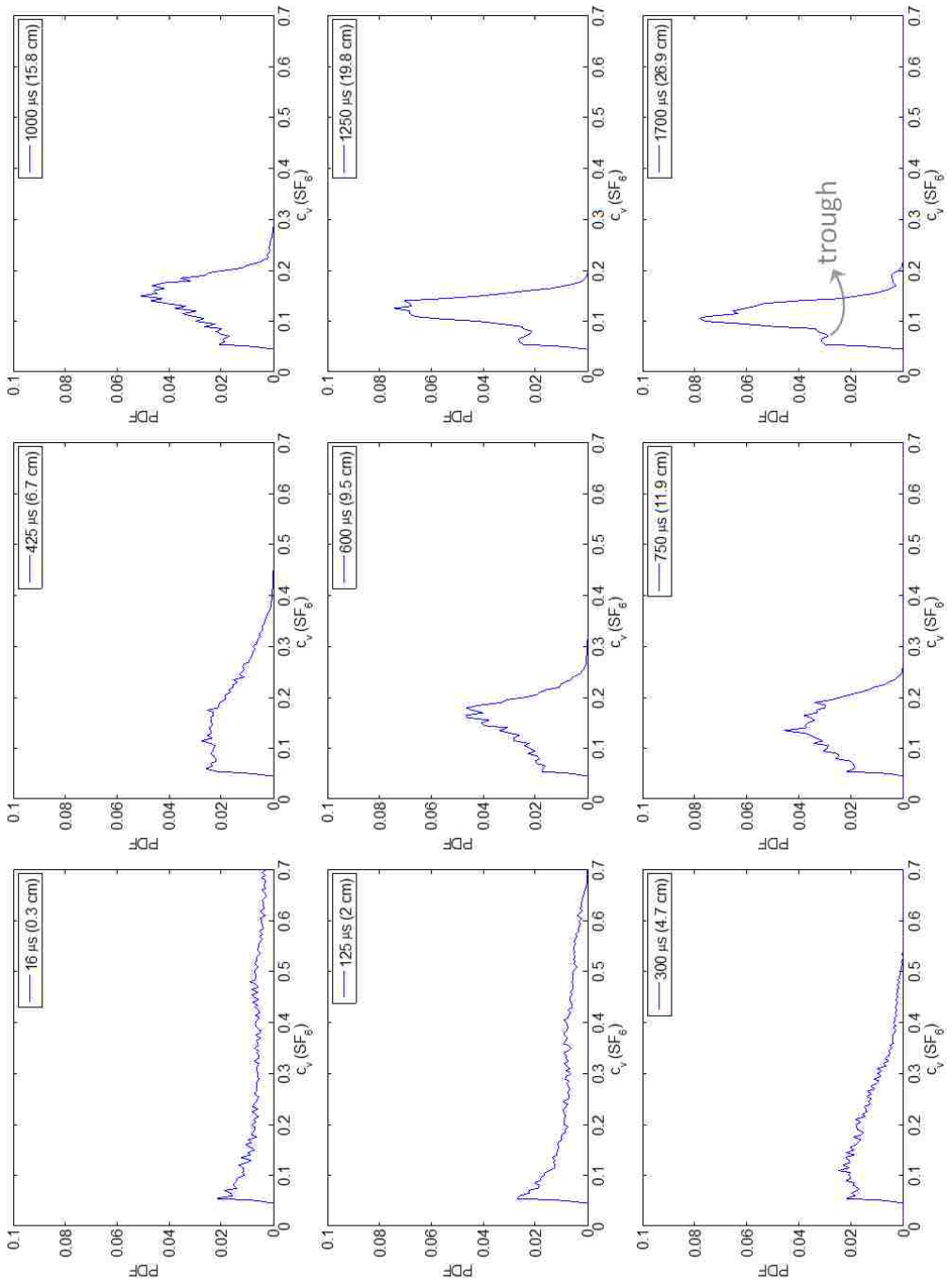


Figure 4.55: Time evolution of PDFs for volume fraction of $SF_6$ in Mach 1.36 experiments.

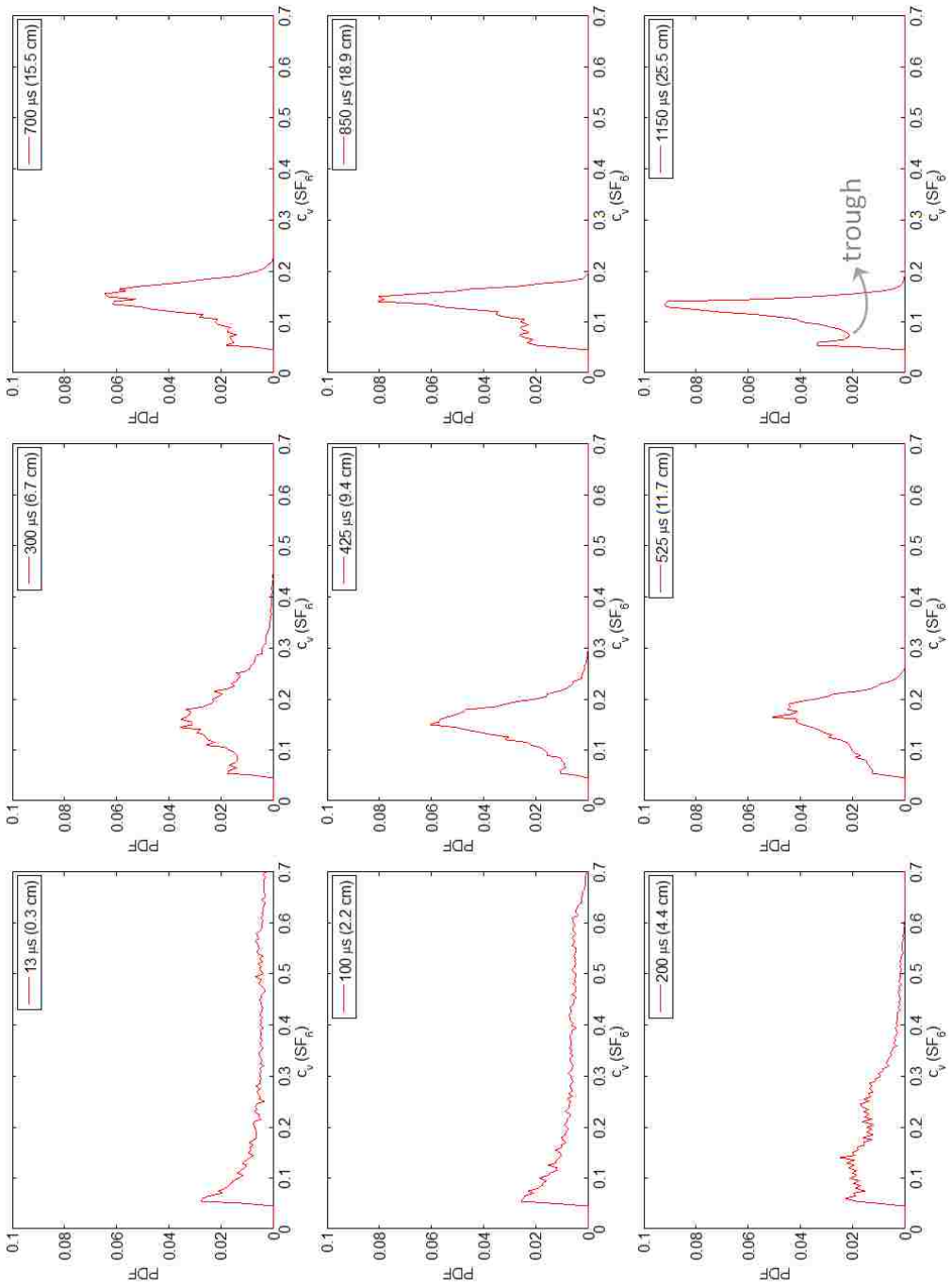


Figure 4.56: Time evolution of PDFs for volume fraction of $SF_6$ in Mach 1.50 experiments.

## 4.13 Vertical PIV Measurements

The vertical PIV measurements were intended to address open questions about the 3-dimensionality of the flow field in the current experiment, i.e. to what degree, and at what time do vertical motions in the flow field contribute to observations made at a given $x$-$y$ plane. In addition to the downward velocity already present in the ICs prior to shock interaction (-1.38 m/s at the center), vertical motions in the flow field can be due to a number of mechanisms. First, as the initial curtain flows through the test section, diffusion acts to decrease the density gradient, presumably resulting in less baroclinic vorticity production at lower locations upon shock wave interaction. Greater vorticity near the top results in lower pressure, and could theoretically cause upward motion through the center of the vortex cores, similar to a tornado. This is believed to explain observations from previous gas curtain experiments using stereo-PIV, in which higher positive vertical velocities were found at vortex core centers. A second mechanism is the deposition of vorticity in the $x$-$z$ plane itself due to the geometric variation of the ICs in the vertical direction, both because of diffusion, as well as any unsteady motions in the curtain as it flows downward. Another mechanism, is the generation of vertical velocity fluctuations as the mixing layer transitions to turbulence as time progresses. Finally, the shock wave itself, if not perfectly flat, could also result in fluid accelerations with vertical components and vorticity deposisition in the $x$-$z$ plane.

The current experiments represent the first PIV measurements of the post-shock flow field in the $x$-$z$ plane in the facility. Only early time vertical PIV experiments were performed, with 250, 150, and 125 μs being the latest times investigated for $M$ = 1.21, 1.36, and 1.50, respectively. Figure 4.57, shows the time evolution of raw particle field images for each Mach number, with the bulk flow moving from left to right. The vertical extents of the visualization in the $z$ direction extend from -5 mm to -46 mm, where 0 indicates the top wall of the test section. The total height of

the test section is 76.2 mm. Variations in the $z$ direction are observed, with the top portions of the curtain lagging behind. At the latest time investigated for each case, a second band of material appears downstream as mixing layer begins to roll up. Although the laser sheet was positioned along the center line of the center heavy gas jet, the finite thickness of the laser sheet causes this feature to be observed as the onset of roll up of the primary mushrooms carries heavy gas into the illuminated region. Because the vorticity is higher closer to the nozzle exit, more roll up occurs, thus making this feature more dramatic near the top.

Figures 4.58 and 4.59 show, respectively, the spatial distribution of vertical velocity, $w$, and the spatial distribution of streamwise fluctuations from the mean, $u' = u - \overline{u}$ after processing the data from Figure 4.57. Here, $\overline{u}$ represents the mean streamwise velocity in each realization. Note that all previously discussed horizontal measurements in the $x$-$y$ plane took place at $z$ = -20 mm. In Figure 4.58, peak vertical velocity magnitudes are observed to be on the order of 10% of $\overline{u}$, with the highest upward velocities located near the top of the test section. As time progresses, the region of the flow that experiences relatively high upward velocities continues to extend in the negative $z$ direction with the last time in the Mach 1.21 experiments being the only exception. Because all of these experiments were performed before vortex core formation, the first mechanism for vertical velocity production can be excluded from consideration. Consequently, turbulent velocity fluctuations can also be dismissed.

That leaves spatial variations in the initial conditions or the shock wave itself as possible explanations for the observed vertical velocities. Due to the presence of high positive vertical velocities and low horizontal velocities near the top of the test section, it is hypothesized that the openings in the test section, which allow for the passive co-flow of air on either side of the heavy gas curtain, permit expansion of the primary shock wave at the top, and is the primary mechanism at play. In this

way, the geometry of the test section appears to have an effect on the primary shock wave, resulting in a reduced pressure gradient, less horizontal acceleration and some positive vertical acceleration as expansion occurs near the top of the shock tube. Although the bottom of the curtain was not visualized in these experiments, the opening for the suction is presumed to produce a similar effect.

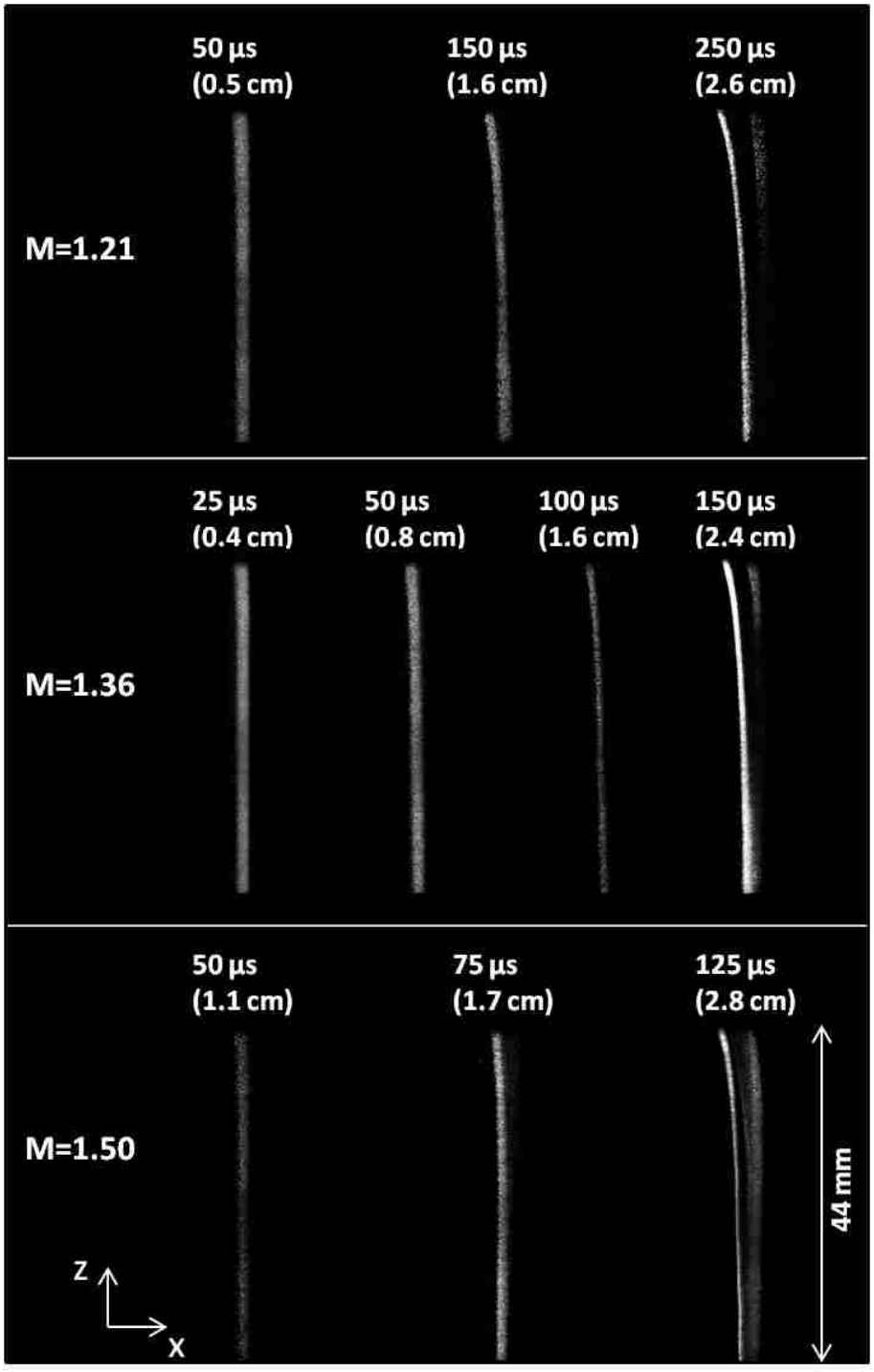


Figure 4.57: Early time evolution of raw particle fields obtained during vertical PIV measurements show variation of flow field with vertical position.

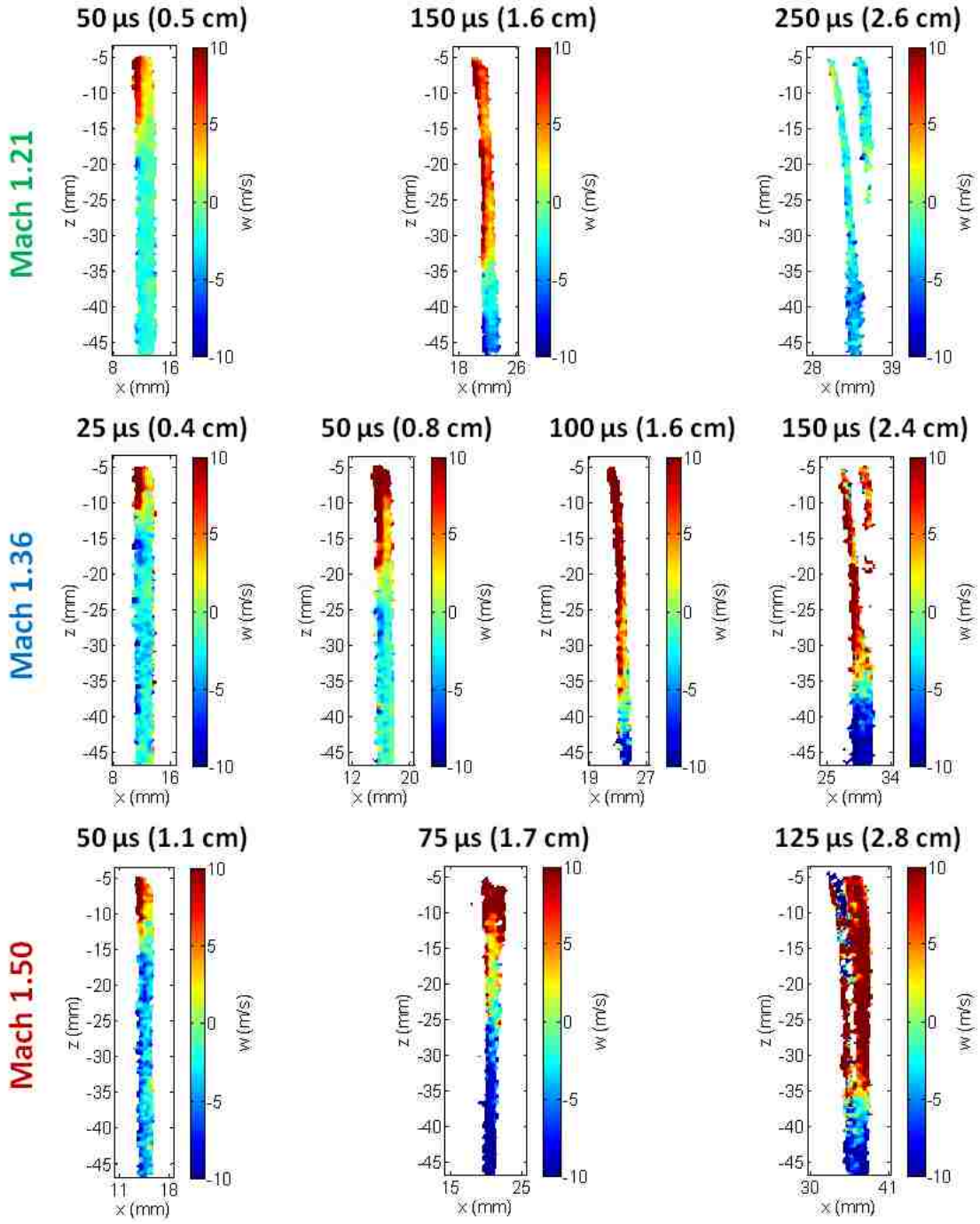


Figure 4.58: Spatial maps showing vertical velocity, $w$, as a function of time for each Mach number. Upwards velocities on the order of 10% of $\overline{u}$ are observed near the top of the curtain.

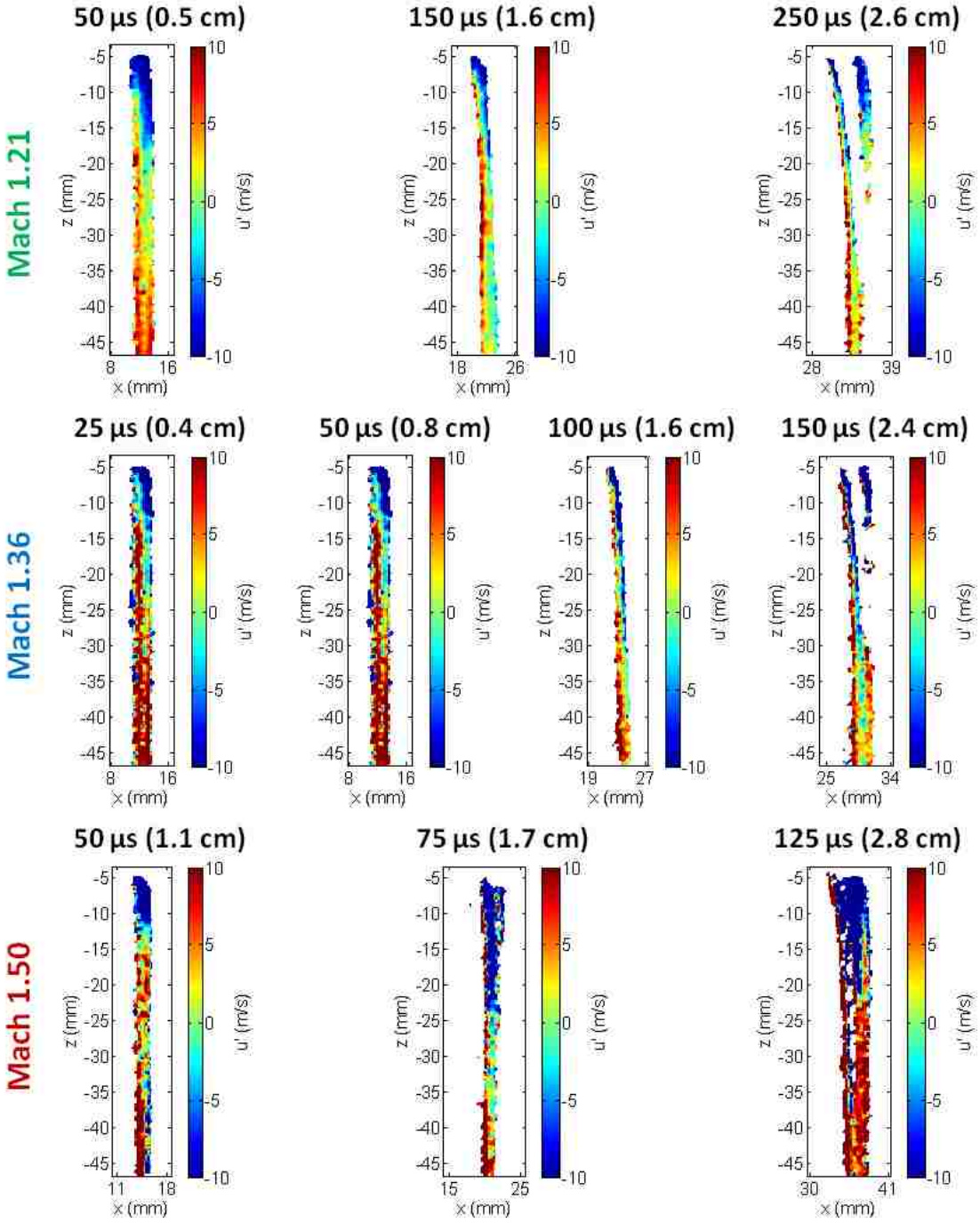


Figure 4.59: Spatial maps showing streamwise velocity fluctuations from the mean, $u'$, as a function of time for each Mach number.

# Chapter 5

# Conclusions

Experiments were performed at the horizontal gas shock tube facility at Los Alamos National Laboratory to characterize the Richtmyer-Meshkov instability and subsequent mixing of a varicose perturbed heavy gas curtain after it is impulsively accelerated by shock waves of varying Mach numbers. Advanced imaging diagnostics, namely, simultaneous quantitative PLIF/PIV, were implemented to provide the most comprehensive and extensive experimental quantification of RM induced mixing to date. Experimental repeatability was demonstrated, making it feasible to track many flow features through time despite only capturing two density fields and one velocity field for each run of the experiment.

Most measurements were obtained in the horizontal $x$-$y$ plane located 2 cm below the top wall of the shock tube, however, a small number of experiments were performed in the vertical $x$-$z$ plane located at the spanwise center of the shock tube to assess the significance of three-dimensional effects on the flow field. Three different incident shock Mach numbers were explored: $M = 1.21$, 1.36, and 1.50. For each case, a time evolution of density and velocity fields were constructed, allowing for both a qualitative and quantitative comparison of post-shock flow evolution. Three

time regimes were identified: early, characterized by qualitatively similar instability development between each Mach number in scaled time; intermediate, characterized by the emergence of differences in instability development; and late, characterized by features that cause a secondary jump in instability growth rate.

Although the large scale flow morphology observed in the density maps is similar at early times, several flow features are identified that are considered to be the result of Mach number effect. At early times these features are: (1) development of the RM instability occurs faster in time in higher Mach number experiments, (2) the higher the Mach number the smaller the overall width at a given stage of vortex development, (3) the shape of the bridge material becomes increasingly flatter with higher Mach number, and (4) the spike feature is increasingly prominent with increasing Mach number.

As time progresses, greater differences in flow features emerge that are additionally attributed to Mach number effect. These are: (5) the streamwise location of the vortex cores relative to the spanwise averaged center of mass is farther upstream with decreasing Mach number, (6) vortex cores develop small scale mixing faster in both real and scaled time with increasing Mach number, (7) mushroom stems become increasingly elongated with decreasing Mach number, (8) vortex induced material ejections on the downstream edge of the mixing layer become increasingly prominent with increasing Mach number, (9) experimental repeatability and flow field symmetry is greater with increasing Mach number, and (10) uniformity of mixing across the mixing layer is greater with increasing Mach number.

A plot of mixing width *vs.* time is presented, along with best fit curves generated using the Jacobs *et al.* [40] mixing width model and varying the circulation parameter. The best fit curves showed good agreement to the experimental data until late times when secondary growth features emerge in the experiments, suggesting that the physics in the model is appropriate at early and intermediate times when the flow is

dominated by a row of vortices.

In an attempt to collapse mixing width data for the three Mach number cases, several ways of scaling the time axis and width axis are presented, and demonstrate the fidelity of scaling methods employed in the existing literature. It was found that simply scaling the time axis with the convection velocity of the mixing layer is sufficient for collapsing the width data, in that the growth rate with distance traveled is the same until the very latest times measured. The remaining difference in width at the same scaled time appears to be the result of the curtain undergoing a greater amount of compression with increasing Mach number, and can be eliminated by scaling the width axis as well.

The state of the mixing layer at a particular downstream location can be of interest to researchers studying inertial confinement fusion or supersonic combustion ramjet engines, for example, in which the amount of space for the instability to develop before ignition occurs is fixed. Whether mixing is desired or not, such information could prove useful for optimization of operating Mach number. Therefore, distance traveled is used as the preferred scaled time in this study, and all other parameters investigated include comparisons between Mach number experiments at the same downstream location.

From the PIV measurements, several quantities were derived, including vorticity, circulation, velocity fluctuations, and TKE estimates based on available data. Each helps to explain or confirm observations made from the density maps. In general, each velocity derived quantity is consistent with the notion that the mixing layer is initially strained, causing an intensification of density gradients along the interface, followed by a cascade of the flow to smaller scales as the velocity field becomes more disordered, enhancing the small scale mixing between the two gases. Without additional energy input after the incident shock wave, each quantity decreases over time. The decreasing of velocity based quantities is indicative of either a transition

of the flow to sub-resolution scales, or that viscous and three-dimensional factors are important. It is likely that each contributes to some degree. It was also found that the rate of decrease of these quantities with distance traveled is similar for each Mach number, suggesting that, in scaled time, Mach number does not have a large effect on the spatially averaged or integrated velocity field, except in magnitude.

In addition to mixing layer width, several quantities that are derived from the PLIF measurements are presented, including instantaneous mixing rate, density self-correlation, the power spectra of the density field, mixing layer area, mixing layer mean $SF_6$ volume fraction, and interface length. These quantities provide information about how quickly mixing occurs, and how well mixed the two fluids become, both in terms of the uniformity of mixing throughout the layer, and the degree to which air and heavy gas intermix. Even when compared at the same downstream location, it is apparent from a qualitative inspection of density maps, that higher Mach number leads to a more well mixed state. But this assessment depends on how 'well mixed' is defined. If well mixed refers to the homogeneity of the density across the mixing layer, then it is true that higher Mach number yields more mix. However, quantities such as mixing layer width, instantaneous mixing rate, mixing layer area, and mean volume fraction indicate the somewhat counterintuitive result that lower Mach number yields greater mix at a given downstream location if 'mix' is meant to refer to the interpenetration of one fluid into another (determined by mixing layer width), or to the amount of originally unmixed fluid that undergoes some molecular mixing (determined by mixing layer area and mean volume fraction). Depending upon the specific application, the use of one definition over the other may be preferred for optimization.

A small number of PIV experiments were performed in the $x$-$z$ plane to measure vertical motions in the flow field. It was found that three-dimensional effects are present even at early times for all three Mach numbers, most likely resulting from

the interaction of the shock wave with openings in the test section that allow the passive co-flow of air on either side of the heavy gas curtain. More experiments extending later in time would be required to assess the degree to which these motions influence the measurements taken at the 2 cm horizontal plane. However, it is believed that these three-dimensional effects are small compared to mixing mechanisms that operate in the horizontal measurement plane, at least throughout early and intermediate times.

While these results provide insight into mixing mechanisms and processes in shock-induced variable density flows, the impact of this work resides particularly in its usefulness as a validation and calibration tool for turbulent mixing models and numerical simulations. The application of state of the art imaging diagnostics allows for a quantitative comparison of numerous flow field parameters, which provide the opportunity for a rigorous approach to validation that extends far beyond previous studies that rely solely on mix width data and qualitative flow evolution for simulation performance.

# Appendices

# Appendix A

# Preshock

In the course of acquiring the experimental data, the ICs were occasionally observed to have been deformed before the arrival of the primary shock wave. ICs disturbed in this way have come to be designated as "preshocked." While the preshock effect has been known for some time, it had never been the focus of analysis in this experimental facility. In most experiments, to prevent premature rupture, multiple polypropolene diaphragms were stacked to isolate the driver section prior to shock formation. In general, the number of polypropylene diaphragms used is 1 or 2 for Mach 1.21, 3 for Mach 1.36, and 5 for Mach 1.50. It is proposed that during the finite time it takes for all diaphragms to rupture, a sound wave is generated in air that begins to propagate down the length of the shock tube before the shock wave is formed. One possible mechanism for this could be a drum-like effect, wherein a pressure wave from the driver section generated from the rupture of one diaphragm collides with a subsequent unruptured diaphragm. Since the diaphragms are taut under pressure, this pressure wave could have an effect like beating on a drum in the instant before the subsequent diaphragm is ruptured itself. In the higher Mach number experiments, it is believed that the higher pressure causes the diaphragms to rupture more rapidly, allowing the shock wave to catch, and consume, any sound waves (if present) prior to

arriving at the initial conditions. Consequently, preshocked ICs were only observed in Mach 1.21 experiments where more than one diaphragm was used.

It was found that ICs were deformed to varying degrees depending on the amount of time between the advanced pressure wave and the primary shock wave, with more time leading to more deformation. Figure A.1 shows initial conditions with different amounts of deformation, from no preshock in (a), to the most extreme preshocked case in (d). Each of the images on the left was chosen because the primary shock wave is also visualized traveling through the curtain, confirming that the deformation was produced in advance. An inspection of the pressure traces in Figures A.2, A.3, and A.4 reveals that there is a pressure rise ahead of the primary shock wave for all of the preshocked cases (in contrast to the normal case of no preshock presented in Figure 2.11). The advanced pressure rises are labeled "advanced wave." Furthermore, using pressure transducers 3 and 4, the advanced wave was measured to be traveling at 347 m/s for all preshock cases, just about the calculated value for the speed of sound.

Also in Figure A.1, (e) through (h) are images of the mixing layer 500 μs after the primary shock interaction that was captured in (a) through (d), respectively. It is clear that the deformation of the ICs can have a dramatic effect on the development of the instability. In the most extreme case, with the earliest advanced wave, image (h) shows a greatly enhanced degree of mixing, owing to the higher degree of complexity of the initial interface shown in (d). In Richtmyer-Meshkov experiments, where generation of gas-gas interfaces of varying configurations is an ongoing experimental challenge, the preshock phenomena, if controlled, could be used to an experimenter's advantage to generate shaped perturbations not easily achieved through nozzle design or other traditional methods, even including those that rely on membranes. If desired, these shaped perturbations could perhaps generate turbulent mixing earlier in time without requiring a reshock wave to deposit more energy, which is one tactic currently

used in this experimental facility.

In summary, caution should be taken in experimental facilities where multiple layers of diaphragms are used to separate the driver section, as sound waves can be generated in the finite time it takes to rupture the diaphragm. These sound waves can deform the initial conditions ahead of the primary shock wave leading to unexpected results. While the rupture process is unlikely to ever be controlled well enough to be highly repeatable, the preshock effect observed in these experiments demonstrates the possibility of using sound waves to create complex shaped perturbations for future studies.

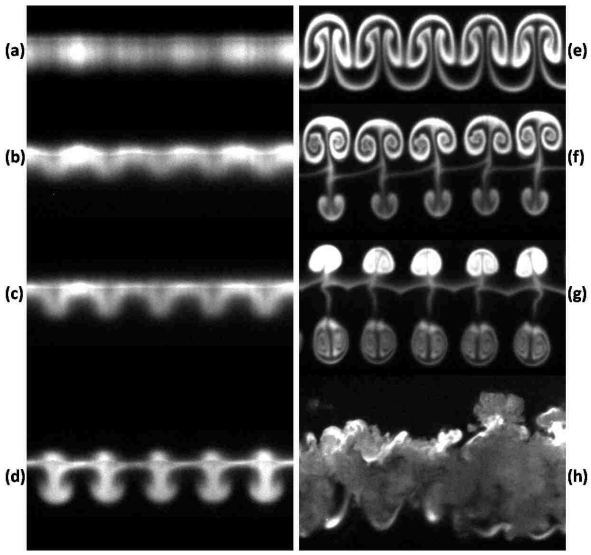


Figure A.1: PLIF images showing varying degrees of preshocked IC structures and the resulting post-shock structures within the same experiment. In each case on the left, the primary shock wave is captured traveling through the upstream edge of the ICs with the image in (a) showing no preshock for comparison. For preshocked images, the advanced pressure wave reached the ICs (b) 660 μs, (c) 1450 μs, and (d) more than 3000 μs before primary shock wave interaction, as shown in Figures A.2, A.3, and A.4, respectively. Images (e), (f), (g), and (h) on the right show the resulting flow field 500 μs later, after primary shock interaction.

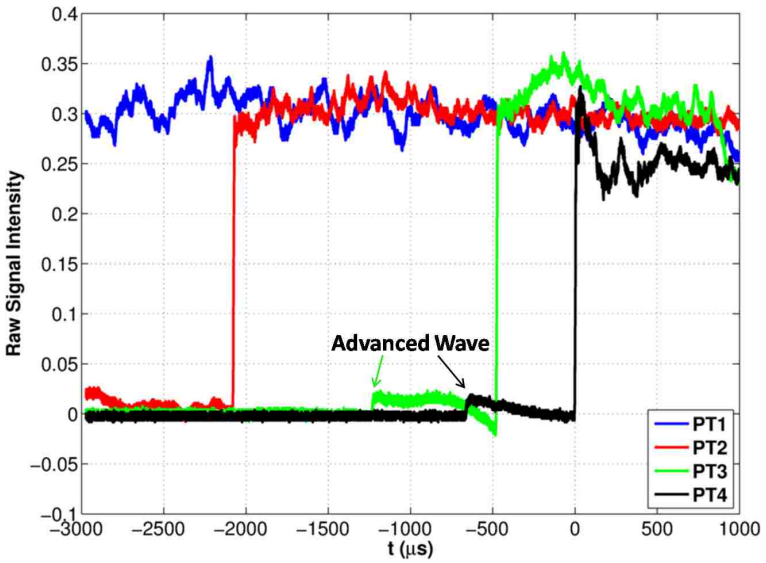


Figure A.2: Pressure traces from an experiment with late preshock occurring 660 μs ahead of the shock wave, as seen in the trace from PT4.

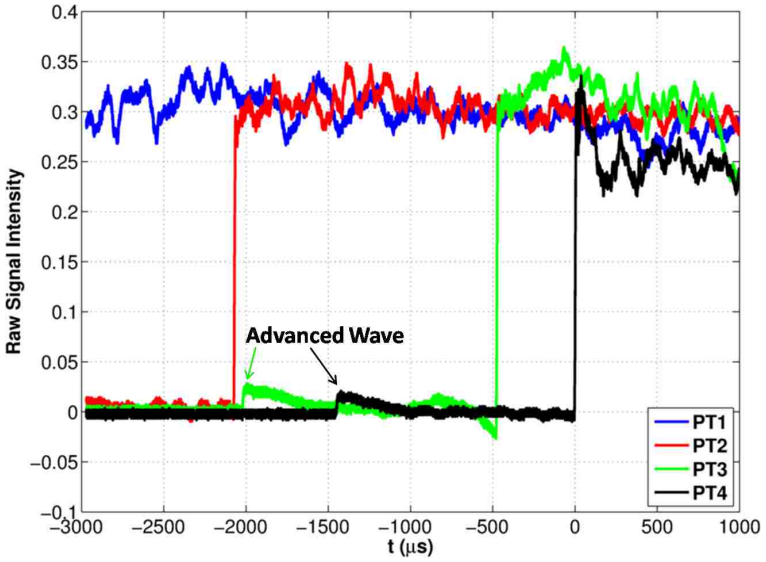


Figure A.3: Pressure traces from an experiment with intermediate preshock occurring 1450 μs ahead of the shock wave, as seen in the trace from PT4.

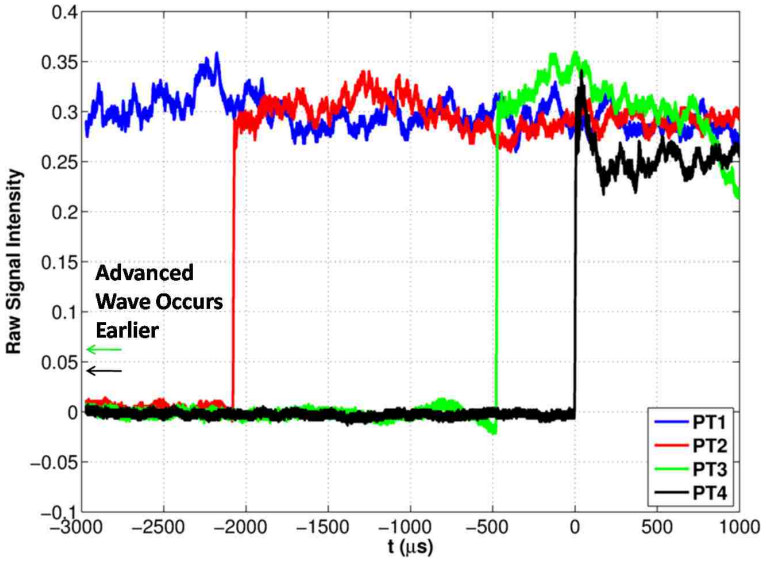


Figure A.4: Pressure traces from an experiment with early preshock occurring more than 3000 μs ahead of the shock wave, as seen in the trace from PT4.

# Appendix B

# Effect of PLIF Imaging on the Initial Conditions

Several experiments were performed to investigate the impact of the PLIF laser on the initial conditions, and thus the resulting flow. It was determined that if the PLIF laser power was high enough, and if the initial conditions were pulsed shortly before shock arrival, image blurring at subsequent dynamic times occurred (see Figure B.1 for a visual illustration). In general, the later the time, the higher the Mach number, and the higher the laser power, the more prominent the image blurring, as changes imposed by the laser upon the ICs get amplified over time. Interestingly, if the laser is pulsed just after shock passage or any time thereafter, no image blurring in dynamic images is observed, independent of laser power. Also, no image blurring is observed when the IC pulse power is sufficiently low. Although it appears that the IC laser pulse, when at high power and focused into a thin sheet, alters the initial conditions in some way, it remains inconclusive whether it is the $SF_6$ that is altered, or if it is only the acetone vapor seeding. One possible mechanism that can explain these observations could be the rapid (and perhaps uneven) heating leading to an alteration of density gradients, or indirectly, the subsequent generation of a sound

wave as the gas expands. It is also not known whether the effect has a threshold at some laser power intensity, below which no blurring occurs, or if it is continuous with laser power intensity, and that no blurring is observed when operating at low power because the effect is small. Consequently, to prevent contamination of this unknown effect on the data set, only those dynamic images acquired in absence of IC visualization were included in the analysis. Further study is needed to understand the mechanism that causes this image blurring effect, as its consequences could be important to many experiments that use PLIF diagnostics.

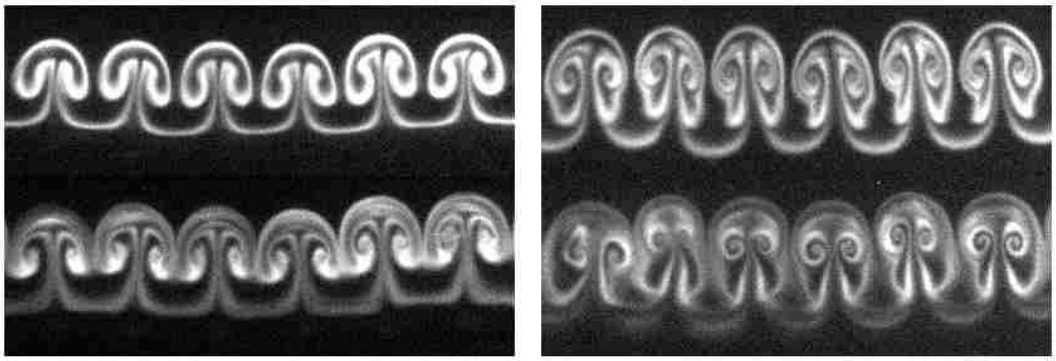


Figure B.1: (a) *Top*, An image from a Mach 1.54 experiment taken at $t$=215 μs; without pulsing the initial conditions, *bottom* an image from a different Mach 1.54 experiment at the same time with nominally the same initial conditions, but imaged with the IC laser pulse at maximum power; note the apparent blurring of material lines. (b) *Top*, An image from a Mach 1.21 experiment taken at $t$=615 μs; without pulsing the initial conditions, *bottom* an image from a different Mach 1.21 experiment at the same time with nominally the same initial conditions, but imaged with the IC laser pulse at maximum power; note the apparent blurring of material lines.

# Appendix C

# Evolution of the Spike Feature

Another Mach number effect observed in the current study is the amplitude of the spikes of material that are ejected downstream from the center of each mushroom structure at early times, circled in Figure 4.1. It is known that the shock wave front refracts as it passes through the perturbed heavy gas curtain. On the downstream edge of the $SF_6$, the curved shock front focuses as it exits the heavy gas and enters back into the lighter air, producing a larger localized pressure in that region of the heavy gas. The higher pressure causes a small amount of material to spike out ahead of the rest of the structure. This effect and its mechanism were first reported by Kumar *et al.* [37], in which the shock focusing within an 8 mm cylinder is clearly visualized in a Mach 1.2 experiment (see Figure C.1, reprinted from *Kumar et al.* [37]). In that study, the flow feature under discussion is referred to as a 'cusp' instead of 'spike' (see Figure C.1 (i)). In subsequent gas curtain experiments by Orlicz *et al.* [47] it was shown that more material is ejected downstream with increasing Mach number, presumably due to the greater pressures. The spike provides an example of a flow feature that appears to be generated on small scales, but grows to larger, resolved scales that are important for understanding material distribution throughout the mixing process. The development of such features can provide a

significant challenge for simulations.

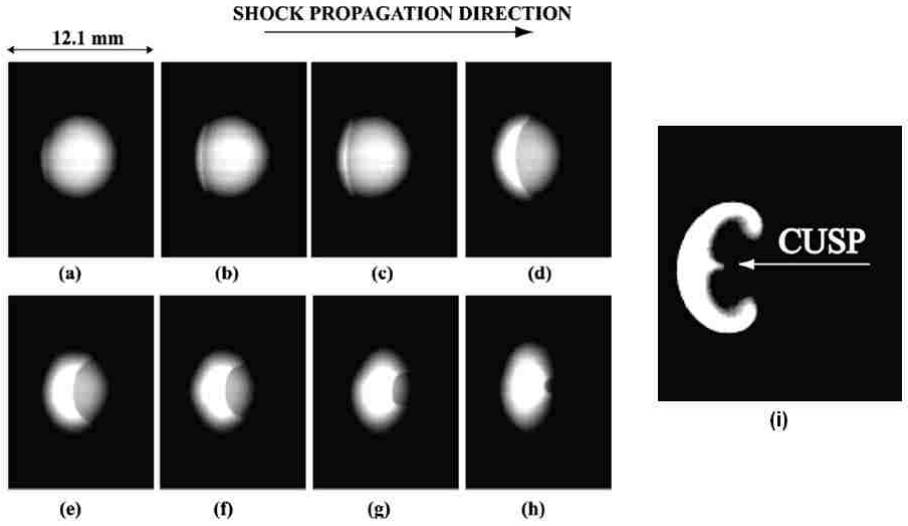


Figure C.1: From Kumar *et al.* [37], shows shock wave refraction as it passes through an 8 mm $SF_6$ cylinder. Flow is from left to right. (a) Shock wave just on upstream edge, $t$=0 μs; (h) Shock focuses on the downstream edge, $t$=30 μs; (i) high pressure region on downstream edge causes cusp feature to form, $t$=130 μs. ((i) is enlarged for visualization)

Figure C.2 shows contrast adjusted images that compare the evolution of the spike feature with time for experiments at each Mach number in the current study. Because the spike is formed from a small amount of material, the intensity of its PLIF signal is low, and it can be difficult to visualize without changing the contrast of the image as shown in Figure 4.1. In the higher Mach number experiments, the higher associated pressure causes more mass to constitute the spike. With time, the spike itself is then observed to roll up into an opposite facing mushroom. At 1150 μs in Mach 1.36 experiments and 575 μs in Mach 1.50 experiments, vortex induced ejections (labeled in Figure 4.1) begin to penetrate through the center of the opposite facing mushroom. As time progresses and the vortex induced ejections grow, it becomes no longer possible to distinguish the spike remnant from the material that makes up the vortex induced ejection. In Mach 1.21 experiments, only a hint of spike roll up is observed, as the relatively smaller amount of spike material mixes with the

surrounding air, thereby decreasing the PLIF signal until there is no evidence of the spike left after 950 μs. Over the range of Mach numbers studied, consistent with the results of Orlicz *et al.* [47], it appears that the higher the Mach number, the more material is ejected, and the more prominent the opposite facing mushroom appears to be at later times.

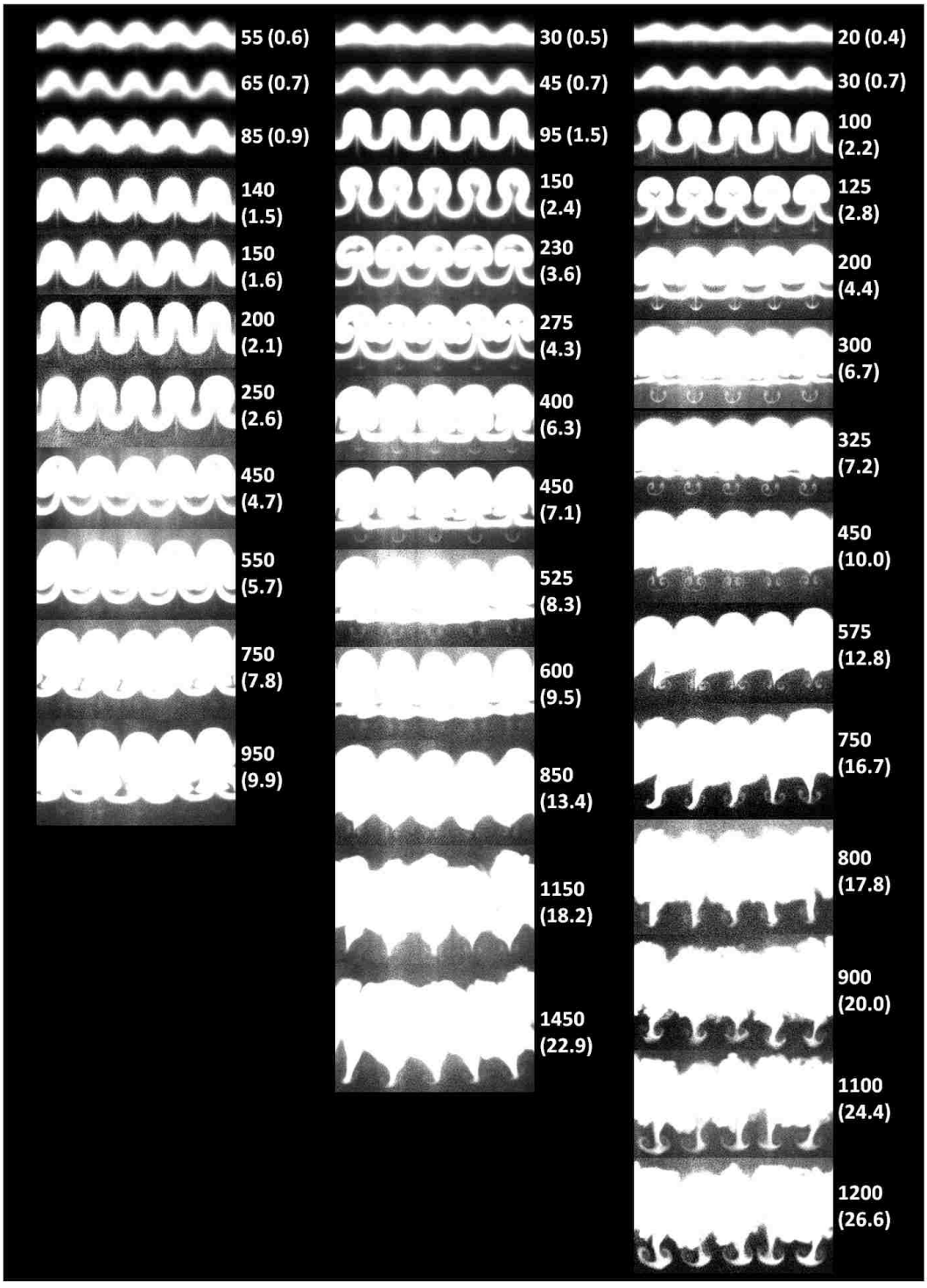


Figure C.2: Contrast adjusted density maps for spike evolution visualization. *Left column*: $M = 1.21$; *Middle column*: $M = 1.36$; *Right column*: $M = 1.50$.

# References


[1] R. D. Richtmyer. Taylor instability in shock acceleration of compressible fluids. *Communications on Pure and Applied Mathematics*, 13:297–319, 1960.

[2] Ye. Ye. Meshkov. Instability of a shock wave accelerated interface between two gases. Technical Report NASA TT F-13074, NASA Technical Translation, 1970.

[3] M. Brouillette. The Richtmyer-Meshkov instability. *Annual Review of Fluid Mechanics*, 34:445–468, 2002.

[4] Lord Rayleigh. *The Scientific Papers of Lord Rayleigh*, volume 2. Cambridge University Press, Cambridge, England, 1900.

[5] G. Taylor. The instability of liquid surfaces when accelerated in a direction perpendicular to their planes. *Proceedings of the Royal Society of London Series A*, 201:192–196, 1950.

[6] C. E. Niederhaus and J. W. Jacobs. Experimental study of the Richtmyer-Meshkov instability of incompressible fluids. *Journal of Fluid Mechanics*, 485:243–277, 2003.

[7] W.J. Hogan, R. Bangerter, and G.L. Kulcinski. Energy from inertial fusion. *Physics Today*, 45:42–50, 1992.

[8] J. Lindl. Development of the indirect-drive approach to inertial confinement fusion and the target physics basis for ignition and gain. *Physics of Plasmas*, 2(11):3933–4024, 1995.

[9] J. Yang, T. Kubota, and E. E. Zukoski. Applications of shock-induced mixing to supersonic combustion. *AIAA Journal*, 31(5):854–862, 1993.

[10] G. H. Markstein. Flow disturbances induced near a slightly wavy contact surface, or flame front, traversed by a shock wave. *Journal of the Aeronautical Sciences*, 24:238–239, 1957.

[11] W. D. Arnett, J. N. Bahcall, R. P. Kirshner, and S. E. Woosley. Supernova 1987a. *Annual Review of Astronomy and Astrophysics*, 27:629–700, 1987.

[12] B. D. Collins and J. W. Jacobs. PLIF flow visualization and measurements of the Richtmyer-Meshkov instability of an air/$SF_6$ interface. *Journal of Fluid Mechanics*, 464:113–136, 2002.

[13] M. Brouillette and B. Sturtevant. Growth induced by multiple shock waves normally incident on plane gaseous interfaces. *Physica D*, 37:248–263, 1989.

[14] I.G. Currie. *Fundamental Mechanics of Fluids*. New York: Marcel Dekker, Inc., 3rd edition, 2003.

[15] N. J. Zabusky. Vortex paradigm for accelerated inhomogeneous flows: visiometrics for the Rayleigh-Taylor and Richtmyer-Meshkov environments. *Annual Review of Fluid Mechanics*, 31:495–536, 1999.

[16] P. Vorobieff and S. Kumar. Experimental studies of Richtmyer-Meshkov instability. *Recent Research Developments in Fluid Dynamics*, 5:33–55, 2004.

[17] A. Rikanati, D. Oron, O. Sadot, and D. Shvarts. High initial amplitude and high Mach number effects on the evolution of the single-mode Richtmyer-Meshkov instability. *Physical Review E*, 67:026307, 2003.

[18] O. Sadot, A. Rikanati, G. Ben-Dor, and D. Shvarts. An experimental study of the high Mach number and high initial-amplitude effects on the evolution of the single-mode Richtmyer-Meshkov instability. *Laser and Particle Beams*, 21:341–346, 2003.

[19] O. Sadot, K. Levy, A. Yosef-Hai, D. Cartoon, Y. Elbaz, Y. Srebro, G. Ben-Dor, and D. Shvarts. Studying hydrodynamic instability using shock-tube experiments. *Astrophysics and Space Science*, 298:305–312, 2005.

[20] O. Sadot, L. Erez, U. Alon, D. Oron, L. Levin, G. Erez, G. Ben-Dor, and D. Shvarts. Study of nonlinear evolution of single-mode and two-bubble interaction under Richtmyer-Meshkov instability. *Physical Review Letters*, 80(8):1654–1657, 1998.

[21] M. V. Bliznetsov, N. V. Nevmerzhitsky, A. N. Rasin, E. A. Sotskov, E. D. Senkovsky, L. V. Tochilina, and V. A. Ustinenko. Study of turbulent mixing development at the gas-gas interface of shock wave at Mach numbers from 2-9. In *AIP Conference Proceedings*, volume 849, pages 341–346. American Institute of Physics, 2006.

[22] J. F. Haas and B. Sturtevant. Interaction of weak shock waves with cylindrical and spherical gas inhomogeneities. *Journal of Fluid Mechanics*, 181:41–76, 1987.

[23] D. A. Holder, A. V. Smith, C. J. Barton, and D. L. Youngs. Shock-tube experiments on Richtmyer-Meshkov instability growth using an enlarged double-bump perturbation. *Laser and Particle Beams*, 21(3):411–418, 2003.

[24] R. Bonazza and B. Sturtevant. X-ray measurements of growth rates at a gas interface accelerated by shock waves. *Physics of Fluids*, 8(9):2496–2512, 1996.

[25] P. B. Puranik, J. G. Oakley, M. H. Anderson, and R. Bonazza. Experimental study of the Richtmyer-Meshkov instability induced by a Mach 3 shock wave. *Shock Waves*, 13:413–429, 2004.

[26] M. A. Jones and J. W. Jacobs. A membraneless experiment for the study of Richtmyer-Meshkov instability of a shock-accelerated gas interface. *Physics of Fluids*, 9(10):3078–3085, 1997.

[27] J. W. Jacobs and V. V. Krivets. Experiments on the late-time development of single-mode Richtmyer-Meshkov instability. *Physics of Fluids*, 17(3):034105, 2005.

[28] J. W. Jacobs and J. M. Sheeley. Experimental study of incompressible Richtmyer-Meshkov instability. *Physics of Fluids*, 8(2):405–415, 1996.

[29] R. F. Benjamin and J. N. Fritz. Shock loading a rippled interface between liquids of different densities. *Physics of Fluids*, 30(2):331–336, 1987.

[30] R. L. Holmes, G. Dimonte, B. Fryxell, M. L. Gittings, J. W. Grove, M. Schneider, D. H. Sharp, A. L. Velikovich, R. P. Weaver, and Q. Zhang. Richtmyer-Meshkov instability growth: experiment, simulation and theory. *Journal of Fluid Mechanics*, 389:55–79, 1999.

[31] G. Dimonte and B. Remington. Richtmyer-Meshkov experiments on the Nova laser at high compression. *Physical Review Letters*, 70(12):1806–1809, 1993.

[32] D. Ranjan, M. Anderson, J. Oakley, and R. Bonazza. Experimental investigation of a strongly shocked gas bubble. *Physical Review Letters*, 94:184507, 2005.

[33] D. Ranjan, J. Niederhaus, B. Motl, M. Anderson, J. Oakley, and R. Bonazza. Experimental investigation of primary and secondary features in high-Mach-number shock-bubble interaction. *Physical Review Letters*, 98:024502, 2007.

[34] J.W. Jacobs. The dynamics of shock accelerated light and heavy gas cylinders. *Physics of Fluids A*, 5(9):2239–2247, 1993.

[35] C. D. Tomkins, K. P. Prestridge, P. M. Rightley, P. V. Vorobieff, and R. F. Benjamin. Flow morphologies of two shock-accelerated, unstable gas cylinders. *Journal of Visualization*, 5:273–283, 2002.

[36] C. Tomkins, K. Prestridge, P. Rightley, M. Marr-Lyon, P. Vorobieff, and R. Benjamin. A quantitative study of the interaction of two Richtmyer-Meshkov-unstable gas cylinders. *Physics of Fluids*, 15(4):986–1004, 2003.

[37] S. Kumar, G. Orlicz, C. Tomkins, C. Goodenough, K. Prestridge, P. Vorobieff, and R. Benjamin. Stretching of material lines in shock-accelerated gaseous flows. *Physics of Fluids*, 17:082107, 2005.

[38] J. W. Jacobs, D. L. Klein, D. G. Jenkins, , and R. F. Benjamin. Instability growth patterns of a shock-accelerated thin fluid layer. *Physical Review Letters*, 70(5):583–586, 1993.

[39] J. M. Budzinski, R. F. Benjamin, and J. W. Jacobs. Influence of initial conditions on the flow patterns of a shock-accelerated thin fluid layer. *Physics of Fluids*, 6(11):3510–3512, 1994.

[40] J.W. Jacobs, D.G. Jenkins, D.L. Klein, and R.F. Benjamin. Nonlinear growth of the shock-accelerated instability of a thin fluid layer. *Journal of Fluid Mechanics*, 295:23–42, 1995.

[41] P. M. Rightley, P. Vorobieff, and R. F. Benjamin. Evolution of a shock-accelerated thin fluid layer. *Physics of Fluids*, 9(6):1770–1782, 1997.

[42] P. M. Rightley, P. Vorobieff, R. Martin, and R. F. Benjamin. Experimental observations of the mixing transition in a shock-accelerated gas curtain. *Physics of Fluids*, 11(1):186–200, 1999.

[43] K. Prestridge, P. M. Rightley, P. Vorobieff, R. F. Benjamin, and N. A. Kurnit. Simultaneous density-field visualization and PIV of a shock-accelerated gas curtain. *Experiments in Fluids*, 29:339–346, 2000.

[44] K. Prestridge, P. Vorobieff, P. M. Rightley, and R. F. Benjamin. Validation of an instability growth model using particle image velocimetry measurements. *Physical Review Letters*, 84(19):4353–4356, 2000.

[45] P. Vorobieff, P. M. Rightley, and R. F. Benjamin. Shock-driven gas curtain: fractal dimension evolution in transition to turbulence. *Physica D*, 133:469–476, 1999.

[46] B. J. Balakumar, G. C. Orlicz, C. D. Tomkins, and K. P. Prestridge. Simultaneous particle-image velocimetry-planar laser-induced fluorescence measurements of Richtmyer-Meshkov instability growth in a gas curtain with and without reshock. *Physics of Fluids*, 20:124103, 2008.

[47] G. C. Orlicz, B. J. Balakumar, C. D. Tomkins, and K. P. Prestridge. A Mach number study of the Richtmyer-Meshkov instability in a varicose, heavy-gas curtain. *Physics of Fluids*, 21:064102, 2009.

[48] K. O. Mikaelian. Numerical simulations of Richtmyer-Meshkov instabilities in finite-thickness fluids layers. *Physics of Fluids*, 8(5):1269–1292, 1996.

[49] B. Motl, J. Oakley, D. Ranjan, C. Weber, M. Anderson, and R. Bonazza. Experimental validation of a Richtmyer-Meshkov scaling law over large density ratio and shock strength ranges. *Physics of Fluids*, 21:126102, 2009.

[50] G. Orlicz. Shock driven instabilities in a varicose, heavy–gas curtain: Mach number effects. Master's thesis, University of New Mexico, 2007.

[51] L. M. Pickett and J. B. Ghandhi. Passive scalar measurements in a planar mixing layer by PLIF of acetone. *Experiments in Fluids*, 31:309–318, 2001.

[52] R. Bonazza. *University of Wisconsin Shock Tube Laboratory (accessed online)*, 2004. http://silver.neep.wisc.edu/∼shock/.

[53] M. Thurber. *Acetone laser-induced fluorescence for temperature and multiparameter imaging in gaseous flows*. PhD thesis, Stanford University, 1999.

[54] B. Balakumar, G. Orlicz, J. Ristorcelli, S. Balasubramanian, K. Prestridge, and C. Tomkins. Turbulence in a Richtmyer-Meshkov fluid layer after reshock: velocity and density statistics. *Journal of Fluid Mechanics*, (doi: 10.1017/jfm.2012.8), 2012.

[55] M. Anderson. *Oblique shock interactions with perturbed density interfaces*. PhD thesis, University of New Mexico, 2011.

[56] J. Jimenez. Intermittency and cascades. *Journal of Fluid Mechanics*, 409:99–120, 2000.

[57] P. Dimotakis. The mixing transition in turbulent flows. *Journal of Fluid Mechanics*, 409:69–98, 2000.

[58] P. E. Dimotakis. Turbulent mixing. *Annual Review of Fluid Mechanics*, 37:329–356, 2005.

[59] C. Tomkins, S. Kumar, G. Orlicz, and K. Prestridge. An experimental investigation of mixing mechanisms in shock-accelerated flow. *Journal of Fluid Mechanics*, 611:31–150, 2008.

[60] D. Besnard, F. H. Harlow, R. M. Rauenzahn, and C. Zemach. Turbulence transport equations for variable-density turbulence and their relationship to two-field models. Technical Report LA-12303-MS, Los Alamos National Laboratory, 1992.